LUNFD6/(NFFL-7234)2011

High Momentum Resolution Tracking in a Linear Collider Experiment; Test Results from a Prototype TPC.

Master's Thesis
by

Martin Ljunggren

Supervisors:
Leif Jönsson
Anders Oskarsson

LUND
UNIVERSITY

DEPARTMENT OF PHYSICS
LUND, 2011

Contents

Abstract

The Large Hadron Collider (LHC) is in the starting phase of its operation. It is believed that many exciting measurements will be made here. Among other things, it is the hope of the particle physics community that the elusive Higgs Boson will finally be detected here. At the same time, research and development is being conducted towards the next large experiment, which will probably be a linear lepton collider. Such a facility is more suited to conduct precision measurements which are more difficult at a hadron collider.

The work in this thesis has been made within the LCTPC-collaboration, an international collaboration for studying the technical aspects af a possible tracking detector at a linear collider. The collaboration has built a prototype Time Projection Chamber (TPC) for testing the properties of different readout structures. A TPC is a tracking detector consisting of a gas filled drift volume placed in a solenoidal magnetic field where the readout is made using a segmented plane of so called *pads*. When a charged particle traverses the chamber, it ionizes the gas and leaves a trail of electrons which are subjected to an electric field that makes them drift towards the readout plane where they are collected on the pads. The TPC is capable of 3D tracking, i.e. determining track coordinates in both the drift direction (z) and in the plane perpendicular to this direction (the "bend plane"), as well as momentum and energy loss measurements.

This thesis focuses on measurements made using a certain kind of readout structure, Gas Electron Multipliers (GEMs), which promise better performance than previously used techniques. Spatial and momentum resolution are important for a linear collider, and GEMs offer considerable improvement in this area.

The measurements were made at the DESY test beam 24 in Hamburg with a 5GeV electron beam. The readout structure made it possible to measure tracks of approximately 50cm in length. Unfortunately, the measurements suffered from distortions created by an inhomogeneous electric field caused by the GEM support structure. A correction for this was attempted using the Millepede method, which allowed an alignment of the recorded particle tracks. Using the corrections, a spatial resolution of $\sigma_y(0) = 59 \pm 0.4 \mu m$ and $\sigma_z(0) = 204 \pm 0.9 \mu m$ was obtained for the drift direction and the bend plane respectively. An estimation of the momentum resolution was also obtained, 0.00919 ± 0.00018 GeV^{-1}, which compares well to the goals set for the final TPC envisaged for the linear collider.

Till Elin. Tack för ditt tålamod och för att du finns. Jag älskar dig.

Chapter 1

Introduction

The idea that matter is made up of discrete building blocks is not a new one. It existed long before modern physics and chemistry. The ancient greeks were on to it, and they were not even first (the ancient indians probably were [1]). It is however from the Greek word atomos, which means indivisible, that we get the word atom.

When what we now call atoms were first discovered they were thought to be indivisible, hence the name. This turned out to be a mistake when the electron was discovered by Thomson in 1897. Furthermore, in 1909, Rutherford discovered the nucleus by observing the deflection of alpha particles incident on a gold foil. Later it was discovered that nuclei consist of electrically charged protons and, in most cases, electrically neutral particles called neutrons.

Since then, a large number of subatomic particles have been discovered. The neutrino for example, originally proposed to solve the mystery of the continuous energy distribution of beta decay, was detected in 1956. By 1964 a large number of particles had been detected, most of them in accelerator experiments. Attempts to classify them led to the suggestion by Murray Gell-Mann and George Zweig that many of the discovered particles were made of smaller particles called *quarks*. At first, many physicists considered the quarks to be nothing but mathematical entities useful for theoretical calculations but nothing more. Their existence has since been verified in numerous experiments.

In the current understanding, matter is made of 12 fundamental particles and their antiparticles. They are in turn subdivided into 6 *quarks* and 6 *leptons*. The interactions between the particles are mediated by four fundamental forces. These are gravity, the electromagnetic force, and the weak and the strong forces. It is believed that they share a common origin and will merge into one single interaction at a high enough energy. Quarks form composite particles known as *hadrons*. There is no evidence that these particles should have substructure themselves. This question is not settled however and there are a number of theories suggesting that the particles found so far are not fundamental. Another theory, called string theory, suggests that the particles are made up of vibrating strings. It is also widely believed that there should be more particles left to discover, even if the 12 particles prove to be fundamental. This idea is supported by the fact that a common theory of the electromagnetic and weak forces (the *electroweak* theory) has already been formulated. This theory predicts the Higgs particle and the origin of mass. For the unification of the electroweak and the strong forces, the theory of supersymmetry has been proposed. Here, all particles have a "supersymmetric" partner.

Experiments in particle physics are often conducted in colliders where particles are accelerated to large energies and brought to collide with each other. As our understanding grows and we probe smaller and smaller distances, the energy required to do experiments grows. The experiments thus grow in size and the largest accelerator built so far, the Large Hadron Collider (LHC), is going to collide hadrons at an energy of 14 TeV when it reaches it maximum energy. The work in this thesis has been done

on a prototype particle detector designed for research towards a lepton collider working at 1 TeV. Even though this is 14 times smaller than the collision energy at LHC, working with leptons has its advantages as described below.

1.1 The Standard Model

Particle physics is concerned with the constituents of matter and the fundamental interactions between them, described in the Standard Model (SM). The basic building blocks of matter are spin 1/2 particles thus called fermions, since they follow Fermi-Dirac statistics. Their interactions are described through the exchange of force mediators, the gauge bosons. Mathematically, these bosons are quanta of the fields that mediate the interactions. Three of the fundamental forces, the electromagnetic and the weak and strong forces, are described in quantum field theories (QFTs). Gravity, although affecting all massive particles, is not yet described by a QFT and is therefore not incorporated in the SM. As an example of attempts to formulate a theory for all four forces, String Theory could be mentioned although it has not yet made any predictions that have been validated in experiments. The particles and the Standard Model will be briefly described in this section.

1.1.1 The fermions

The fundamental fermions are divided into two groups: the mentioned leptons and quarks. Leptons interact through the weak interaction and the charged leptons also interact through electromagnetism. They can be said to carry the charges of these interactions. The quarks carry both of these charges and also a third one, called colour. This is the charge of the strong interaction, which means that quarks interact by all three forces described in the standard model. To each particle there is an associated anti-particle which has the same mass but carries the opposite charge.

The leptons

The most commonly found lepton is the electron. It is the lightest charged lepton and an important constituent of normal matter. The leptons are ordered in three families, or generations. Each family contains one negatively charged particle; the electron, the muon and the tauon, each accompanied by a neutrino with zero electric charge. The families are almost identical except for the masses that increase according to the order in Table 1.1.

$$\begin{array}{cccc} -1 & \left(\begin{array}{c} e^- \\ \nu_e \end{array}\right) & \left(\begin{array}{c} \mu^- \\ \nu_\mu \end{array}\right) & \left(\begin{array}{c} \tau^- \\ \nu_\tau \end{array}\right) \\ 0 & & & \end{array}$$

Table 1.1: The leptons arranged according to generation with increasing mass from left to right. The charges, in units of elementary charge, are indicated in the leftmost column.

The quarks

The quarks can also be arranged in three families. The lightest family contains the up (u) and the down (d) quark. These are the particles that, together with the electron, make up most of the matter in the visible universe. The four remaining quarks are the charm (c), strange (s), top (t) and bottom (b) quarks. Quarks and leptons in the heavier families are mostly found in high energy collisions, such as in cosmic radiation that interacts with the atmosphere or in man made experiments. They decay very quickly into lighter particles. The quarks carry a quantum number called $flavour$ which is conserved in

electromagnetic and strong interactions but not in the weak interaction (described below). For example, an interaction involving a strange quark (antiquark) in the initial state has a "strangeness" of 1 (-1). Since this number is conserved, the total strangeness has the same value in the final state if the interaction is not mediated by the weak force.

Particles made of quarks are called hadrons. Hadrons are subdivided into baryons and mesons. Baryons (antibaryons) contain three quarks (antiquarks), e.g. the proton, and mesons consist of a quark and an antiquark.

$$\begin{array}{cccc} +2/3 & \begin{pmatrix} u \\ d \end{pmatrix} & \begin{pmatrix} c \\ s \end{pmatrix} & \begin{pmatrix} t \\ b \end{pmatrix} \\ -1/3 & & & \end{array}$$

Table 1.2: The quarks arranged according to generation with increasing mass from left to right. The top, charm and down quarks are heavier than the other quark in their respective generations. Again, the leftmost column indicates charge in units of elementary charge.

1.1.2 Quantum Field Theory

To date, there are four known fundamental forces of nature: gravity, the strong force, the weak force and electromagnetism. The forces are described in quantum field theories where quanta of the fields act as force carriers. A complete QFT for gravity is however still not realized since the current theory breaks down at the Planck scale. Theoretically, the dynamics of a system can be described by writing down its Lagrangian. The interactions arise as a consequence of demanding that the Lagrangian should be locally gauge invariant. The forces and their mediators are summarised in table 1.3.

Name	Relative strength	Mediators
Strong	1	Gluons
EM	1/137	Photons
Weak	10^{-6}	$W^{\pm}$- and Z-bosons
Gravity	10^{-39}	Gravitons(?)

Table 1.3: The relative strength and mediating particles of the four fundamental forces at normal energies (in terms of their coupling constants), where the graviton has not yet been detected.

Feynman diagrams

A Feynman diagram is a graphical representation of an interaction between fundamental particles. It consists of the interaction points, known as vertices, and lines connecting them which represent the particles of the interaction. Solid straight lines represent fermions while other line types represent bosons, e.g. a wave for a photon. The particles corresponding to the internal lines connecting different vertices are called propagators. By convention, time always flows from left to right.

Feynman diagrams are used to calculate the amplitude for a certain reaction. It depends on the vertices and propagators of the interaction. Simplified, the term from the propagator is given by its virtuality. The terms from the vertices are related to the coupling constants of the participating forces.

The amplitude can then be used to calculate the cross section for a certain process or the lifetime of a certain particle. The parameters of the standard model, such as the coupling constants, are not given by the theory but have to be measured. One way of finding the parameters is to measure the mentioned lifetimes or cross sections.

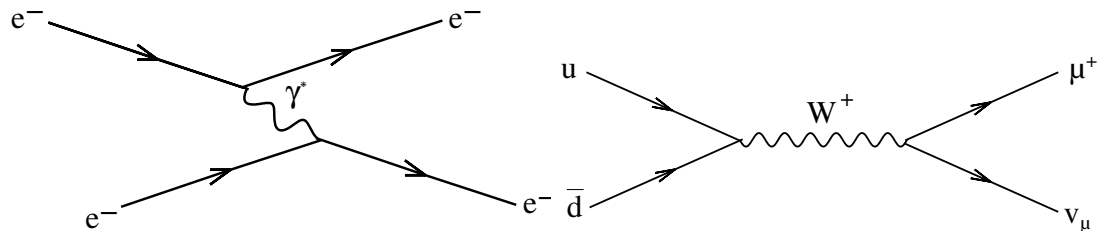

Figure 1.1: Feynman diagrams of electron-electron scattering (left) and pion decay (right).

As an example, electron-electron scattering and pion decay is shown in Fig. 1.1. In the first vertex of the ee-scattering, a virtual photon is emitted by one of the electrons. This is later absorbed by the other electron. The momentum transferred by the photon makes the electrons change their directions of motion. The photon is called virtual because the principle of energy conservation is violated in the first vertex (and the second). This is allowed due to the Heisenberg uncertainty principle which states that

$$\Delta E \cdot \Delta t \sim \hbar$$

where ΔE is the uncertainty in energy, Δt a time interval and $\hbar = \frac{h}{2\pi}$ (h = the Planck constant). Thus, in order to have an interaction, the exchange has to take place within a time allowed by this principle so that the violation in the first vertex is balanced by another violation in the second vertex. The process "borrows" energy from the vacuum to create a virtual particle and then returns it within the time interval given by the uncertainty principle. This will also provide us with a simple explanation for the ranges of the forces. If we use $\Delta E \sim mass$ we see from the uncertainty principle that the mediator's mass determines the range of the interaction, since

$$\Delta t \sim \frac{\hbar}{\Delta E}.$$

A force mediated by a heavy particle will therefore have shorter range than one mediated by a lighter particle. Thus, the electromagnetic force has an infinite range since the photon is massless. This will however not hold for the strong force. Since the gluon is massless the range should be infinite according to the Heisenberg uncertainty principle but it turns out that the range of the strong force is typically the size of a nucleon, i.e. $\sim 10^{-15}$ m. The reason for this will be discussed later.

Electroweak theory and the Higgs mechanism

The electromagnetic force, EM, is described by the theory of quantum electrodynamics (QED) as an exchange of massless photons. The absence of mass gives the interaction infinite range according to the Heisenberg uncertainty principle.

The mediators of the weak force are the W^+-, the W^-- and the Z^0- bosons. The W- bosons mediate the so called charged current reactions that take place whenever electric charge is being exchanged. These reactions are responsible for the flavour changing that occurs for example when a heavier quark or lepton decays into a lighter one. The third boson, Z^0, mediates the neutral current interactions and have a significant role in the unified theory of electromagnetism and the weak force, the so called *electroweak force*, where the photon and the Z^0 are described as different mixtures of two particles, the W^0 and B particles. The gauge bosons of the weak force are very massive particles, which gives the force a short range.

During the 1960's, S.L. Glashow, A. Salam and S. Weinberg showed that the electromagnetic and weak forces could be described by a single theory. From the gauge invariance demand on the Lagrangian, three vector bosons, W^+, W^- and W^0, and a scalar boson, B^0, are obtained. To make the theory conform to experimental observations, the W^0 and B^0 can not be directly identified with the Z^0-boson

$$\begin{pmatrix} \gamma \\ Z^0 \end{pmatrix} = \begin{pmatrix} cos\theta_W & sin\theta_W \\ -sin\theta_W & cos\theta_W \end{pmatrix} \begin{pmatrix} B^0 \\ W^0 \end{pmatrix}$$

Table 1.4: By rotating the B- and W-fields, the experimentally observed photon and Z-boson are recovered in the theory.

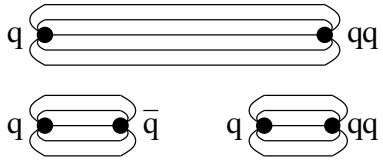

Figure 1.2: The color fields form strings between the quarks of the meson. After a sufficient amount of energy has been desposited in the string, it breaks and a quark-antiquark pair is formed at the breaking point. Two new mesons are thus formed and the quarks are still confined in a hadron.

and the photon. This would, among other things, give the neutrino an electromagnetic interaction which it (empirically) does not have.

The photon and Z^0-boson are obtained by a rotation of the fields W^0 and B^0 as can be seen in Table 1.4. Here, θ_W is called the Weinberg angle or weak mixing angle. Requiring invariance of the Lagrangian under a gauge transformation produces the interactions of the theory but it also forbids the inclusion of a mass term since this will violate gauge invariance. This is no problem in quantum electrodynamics since the photon is massless. For the weak interaction however, the short range indicates large masses of the mediating particles. Experiments also verify this. To solve this, the Higgs mechanism was introduced. Through what is known as spontaneous symmetry breaking, it gives mass to the vector bosons. The mass is aqcuired in the interaction with a field known as the Higgs field which has a non vanishing vacuum expectation value. The combination of fields corresponding to the photon does not get a mass term. In addition to giving mass to the bosons of the weak interaction, the theory predicts a new scalar boson known as the Higgs boson. The discovery of this particle would be a confirmation of the theory but despite great efforts, it has not yet been found.

Quantum Chromodynamics

The strong force is described in the theory of Quantum Chromodynamics (QCD). It affects particles carrying colour charge (red, green or blue) and is mediated by 8 massless bosons called gluons. Even though the gluons have no mass, the interaction has finite range. This is due to the fact that gluons carry colour charge, i.e. a gluon carries one colour and one anti-colour. This leads to gluon self coupling so that the colour field will not spread out radially in space but rather form a so called colour string between the quarks. Since the field line density in the string is constant the force will also be constant. The energy of the string will therefore increase with distance. Because of this the quarks move rather freely inside the hadron (asymptotic freedom) but the force will not diminish when the quarks are moved apart as in EM, confining the quarks within hadrons. When enough energy has been deposited in the string, it is energetically favourable to form a quark-antiquark pair which will result in the splitting of the hadron into two (Fig. 1.2). This is called hadronization and is the process that gives rise to the hadrons observed in experiments as materialization of the incoming kinetic energy. Because of the confinement, quarks are always tied up in colour neutral hadrons and will not be observed on their own.

1.1.3 Gravity

Gravity was first described on a macroscopic scale by Newton in the 17^{th} century. His theory, although flawed, is still in use today since it provides fairly accurate predictions for many applications, with

comparatively easy calculations. In Einstein's general theory of relativity, gravity is explained by the curvature in space-time created by massive objects. This theory successfully accounts for the flaws in Newton's theory. It is not yet possible to formulate a complete quantum field theory for gravity and no mediating particles, gravitons, have been detected. This is one of the great future challenges of physics. However, due to the weakness of the force (gravity is the weakest of the fundamental interactions) and the small masses of the elementary particles, gravity can be neglected when studying high energy reactions.

1.2 Extensions to the Standard Model

There are many areas not covered by the Standard Model that need to be explained. A large issue is the one concerning dark matter. For example, astronomical observations on the motion of galaxies shows a rotational velocity that can not be explained by visible matter alone. Another observation indicating the presence of dark matter is the gravitational lensing effect on light passing large galaxy clusters where the effect on the light indicate a larger mass than what is visually observed. It is believed that only 4 % of the matter content in the universe is made up of visible matter. The rest is made up of 22 % dark matter and 74 % dark energy which is believed to be responsible for the accelerating expansion rate of the universe.

In the theory of supersummetry (SUSY), the particles described previously in this chapter have a "superpartner" where the fermions have a boson partner and vice versa. If SUSY is valid, it will be a broken symmetry or else the superpartners, the "sparticles", would have been found with the masses of the observed particles in the Standard Model. The lightest supersymmetric partner would be interesting as a possible candidate for dark matter [2]. Supersymmetry could also be a cure for quantum effects that should destabilize the Higgs boson at Terascale energies [3].

Another example is neutrino masses. In the Standard Model, they are massless but the observation of neutrino oscillations reveal that they do have non zero masses [4]. To accomodate this, the theory needs to be extended. This could be experimentally tested by detecting the new gauge bosons that should arise [3].

Chapter 2

The international linear collider

Particle physics is often called high energy physics because most experiments are carried out at facilities that accelerate particles to extremely high energies and collide them in order to study the outcome. In one way or another, all accelerators work by applying electric fields to charged particles. This means that any stable particle that carries charge could be used as the basis for such an experiment. The LHC, for example, is designed to accelerate either protons or heavy nuclei. As we shall see, it is easier to accelerate heavy particles such as protons to very high energies than to accelerate e.g. electrons. This is however not the end of the matter. When it comes to analyzing the results, electrons are better suited for precision measurements because of the simple initial conditions and clean signals that they provide. Protons have an inner structure that greatly complicates calculations and collisions between them give rise to a lot of background to the fundamental phenomenon under study. Because each technique, colliding hadrons and electrons respectively, has its advantages and disadvantages they are thought to complement each other. A lepton collider is therefore being proposed as the next large facility to sort out the details of what is discovered at LHC. The suggested *International Linear Collider*, (ILC), is described in this chapter. This is of course under development so the design described here should be thought of as an example. Fig. 2.1 shows a schematic picture of the suggested design. Other proposals include the *Compact Linear Collider* ($CLIC$) and a muon collider. CLIC would be using normal conducting cavities for the acceleration rather than the superconducting ones envisioned for the ILC. This would make it possible to go to higher energies than the ones reachable with superconducting technology since it is fundamentally limited to lower acceleration gradients [5]. A muon collider would make it possible to use a circular accelerator ring since muons, being heavier than electrons, do not lose as much energy

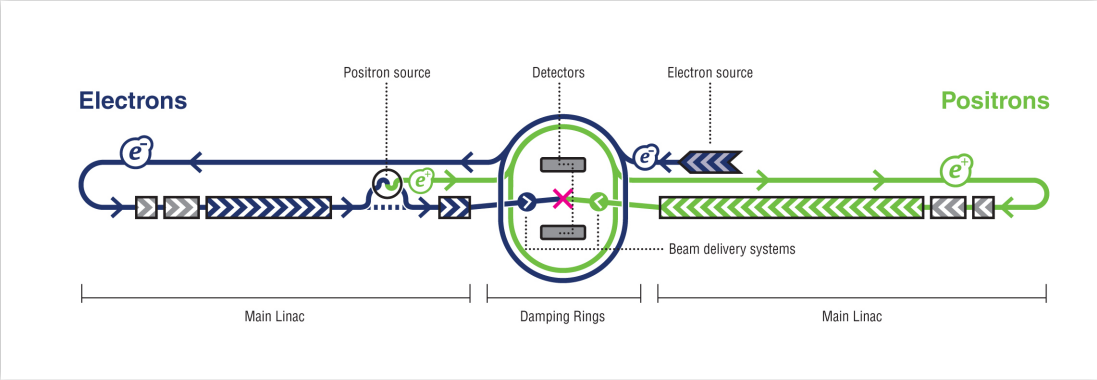

Figure 2.1: Sketch of the ILC. [6]

as electrons do in such a design (described below).

2.1 Motivation

The most powerful collider in history (the LHC) is in the beginning of its operation. When it is in full operation its *center of mass* (CM) [1] energy will be 14 TeV. Why then build a lepton collider capable of only a fraction of the LHCs CM energy? As mentioned, one of the answers is precision. The LHC has a higher energy but suffers from large backgrounds, i.e. a large number of particles are produced, due to the composite structure of the collided particles, and it can be difficult to sort out interesting events. The collisions take place between the constituents of the accelerated particle, i.e. the quarks and gluons. Not only do they each carry just a fraction of the total momentum but this fraction is not known in the individual collision which means that particles collide at a wide range of energies, making precision studies difficult. A lepton collider on the other hand has the advantage of a well known initial state where the first interaction is electromagnetic and takes place between particles without substructure. This is an advantage since the electromagnetic interaction can be more accurately calculated than the strong interaction, and leads to less background because the colliding particles are pointlike. Background in this case means particles from the collision that are not of interest to the studied process. The simple initial state means that almost the entire beam energy, excluding some losses to e.g. beamstrahlung (photon radiation from an incoming particle due to interaction with a positron (electron) bunch from the opposite beam), goes into the initial collision, in contrast to the case in hadron colliders where the colliding partons carry a varying fraction of the total energy. Thus, the precision is given by the energy spread of the electron and positron beams. The well defined initial energy offers the possibility to tune the beam energies in order to scan over resonances and production thresholds. The low background allows the exploration of low cross-section processes. Also, the use of polarized beams makes it possible to enhance signal rates since many reactions depend on the polarization of the initial particles.

The goal of precision measurements sets high requirements on the detectors. In the case of a low mass Higgs boson for instance, the momentum resolution $\delta(1/p)$ needs to be at least below $7 \times 10^{-5} GeV^{-1}$ [7]. All detector options aim at a momentum resolution of about $5 \times 10^{-5}\ GeV^{-1}$ or better [8]. Fig. 2.2 shows the importance of momentum resolution for distinguishing a possible Higgs signal from the background.

2.1.1 Possible studies at the ILC

One of the most important tasks for the ILC is of course to participate in the search and study of the Higgs boson. As mentioned, the Higgs boson is yet to be detected and when (if) it is finally discovered its properties need to be investigated. The ILC is a good choice for precision measurements considering the advantages with an e^+e^- collider mentioned above. It is very probable that the Higgs boson will be detected at the LHC when it gets fully operational. However, because of the mentioned drawbacks of hadron collisions, precision measurements need to be done elsewhere. The ILC is very well suited for this.

In e^+e^- collisions, Higgs bosons are mainly produced in Higgs-strahlung and WW-fusion. For the mass range where the Higgs probably lies, somewhere between the limits 115 and 200 GeV, as set by previous experiments, the cross sections for the two processes are roughly the same for a collision energy of 500 GeV, which is the CM energy of the ILC before upgrades, see Fig. 2.3[3].

In Higgs Strahlung (Fig. 2.4), an excited Z boson is created through annihiliation of the colliding particles. Subsequently, a Higgs boson is radiated from the Z*, leaving an on-shell Z boson and the Higgs. The WW-fusion process contains two vertices where the electron (positron) splits into a W-(W+) and an

[1] In a collider, the CM energy is the energy available for particle production. If the colliding beams are of equal energy, this is just the sum of the beam energies.

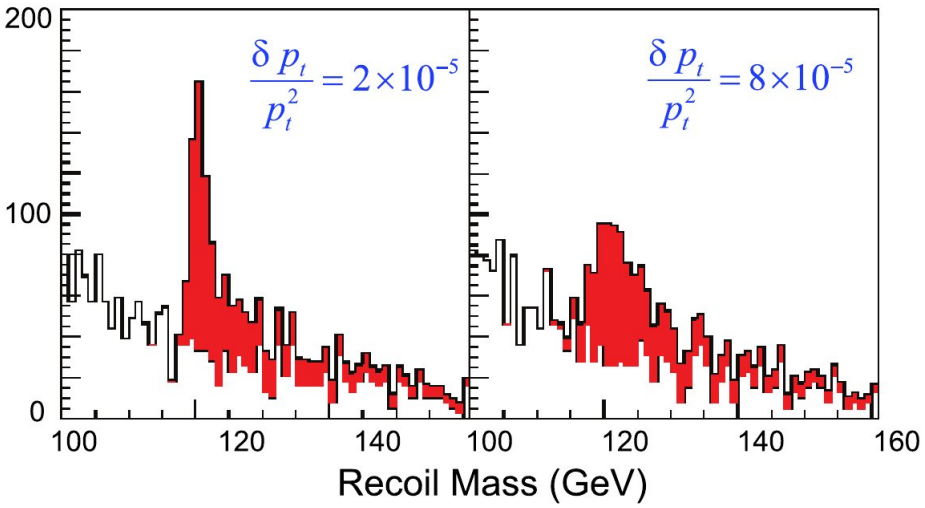

Figure 2.2: Illustration of the impact of detector resolution on the ability to measure the Higgs mass using the recoil mass technique, explained in section 2.1.1[3].

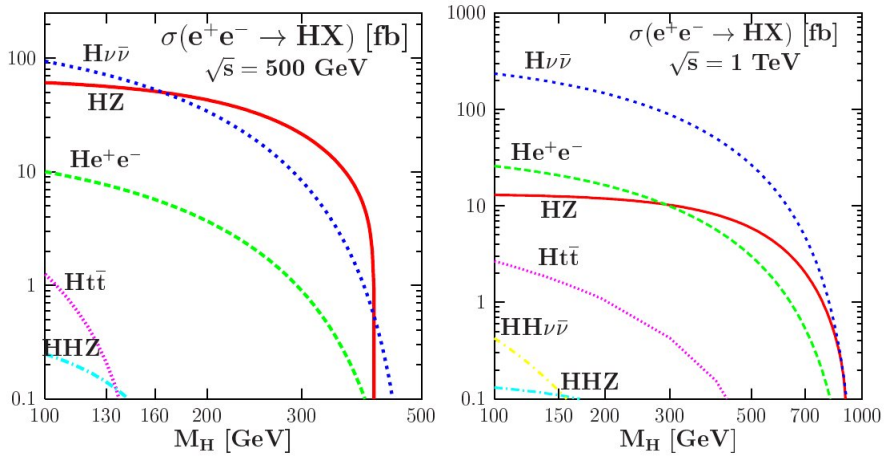

Figure 2.3: Higgs production cross sections as a function of Higgs mass for a center of mass energy of 500 GeV (left) and 1 TeV (right) [3].

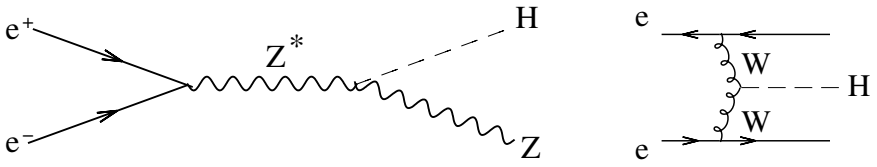

Figure 2.4: Left: The Higgs-strahlung process. The colliding electron and positron annihilate to create an excited Z-boson, which then deexcites by radiating a Higgs boson. Right:WW-fusion. The W-bosons annihilate to create a Higgs boson.

antineutrino (neutrino). The W-bosons then annihilate with a Higgs-boson as result. As an example of mass measurements, the Higgs-strahlung will be discussed a little further. The Higgs mass can be determined with great accuracy by measuring the energy of the final Z-boson in the Higgs strahlung process and calculating the recoil mass. This recoil mass technique uses the leptonic decay channel of the Z-boson. Since the initial beam energies are sharp (provided that beamstrahlung is suppressed), the Higgs mass can be determined from the reconstructed energy of the Z boson obtained from the lepton pair as $m_H^2 = s + m_Z^2 - 2E_Z\sqrt{s}$ [8]. Here, s is the center of mass energy and m_Z and E_Z is the mass and reconstructed energy of the Z-boson, respectively. This technique also makes it possible to measure the production cross section without having to take the decay modes of the Higgs boson itself into account. Normally the Higgs mass and the production cross section has to be determined from the decay products of the Higgs boson. Here, the measurements are independent of the nature of the Higgs boson, i.e. whether it is best described by the Standard Model or another theory such as SUSY. The ability to measure the mass of the recoiling system relies heavily on how accurately the momentum of the Z decay products can be measured, as shown above in Fig. 2.2. Evidently, this method can not be used in hadron collisions since the initial energy is not known well enough.

In addition to measuring the properties of a possible Higgs boson, it will be possible to investigate a range of new physics cases. The mass of some of the particles predicted by SUSY are potentially within the range of the ILC. Depending on the mass of a new boson hypothesized within a number of possible extensions to the standard model, the so called Z' boson, it too might be detected. Also in these cases, the ILC can do the precision measurements not possible at the LHC.

Not only new physics will be considered. Already discovered particles can also be studied with high precision. Important processes, such as top quark pair production, are within reach of the ILC. The ILC will make it possible to measure the top mass to within 100 MeV [9] compared to the present precision of about 1.6 GeV [10].

Many of the envisioned measurements can benefit from the well defined initial state and the ability to tune the beam energies which will allow to scan over production thresholds or set the energy to a region where the sought particle should be, perhaps pointed to by the LHC.

2.2 Colliders

A collider experiment uses energetic particle beams to create highly energetic collisions. The beam is obtained with an accelerator through the application of oscillating electric fields to the beam particles. The collider principle is advantageous since the CM energy, $\sqrt{s}$, is equal to the sum of the beam energies (if the energies and particle types are the same) whereas in a fixed target experiment for example, the center of mass energy is only a fraction of the total beam energy. Thus, colliders are preferred since all of the energy is available for particle production.

An important property of a collider is the luminosity, $\mathcal{L}$, necessary to convert the measured rate for a process, n, to a cross section. The luminosity is related to the beam intensities and the size of the area to which the beams are focused. We can get the expected rate of a certain process by multiplying the

luminosity with the cross section for that process, $n = \sigma\mathcal{L}$.

2.3 Why a linac?

The dominating accelerator designs for high energies are linear accelerators (linacs) and synchrotrons. In a synchrotron, the particles are accelerated in radio frequency (RF) cavities and constrained to circular paths by bending magnets with strong magnetic fields. The particles can in this way pass the same RF cavity many times (in LHC a proton moving at near the speed of light will make about 11,000 revolutions per second) and be further accelerated. This is an advantage compared to linacs, where the particles only pass the cavities once. The circular design has so far been preferred over the linear since it has allowed for acceleration to high energies with smaller machines and simpler acceleration cavities. The synchrotrons do however suffer from a severe limitation. Since the accelerated particles move in a circular orbit, they will emit synchrotron radiation. The energy ΔE radiated by a particle per turn is given by

$$\Delta E = \frac{q^2\beta^3\gamma^4}{3\epsilon_0 R} \text{ [39]}, \tag{2.1}$$

where q is the particle charge, $\beta \equiv \frac{v}{c}$ is the particle velocity in units of the speed of light, $\gamma \equiv \frac{1}{\sqrt{(1-\beta^2)}}$ is the particle gamma factor, ϵ_0 is the permittivity of free space and R is the radius of the accelerator.

It is clear, since $\gamma = E/m$ in natural units and $\beta \to 1$ as v approaches the speed of light, that the energy loss grows rapidly (as the fourth power) with E and also that they are inversly proportional to the fourth power of m. The losses will therefore be more severe when accelerating electrons, which is what we want to do here, than heavier particles like protons. Increasing the radius will of course bring down the losses but that approach has its practical limits since the losses go as E^4 but only as $\frac{1}{R}$. The particle physics community has therefore decided to make the next generation e^+e^--collider a linear one which will not suffer from such energy losses. The ILC is aimed at an initial center of mass energy $\sqrt{s} = 500$ GeV with a planned upgrade to 1 TeV. Of course, the use of a linac also has its drawbacks. The first thing that comes to mind is the loss of non-colliding particles, i.e. when the beams cross, very few particles will participate in an interaction. In a synchrotron, this is not a problem since the bunches circulate and are available for collisions on the next turn. In a linac, the particles that do not collide are lost. By focusing the beams to a small transverse size ($\sim nm$), a high luminosity can still be attained. The luminosity goal for the 500 GeV collider is 2×10^{34} cm$^{-2}s^{-1}$ [7].

2.4 The accelerator

During the last two decades, superconducting RF (Fig. 2.5) cavities have been developed that have increased the possible acceleration gradient dramatically from 5MV/m (megavolts per meter) to the 31.5MV/m wanted for the ILC project. There are even cavities in development that has achieved 50MV/m, which is close to the physical limit. The challenge now is to enable mass production since the ILC needs about 17,000 1 meter long cavities. [7]

The highly polarized electron beam (with a polarization of up to 80 %) is produced in a DC photocathode gun. When the electrons have been accelerated to 150 GeV they are used to generate the positrons for the positron beam. By passing the electron beam through an undulator before it is returned to the main beamline, high energy photons are produced. They are in turn directed onto a Ti-alloy target where electron-positron pairs are produced. The electrons from the pair production process are diverted and dumped, leaving a beam of positrons to be accelerated in a similar way as the electron beam.

The electron bunches will have a tendency to spread out in the transverse direction. To reduce the emittance, i.e. the bunch size in phase space, damping rings operating at 5 GeV are used. This ensures

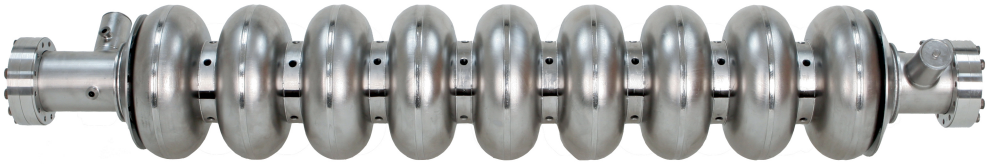

Figure 2.5: A superconducting niobium RF cavity [7].

a high interaction rate since a spread out beam will have fewer collisions. In the damping rings, the particles lose energy due to synchrotron radiation and are reaccelerated in rf cavities along the rings. Since the particles lose momentum in all directions but are only reaccelerated in the direction along the beam the result is that the particles in the bunches get a more parallell direction of motion. Thus, they will not spread out as much during the main acceleration which will give a smaller beam size and therefore a higher luminosity. The ILC design calls for one electron ring and one positron ring, both with a circumference of 6.7 km.

After the damping rings, the beams are transferred to the main linac via a Ring to Main Linac (RTML) system. In addition to transporting the beam it also performs a number of additional tasks such as turning the beam around, orienting the beam polarization in the desired direction, bunch compression and acceleration to 15 GeV.

The main acceleration is taking place in two 11 km long linacs. The goal energy is 250 GeV which is achieved through the use of superconducting RF cavities with an average accelerating gradient of 31.5 MV/m. For the upgrade to 1TeV, the length of the accelerator will be increased.

The result of the acceleration will be a pulsed beam with bunches containing $1 - 2 \times 10^{10}$ electrons (positrons) at a rate of 5 Hz, where the bunches will arrive in trains containing 2820 bunches. The typical bunch size at the interaction point (IP) is 640×5.7nm [7].

After the linacs, the beams are taken care of by the Beam Delivery System (BDS) which among other things is responsible for focusing the beams after acceleration and making them collide at the IP. Around the IP, a detector will be built to study the results of the collisions.

2.5 Detector

To reach the design goals and be able to perform the desired measurements, detector performance has to be improved considerably compared to the experiments of today. Many of the studied processes result in multi-jet final states. The reconstruction of jet energies will thus be important in order to identify the initial interaction and the participating particles. For example, if the Higgs mass is small enough to have reasonable branching ratio to b-quarks, its mass can be determined by using the 4-jet channel where the Z-boson decays into a quark-antiquark pair. An advantage with this method is the larger statistics obtained from hadronic Z-boson decay compared to leptonic decay. The required jet energy resolution can be achieved by using the particle flow concept described for example in [8].

The aspect most relevant for the topic of this thesis is the momentum resolution. One factor deciding the required resolution is again the measurement of Higgs mass through the recoiling Z-boson in the Higgs strahlung process. When the Z-boson decays leptonically, the invariant mass can be determined through the momenta of the leptons. This puts some requirements on for example the accuracy of the beam energy. For the detector, it means that a high momentum resolution is necessary.

A number of detector concepts are being explored for the ILC. At least one, the International Large

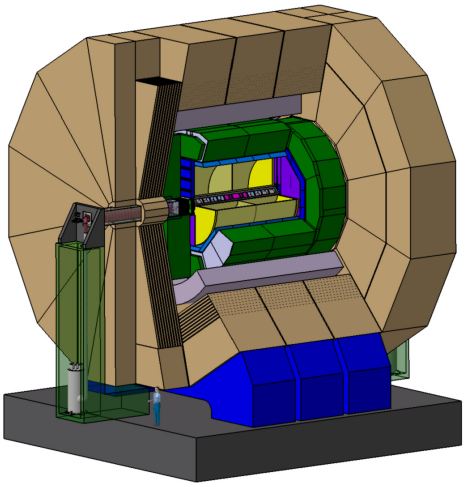

Figure 2.6: The ILD detector concept [11].

Detector (ILD), relies on a Time Projection Chamber for tracking. Fig. 2.6 shows a schematic picture of the ILD concept. A brief summary of its subsystems is given here.

The detector closest to the IP is a barrel shaped multi layer pixel vertex detector (VTX) optimised for excellent point resolution and low material budget. Surrounding the VTX is a system of strip and pixel detectors. Two layers of strip detectors sit in between the VTX and TPC as intermediate tracker (SIT) and in the large rapidity region a number of forward tracking disks (FTD) consisting of Si pixel and strip detectors provides tracking. Main tracking is provided by a large time projection chamber (TPC) which allows measurement of up to 224 individual points per track over a length of about 1.3 m. The envisaged point resolution of the TPC is less than 100 μm in the bend plane and 500 μm in the drift direction. The TPC is described in more detail later. A prototype TPC has been developed within the LCTPC (Linear Collider TPC) collaboration which is the topic of this thesis. Another system of Si strip detectors, the silicon external tracker (SET) around the TPC and the end cap tracking detector (ETD) behind the TPC endcap, provide additional points to improve the tracking. Two calorimeters, one electromagnetic (ECAL) and one hadronic (HCAL), are used to provide energy measurements of leptons and hadrons, respectively. The designs are not yet settled upon since two different options are being considered in both cases. A superconducting solenoid encloses the system and generates a magnetic field of 3.5 T which is the basis of momentum measurements since charged particles are forced into curved trajectories. The iron return yoke, in addition to returning the magnetic flux, is instrumented with a muon detection system.

Chapter 3

Time projection chambers

The time projection chamber (TPC) is an advanced particle detector for detecting charged particles. It is capable of 3D tracking and if placed in a solenoidal magnetic field momentum measurements and particle identification through energy loss (dE/dx) measurements.

The time projection chamber was proposed in 1974 by David Nygren at the Lawrence Berkeley Laboratory (LBL). It was invented for the PEP-4 detector used in the PEP experiment at SLAC. Since then, TPCs have been used in numerous experiments such as the LEP detectors and more recently in the ALICE detector at the LHC at CERN and the STAR experiment at the Relativistic Heavy Ion Collider in Brookhaven.

The TPC comes with a number of advantages:

- Particle identification is simplified since tracking, energy loss measurements and momentum measurements are done at the same time which, with an efficient track recognition software, minimizes the risk of falsely associating measurements coming from different tracks. If for example tracking was done in one detector and energy loss measurements in another, a recorded track of one particle could be associated with the energy measurement of another, especially in an environment with a high track density.

- If the energy loss measurement is done using a truncated mean of the deposited energy at the track measurement points it is also possible to remove data points that have a distorting influence on the result such as delta electrons, as explained in section 3.3.2.

- An important advantage with a TPC is that it presents a low amount of material for the traversing particles, thus limiting the energy loss of the particles. This is good for subsequent energy measurements in the surrounding calorimeters since the energy deposited in the TPC is kept to a minimum.

- The large number of measurement points and the high point resolution is advantageous for track reconstruction and provides a good momentum and dE/dx resolution. The particle tracks are measured over a long distance, which is also advantageous for momentum resolution.

This chapter will first give an overview of the TPC envisaged for the ILD. Then, a general description of TPCs is given before a more detailed treatment of the subsystems and principles.

3.1 The ILD TPC

A TPC, being the main tracking detector in the ILD proposal, is suggested for a number of reasons. For example it offers a large number of space points which in combination with the long tracks can give a high momentum resolution. The track finding efficiency is as high as 99 %. It also has a low material budget which is an obvious advantage for the subsequent energy measurements in the calorimeters and minimizes the interactions with the endplate of the $\sim 10^3$ photons per event due to beamstrahlung in the forward direction [12]. A high magnetic field limits transverse diffusion of the drifting electrons used to obtain an image of the track. This improves the space point resolution and therefore also the momentum resolution which in turn gives good particle identification from combined momentum and energy loss measurements. No combinatorial background, i.e. incorrect combination of measurements from different tracks, arises if momentum and energy loss of a track can be measured in the same detector at the same time, which is the case with a TPC.

3.1.1 Performance

The requirements on the TPC performance comes of course from the measurements that are going to be performed. The previous example of recoil measurements on the Higgs strahlung process is one of them. As mentioned, momentum resolution is important here.

The momentum resolution goal for the ILD TPC is

$$\delta(1/p_T) \approx 9 \times 10^{-5}\ GeV^{-1}[11] \tag{3.1}$$

Note that this is only for the TPC. The combined momentum resolution goal for the TPC, the SET, the SIT and the VTX is

$$\delta(1/p_T) \approx 2 \times 10^{-5}\ GeV^{-1}[11] \tag{3.2}$$

which should be sufficient to determine the Higgs mass with a precision of around 150 MeV [8]. This in turn puts requirements on the point resolution σ in the $r\phi$-plane since they are linked through the Glückstern equation,

$$\frac{\delta_{P_T}}{P_T} = \frac{\sigma P_T}{0.3L^2B}\sqrt{\frac{720}{N+4}}[13] \tag{3.3}$$

where B is the magnetic field, L is the track length and N is the number of measured points. The spatial resolution is required to be better than 100 μm in the $r\phi$-plane and about 0.5mm in the drift direction [11]. Table 3.1 gives an overview of the goal design parameters of the ILD TPC.

3.2 Principle

A Time Projection Chamber (TPC) usually consists of a gas filled cylindrical drift volume. Fig. 3.1 shows a simple sketch of a TPC. The basic idea is that a charged particle with enough energy will ionize the gas when passing through the detector. A uniform electric field is applied over the drift volume, usually with anodes at the two ends of the chamber and the cathode in the middle, dividing the chamber in two halves. [1] Thus, ionization electrons drift towards the anode where the segmented readout structure measures charge, location and arrival time. The uniform field is provided by a field cage made up of

Size	ϕ = 3.6m, L = 4.3m outside dimensions
Momentum resolution (3.5T)	δ (1/pt) $\sim$ 9 $\times 10^5$/GeV/c TPC only ($\times$ 0.4 if IP incl.)
Momentum resolution (3.5T)	δ(1/pt) $\sim$ 2 $\times 10^5$/GeV/c (SET+TPC+SIT+VTX)
Solid angle coverage	Up to cos $\theta \simeq 0.98$ (10 pad rows)
TPC material budget	$\sim 0.04 X_0$ to outer fieldcage in r $\sim 0.15 X_0$ for readout endcaps in z
Number of pads/timebuckets Pad size/no.padrows σpoint in rϕ σpoint in rz 2-hit resolution in rϕ 2-hit resolution in rz dE/dx resolution	$\sim 1\times 1^6$/1000 per endcap $\sim$ 1mm$\times$4–6mm/$\sim$200 (standard readout) $\leq 100\mu$m (average over $L_{sensitive}$, modulo track ϕ angle) $\sim$ 0.5mm (modulo track θ angle) $\sim$ 2mm (modulo track angles) $\sim$ 6mm (modulo track angles) $\sim$ 5 %
Performance Background robustness Background safety factor	$>$ 97 % efficiency for TPC only ($p_t >$ 1GeV/c), and $>$ 99% all tracking ($p_t >$ 1GeV/c) Full efficiency with 1 % occupancy, Chamber will be prepared for 10 $\times$ worse backgrounds at the linear collider start-up

Table 3.1: Goal design parameters of the ILD TPC[11].

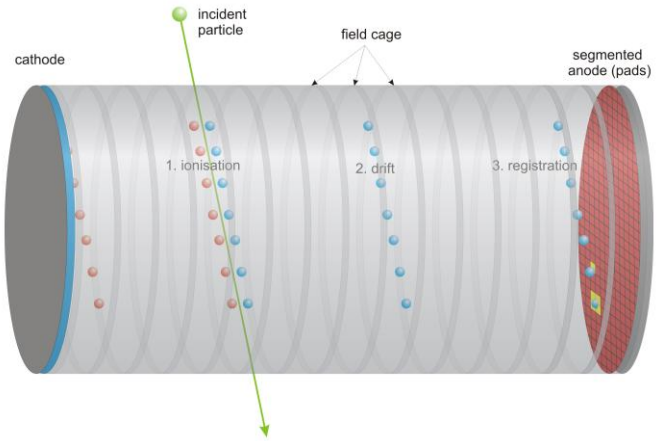

Figure 3.1: Working principle of a TPC. Here we see the traversing particle ionizing the gas, leaving a trail of electrons and positive ions along its path[14].

conducting strips placed along the chamber walls which are kept at appropriate potentials to shape the field to a high degree of uniformity.

In a collider, the TPC can be built around the interaction point (IP) so that the beam pipe goes through its central axis which means that almost all directions around the IP are covered. As mentioned, charged particles traversing the detector volume will lose energy to the gas, thus ionizing the gas molecules and leaving a trace of electrons and positive ions in their wake. The electrons produced in this way are called *primary electrons*. The electric drift field usually has a magnitude on the order of a few hundred V/cm which gives the electrons a high drift velocity and therefore a low drift time to one of the chamber's end plates and the readout apparatus. This has usually been made up of a system of anode wires similar to the one found in a Multi Wire Proportional Chamber (MWPC) and rectangular cathode segments ("pads") underneath the wires. The function of the wires is to amplify the signal since a particle will leave a trail containing on the order of 100 electrons/cm which is too few for effective electronic detection. As a drifting electron approaches an anode wire, the large field close to the wire (the field goes a $1/r$ where r is the distance from the the wire center) accelerates the electron which enables it to liberate more electrons, *avalanche electrons*, from the gas and a so called avalanche is formed. Behind the wires, a signal is at the same time induced on a number of cathode pads underneath the wires by the backdrifting avalanche ions. One of the coordinates in the plane perpendicular to the cylinder axis is thus determined by the anode wire and the other coordinate is given by the signals on the cathode pads. Since the drifting electrons undergo multiple collisions with the gas molecules as they drift, they will diffuse outwards from the original point of ionization. The charge is thus distributed over the cathode pads such that the amplitudes are forming a gaussian distribution with its peak giving the coordinate of the track point to a higher precision than the size of the pads.

[1]It is of course also possible to have only one anode which is the case in the TPC prototype studied in this thesis.

In the ILD there will be no anode wires. Instead, two types of Micro Pattern Gas Detectors (MPGDs) are under consideration. These are Gas Electron Multipliers (GEMs) and Micro Mesh Gas amplifiers (Micromegas). These techniques are fairly new and come with a number of advantages compared to the anode wire solution, among which are better resolution and less distortions caused by non-parallell electric and magnetic fields. [2]

The readout, whether it comes from the traditional solution with wire readout or MPGDs, will give a two dimensional projection of the track on the readout plane. To get a full three dimensional reconstruction, a third coordinate is needed. It is given by the drift time of the ionization electrons which is measured as the time it takes for the electrons to drift from the collision point to the pad. If the drift velocity of electrons in the particular gas mix and field strength is known and constant throughout the detector volume (which it will be with a homogeneous field), the drift time can easily be converted into a distance and so a three dimensional image of the track can be reconstructed. The coordinate system of a detector is usually set up with the z-coordinate along the beam so that in a TPC the drift is along z-axis. Thus, the readout plane corresponds to the xy-plane or, equivalently, the $r\phi$-plane.

In addition to position measurements, momentum and energy loss of the traversing particle can also be reconstructed. If a solenoidal magnetic field is applied over the detector volume, a charged particle will describe a curved trajectory. If the measured space points are combined to a track, the curvature can be used to measure the momentum. Furthermore, since the number of primary electrons is related to the energy loss of the traversing particle, the measured charge can be related to the energy loss of the particle if the number of secondary electrons from the amplification device is proportional to the number of primary electrons.

3.3 Energy loss

For particle identification, measurements of energy loss are important. The energy loss of a particle in a gaseous detector causes ionization of the gas molecules. The distribution of ionization electrons per unit length is related to the mean energy loss which means that the number of primary electrons can be taken as a measure of the energy deposited in the gas by the traversing particle. Therefore, it is important to understand the energy loss mechanism.

A charged particle traversing a gas (or any material) will lose energy due to interactions with the material, causing the ionizations and excitations mentioned above. To describe the mean energy loss per unit length, dE/dx, in the interval $0.1 < \beta\gamma < 1000$, where β and γ are defined below, the Bethe-Bloch equation is usually used.

Below this interval, one of the assumptions used in deriving the equation, that the impacted shell electron can be taken to be free and at rest compared to the incoming particle, is no longer valid. Above the interval, radiative effects become important (this happens earlier for electrons which will be dealt with below). The Bethe-Bloch formula is given by

$$-\frac{dE}{dx} = 2\pi N_a r_e^2 m_e c^2 \rho \frac{Z}{A}\frac{z^2}{\beta^2}\left[\ln\left(\frac{2m_e\gamma^2 v^2 W_{max}}{I^2}\right) - 2\beta^2 - \delta - 2\frac{C}{Z}\right] \text{[15]} \tag{3.4}$$

where

[2] If the magnetic field is not aligned properly with the electric field, the drift direction of the electrons will not be exactly parallell to the electric field (and the chamber axis). Instead, a component due to a term proportional to the vector product between the two fields will distort the drifting electrons from their straight trajectories. This $\mathbf{E} \times \mathbf{B}$-effect will be dealt with in more detail below.

r_e is the classical electron radius
m_e is the electron mass
N_a is Avogadro's number
I is the mean excitation potential
Z is the atomic number of the absorber material
A is the atomic weight of the absorber material
ρ is the density of the absorber material
z is the charge of the incident particle in units of elementary charge
β is the velocity of the incident particle in fractions of c
γ is the gamma factor $1/\sqrt{1-\beta^2}$ of the particle
W_{max} is the maximum energy transfer in a single collision
C is the so called *shell correction* which is important for highly relativistic particles
δ is the so called *density correction* which is important at low velocities

From the Bethe-Bloch formula, we see that for a specific target material the energy loss varies with velocity and the particle charge Z. A combined measurement of the momentum and of the energy loss can be used to identify the particle, i.e. to determine its mass.Fig. 3.3 shows the energy loss for a number of different particles as a function of momentum where it is clear that different particles follow different curves. Particles at the minimum of the curve are called *minimum ionizing*. Before reaching the point of minimum ionization, the dE/dx curve of a certain particle is distinctly different from the one followed by another particle type. This is good for particle identification. After the minimum ionization point (on what is known as the relativistic rise) the curves are not as well separated and particle identification using this method becomes difficult.

3.3.1 Corrections for electrons

One of the assumptions used in deriving the Bethe-Bloch equation is that the mass of the ionizing particle is much larger than the mass of the electron. Therefore, the formula is not valid when the ionizing particle itself is an electron. With its small mass, the emission of bremsstrahlung becomes important. Above an energy of the order of 10's of MeVs, bremsstrahlung dominates the energy loss completely [15].

To begin with, the Bethe-Bloch formula has to be modified to account for the low mass of the electron. An approximation made in the original derivation, that the incident particle remains undeflected, is no longer valid. Also, the collision is between two identical particles which has to be taken into account. The formula now becomes

$$-\frac{dE}{dx} = 2\pi N_a r_e^2 m_e^2 c^2 \rho \frac{Z}{A}\frac{1}{\beta^2}\left[\ln\frac{\tau^2(\tau^2+2}{2(I/m_e c^2)^2} + 1 - \beta^2 + \frac{\frac{\tau^2}{8} - (2r+1)\ln 2}{(\tau+1)^2} - \delta - 2\frac{C}{2}\right] \text{[15]} \tag{3.5}$$

where τ is the kinetic energy of the particle in units of $m_e c^2$.

Second, as mentioned, energy loss from bremsstrahlung becomes important for electrons because of their low mass. The cross section for bremsstrahlung emission varies as the inverse square of the particle mass which is the reason why other particles are not significantly affected by bremsstrahlung emission (at least not before reaching hundreds of GeVs). The energy loss due to radiation can be written as

$$-\left(\frac{dE}{dx}\right)_{rad} = N\int_0^{\nu_0} h\nu \frac{d\sigma}{d\nu}(E_0,\nu)d\nu \text{ [15]} \tag{3.6}$$

where E_0 is the initial energy of the electron and $h\nu$ is the energy of the bremsstrahlung photon, $N = \rho N_a/A$ and $\nu_0 = E_0/h$. The total energy loss can largely be described as a sum between the collision loss (from Bethe-Bloch) and the loss due to radiation given by eq. 3.6. Fig 3.2 shows how the bremsstrahlung losses completely dominate the collision losses for higher energies and Fig. 3.3 shows that the electron energy loss curve does not have the same shape as the other curves.

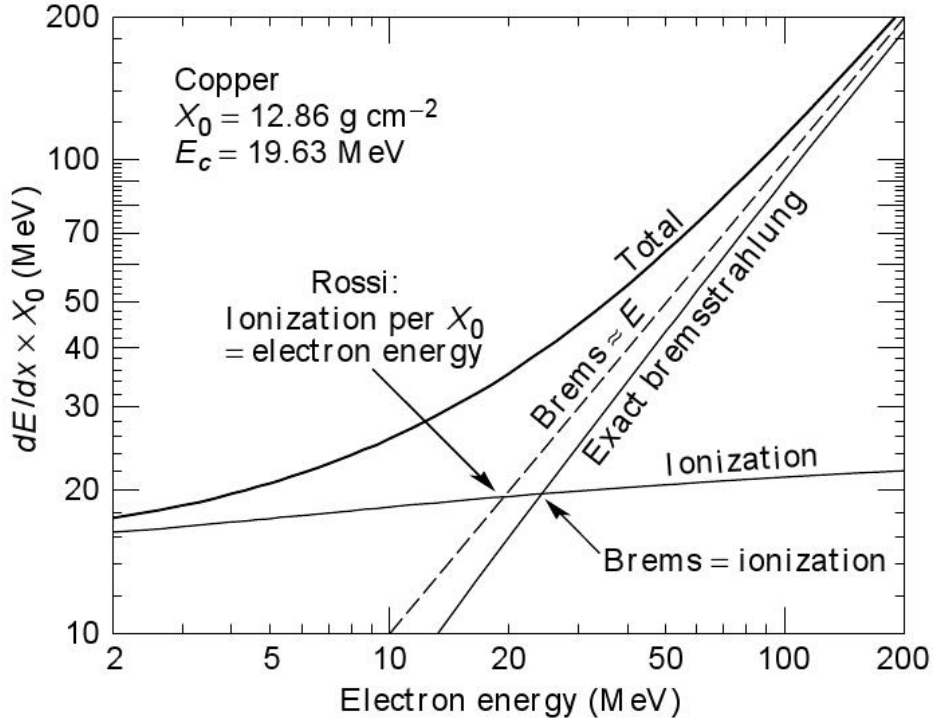

Figure 3.2: The electron energy loss per radiation length, dE/dx, as a function of electron energy. The energy loss from bremsstrahlung is dominating after around 10 MeV (here in copper). Here we see two definitions of the critical energy E_c, usually defined as the energy at which E_{col}, the energy loss due to collisions, and E_{rad} are equal [10].

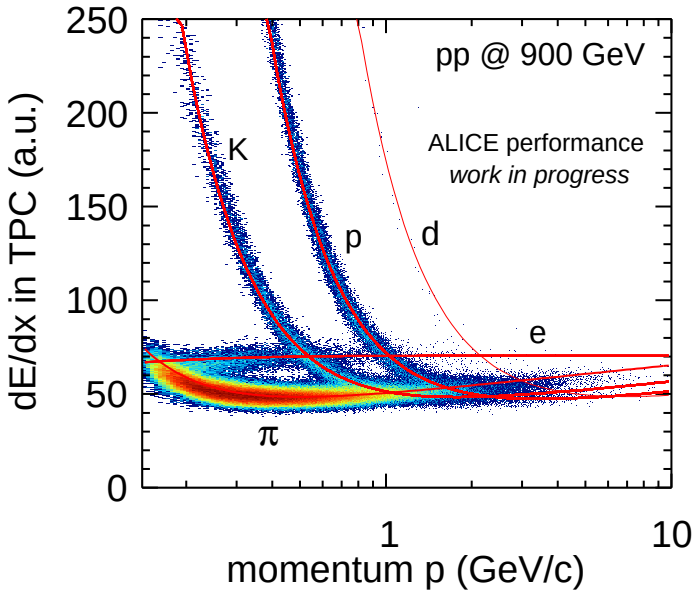

Figure 3.3: Energy loss per unit path length, dE/dx, as a function of momentum for different particles measured in the Alice TPC.

3.3.2 The energy loss distribution

Since the Bethe-Bloch equation describes the mean energy loss, the shape of the energy loss distribution will tend towards a normal distribution when the number of interactions is large, such as in a thick absorber. In a thin absorber and in a gas however, the mean will be considerably biased toward large energies due to rare large energy transfers in a single collision. The possibility for a large single energy deposit gives the distribution a tail towards higher energies so that it follows a Landau distribution. In a gas, these large energy deposits can create so called "delta electrons" that receive a large momentum compared to other ionization electrons and can travel several millimeters in the detector volume and give rise to new ionizations. Delta electrons can often be seen as an offshoot from a particle track, spiraling rapidly because of the magnetic field. Most energy loss detectors measures the total signal including the less frequent delta electron events, i.e. the Landau tail. The TPC, by means of the very large number of $\frac{dE}{dx}$-values, gives the possibility to find these events and remove them, thus providing a better $\frac{dE}{dx}$-measurement. This is called a truncated mean, which is the mean of the energy when the largest values have been removed, and is often used as a more reliable estimator of the mean energy loss [10].

3.3.3 Ionization yield

As mentioned in the beginning of this section, the number of ionization electrons can be related to the energy deposited by the traversing particle. The average number of electrons per unit length, n_e, is basically

$$n_e = \frac{\Delta E}{W} \tag{3.7}$$

where ΔE is the energy deposited per unit length and W is the average energy needed to create an electron-ion pair in the specific gas. W is, albeit different for different gases, generally on the order of 30 eV [15] and shows no general correlation with the ionization potential of the gas. Much energy goes

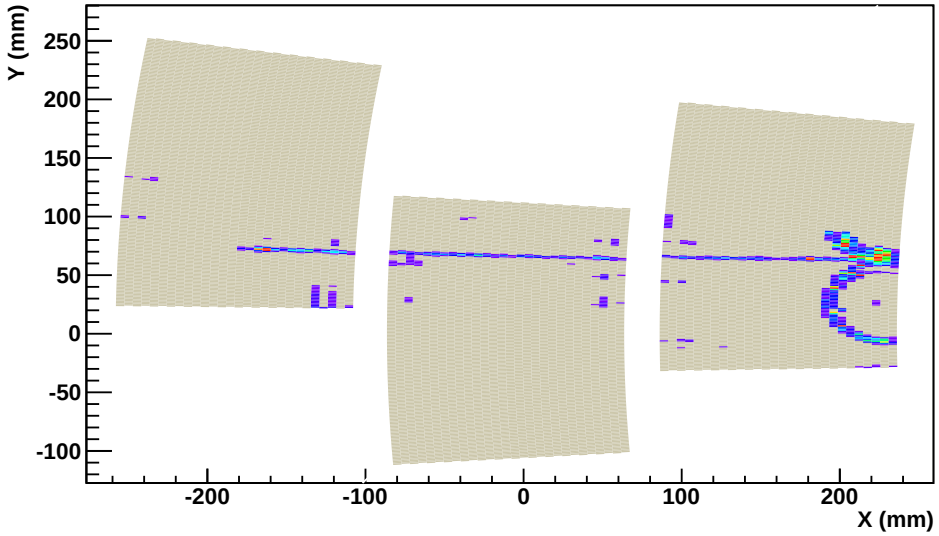

Figure 3.4: Electron track measured with the prototype TPC described in chapter 4. The track image shows a delta electron that follows a circular trajectory with a smaller radius than the main track.

to excitation of gas molecules and it can be shown that the energy lost in this way is large in substances with low ionization potential and vice versa [16]. Thus, W varies only weakly with gas type.

3.4 Drift

When a particle, here an electron, of charge e moves with velocity $\mathbf{v}$ in electric and magnetic fields ($\mathbf{E}$ and $\mathbf{B}$), it is subject to a Lorentz force

$$m\frac{d\mathbf{v}}{dt} = e\mathbf{E} + e\left(\mathbf{v} \times \mathbf{B}\right) \tag{3.8}$$

If the electric and magnetic fields are the fields applied over the TPC drift region, equation 3.8 is then the effect of the fields on the drifting electron. Since the chamber is filled with a gas mixture, the electron will suffer numerous collisions with the molecules of the gas. Because of this, the total force is modified with a term proportional to the drift velocity. The equation of motion thus becomes

$$m\frac{d\mathbf{v}}{dt} = e\mathbf{E} + e\left(\mathbf{v} \times \mathbf{B}\right) - \frac{m}{\tau}\mathbf{v}. \tag{3.9}$$

where m is the mass of the drifting particle and τ is the average time between collisions. This is known as the *Langevin equation* and is valid for times t much longer than τ.

Because of the repeated collisions, the electrons assume a constant average drift velocity, i.e. $\frac{d\mathbf{v}}{dt} = 0$. With this condition, the equation can be rewritten as

$$\mathbf{v} = \frac{e\frac{\tau}{m}E}{1+\omega^2\tau^2}\left(\hat{E} + \omega\tau\left[\hat{E}\times\hat{B}\right] + \omega^2\tau^2\left(\hat{E}\cdot\hat{B}\right)\hat{B}\right) \tag{3.10}$$

where $E = |\mathbf{E}|$, $\hat{E} = \mathbf{E}/E$ and B and $\hat{B}$ are the corresponding quantities for the magnetic field. Also introduced is the cyclotron frequency, ω, which is related to the magnetic field through $\omega = \frac{e}{m}B$ [17]. The $\mathbf{E}\times\mathbf{B}$-effects resulting from non-aligned fields are described by the middle term. This can be a problem, especially when the gas amplification is achieved with a wire solution. The electric field lines close to the wires will not be aligned with the magnetic field and distortions in the position measurements will result since the drift velocity will get a component perpendicular to the electric field.

It is clear from eq. 3.10 that with perfectly aligned electric and magnetic fields, the middle term vanishes and the drift would take place along the electric field direction. In this case, eq. 3.10 reduces to

$$\mathbf{v} = e\frac{\tau}{m}\mathbf{E}. \tag{3.11}$$

Thus, the drift velocity at a constant electric field depends on τ which in turn depends on the properties of the gas. For a certain gas mixture, τ, and therefore $\mathbf{v}$, depends on the energy of the drifting particle. There is therefore a maximum in the drift velocity at a certain amplitude of the electric field. The drift velocity can be obtained from simulations. From eq. 3.11 it becomes obvious that having aligned electric and magnetic fields is advantageous since the drifting electrons will follow straight paths from the ionization point to the readout structure, giving a good image of the track.

It is often desirable to operate at maximum drift velocity, among other reasons to minimize the event overlap. On the other hand, a high drift velocity gives a lower time resolution (for the same sampling frequency) so a compromise might be necessary. To avoid deviation of the electron trajectories the fields must be highly uniform.

For ions, the drift velocity is much lower than for electrons because of the larger mass. A large amount of ions are created in the amplification region and because of the low drift velocity, ions from several events will therefore be present in the TPC drift region simultaneously. This causes a large buildup of positive charge in the chamber which ultimately risks distorting the drift field and destroy measurement statistics due to drift electrons recombining with the ions. Some kind of gating is thus usually implemented to prevent the ions from drifting back into the drift volume and allow only registered particles to generate avalanches. This will be described below.

3.5 Gas properties

The gas mixture of a TPC is chosen with respect to the technical requirements of a specific experiment so that studies have to be conducted to find the best mixture for a specific application. Noble gases are often used for a number of reasons. One advantage is the negative electron affinity of noble gases which means that they will not trap the drifting electrons. Properties such as drift velocity, amplification and diffusion are important when choosing a gas. It should be such that the transverse diffusion is minimized because it degrades the position resolution. Also, longitudinal diffusion affects the drift time measurements. Another important property is that the drift velocity should be reasonably high even at a moderate field strength to limit central cathode voltage. As mentioned, a high drift velocity enables good discrimination between events since a short drift time lowers the risk of event overlap. When designing the chamber and its gas system, steps have to be taken to minimize gas impurities and leakage. Impurities introduced from sources such as out-gasing of chamber material or leakage, can be a

problem. For example, oxygen impurities (or some other electronegative gas) can lead to loss of primary statistics due to electron attachment [17]. If the impurities cannot be removed they have to be taken into account when analysing the experimental data. For momentum resolution, it is important to keep multiple scattering to a minimum since it degrades the resolution. Therefore, a gas with low Z of the gas molecules should be chosen. Again, however, a compromise might be necessary since a high Z will give a large number of ionization electrons.

3.5.1 Quencher

During avalanche formation, it is possible that a molecule deexcites by sending out a photon that has enough energy to ionize the material in the chamber walls or the cathode. This obviously has to be dealt with since it gives rise to signals that are not coming from the original track and cause further avalanches leading to a chain reaction. This is remedied by adding a quencher, a gas that has high absorption cross section for photons in the appropriate energy range. The absorbed energy is then dissipated by dissociation of the quencher molecules or through elastic colissions [15].

3.6 Diffusion

In a typical ionization event, the first electron produced by the incident particle (the primary electron) can ionise more gas molecules, if it has enough energy, and give rise to *secondary electrons* (not to be confused with delta electrons that can travel several millimeters). The electrons in the cloud resulting from this will drift towards the readout structure and form an image of the track . The size of such an electron cloud is initially treated as negligible so that all of the electrons have the same location before they start drifting towards the readout plane [18].

As they drift towards the anode, the electrons suffer numerous collisions with the gas molecules. The electrons are therefore scattered in multiple directions with the effect that the electron cloud diffuses outwards nearly isotropically. This diffusion of the cloud takes place in the drift direction as well as in the transverse plane, affecting the resolution in all space directions. In one dimension, say x, the electron will therefore deviate from its original position, x_0, by an amount Δx. The result is a gaussian distribution of electron positions around x_0 according to the probability distribution

$$P(x) = \left(\frac{1}{\sqrt{2\pi}\sigma}\right) exp\left(\frac{-(\Delta x - x_0)^2}{2\sigma^2}\right). \tag{3.12}$$

Here, $\sigma = D\sqrt{z}$ where D is the diffusion constant and z is the drift distance from the ionization point.

Since the resolution eventually gets worse with the diffusion it is to be expected that the drift distance will have an effect on the resolution. This has rather drastic consequences for the resolution where it rapidly gets worse with increasing z. Fortunately, a remedy for this is already a vital component in a tracking detector: the magnetic field. In addition to providing the track bending for momentum determination it also serves to reduce the transverse diffusion. A field oriented along the drift direction will cause a spiraling of the electrons along the drift direction, greatly reducing the effect of the diffusion. The result is that the diffusion constant is modified according to

$$D = \frac{1}{1 + \omega^2\tau^2} D_0 [17] \tag{3.13}$$

where D is the resulting diffusion constant, ω is once again the cyclotron frequency, τ is the average time between collisions and D_0 is the diffusion without magnetic field. Note that this only affects the transverse diffusion while leaving the longitudinal diffusion unaffected.

Diffusion is not necessarily a bad thing. Diffusion allows charge sharing between pads which is essential for a good reconstruction of coordinates, provided that the signal from the charge deposition is larger than the electronics noise. If the charge is shared between many pads it is possible to take advantage of this and achieve a better resolution than the one initially admitted by the pad size. Had the electron cloud hit only one pad the coordinates would have been given by the pad coordinates and had an uncertainty of the size of the pad. With the charge spread over a number of pads, a coordinate, can be determined by a mean of the pad positions weighted according to the charge deposited on the different pads. This is normally a gaussian distribution which means that the position of the peak value should correspond to the desired coordinate. The diffusion, used in this way, is therefore instrumental in achieving a high resolution. Indeed, if the drift distance is too short, the resolution should degrade due to low charge sharing between pads.

3.7 Amplification

It is often necessary to amplify a signal of few electrons to be able to measure it with an electronic readout system. In PM tubes, for example, the initial current produced by by an individual photon hitting a photocathode is amplified several orders of magnitude to produce a detectable signal. In a TPC, the electrons liberated in the primary ionization are around the order of 100/cm. If one tried to detect them directly, the signal would not be distinguishable from electronics noise. Electronic amplification is of course not useful at this stage since it would amplify the noise as well as the real signal. To remedy the situation it is necessary to somehow do the amplification before the electrons are collected on the readout plane. The solution is avalanche amplification in the gas, often called gas amplification.

Gas amplification works by subjecting the electrons to a strong electric field. This will accelerate the electrons to the point where they start liberating new electrons, here we will call them secondary electrons, from gas molecules. This leads to a so called Townsend avalanche where the newly liberated electrons are accelerated to ionize even more and so on. This leads to a great multiplication of electrons numbers, in the case of the Asian GEM system studied in this thesis, the gain is of the order of 10^4. The field strength is chosen such that the mean amount of avalanche electrons is proportional to the number of incoming drift electrons. In this mode of operation, called proportional mode, it is possible to relate the charge collected after the amplification to the energy loss of the traversing particle.

3.7.1 Wire Readout

Electric fields strong enough for avalanche amplification can be obtained in different ways. Originally for TPCs, the amplification was accomplished using the same principle as in proportional counters. A plane of sense wires, much like one found in a Multi Wire Proportional Chamber (MWPC), is located above the pads on the readout plane where they are kept at a high positive potential. With thin sense wires one gets a high electric field in the vicinity of the wires since the field strength goes as $1/r$, where r is the distance to the wire center. When the electrons are sufficiently close to the wire, the field will be strong enough to start an avalanche. The ions created in the avalanche induce a signal in the pads as they drift towards the cathode.

There are some limitations with the wire method. The resolution is limited by the fact that the wires need to be kept at a minimal distance of a few millimeters of each other to limit the strain on the wires. It also suffers from $\mathbf{E} \times \mathbf{B}$-effects close to the wires which limits the attainable resolution. It has been shown that the $\mathbf{E} \times \mathbf{B}$-effects using wires are to severe for the TPC envisioned for the ILC [19]. The signal is mainly due to the ions from the avalanche drifting away from the wire which is a slow process compared to the amplification. For a high rate capability it would be advantageous to produce the signal directly from the secondary electrons since they drift faster. The wires need to be kept at a high tension to provide a parallell alignment. This introduces the need for a stiff support structure that increases the

material budget.

Ion backdrift

Many ionization events occur in the amplification region of a TPC, which means that a large number of positive ions are created here. The ions will drift towards the cathode, creating the charge buildup mentioned above.

To minimize the amount of backdrifting ions and prevent electrons that are not track related (or comes from unwanted cosmic radiation and collisions not giving a trigger signal) from starting avalanches, at least those that are not close in time to a real track, an ion gate (or gating grid) can be used. This is a device that makes it possible to prevent movement of electrons and ions between the drift region and amplification region, thus preventing backdrift and at the same time limiting unnecessary ion production.

A gating grid is made up of wires that are placed in front of the amplification region and can be used to manipulate the electric field. To prevent ions and electrons to pass the gate, the wire potentials are set in such a way that the field is perpendicular to the drift direction. Thus, the ions and electrons are swept away when the grid is closed. When a trigger signal comes the potential of the wires is set to the potential corresponding to their location in the drift field. Thus, the gate wires will leave the field unaffected and the electrons can pass through to the amplification region.

For the event rate at the ILC, a gating grid can not be used because of the short time between bunch crossings. Another solution is therefore necessary.

3.8 Micro pattern gas detectors

To meet the physics goals at the ILC, two improved amplification techniques are under consideration for the ILD TPC: Micromegas and GEMs.

3.8.1 Micromegas

Micromegas (Micro-Mesh Gaseous Detector) consist a of thin wire mesh placed above a pad plane. Gas amplification is achieved by applying a potential between the mesh and the pad plane. Electrons passing the mesh will be accelerated to create an avalanche just as in the sense wire approach. The secondary electrons are then collected on the pads where they create a signal. The work in this thesis is dealing with a GEM based TPC and therefore, micromegas will not be considered further.

3.8.2 GEM

The Gas Electron Multiplier (GEM) was introduced in 1996 [20] by the Gas Detector Development Group at CERN. A GEM is made of two foils of a conducting material (often copper) separated by an insulator. It is highly perforated by holes with diameter of about 70 micrometers, with a hole density around $50 - 100/\text{mm}^2$. The pitch of the holes is around a 140 μm which is about the same size as the resolution goal of the ILD. Fig. 3.5a shows an electron microscope image of a GEM. By keeping the two metal layers at a suitable potential difference of a few hundred volts between each other the structure can be used for gas amplification. A single GEM can provide a gain of about 10^2, depending on the voltage applied between the copper foils and the gas mixture used. The GEM is placed in front of the pad plane so that the drifting electrons are collected in the holes of the GEM where the large potential

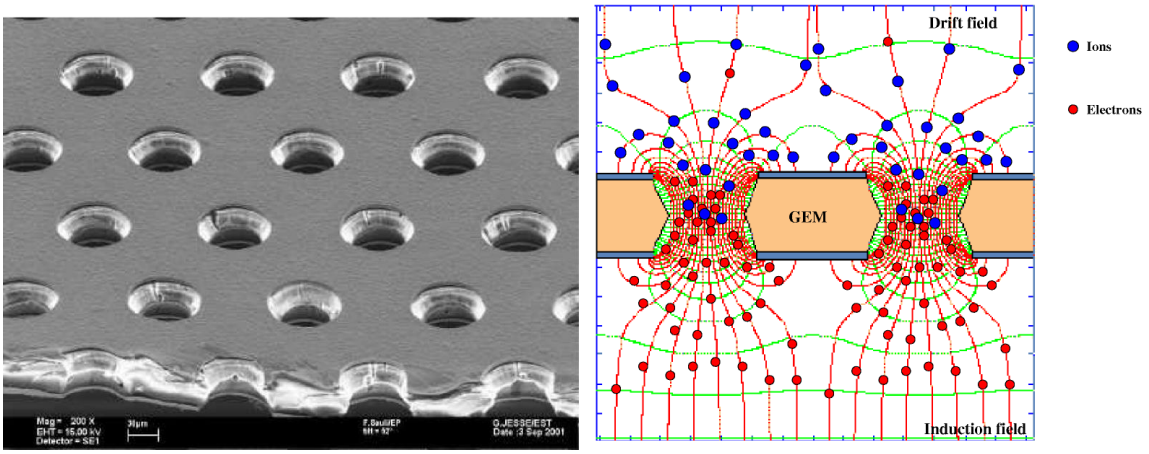

(a) (b)

Figure 3.5: (a):Electron microscope image of a GEM-foil [21]. (b):Sketch of the field lines and principle of a GEM [21].

difference accelerates the electrons and an avalanche is formed in a similar way as described above for the wires. Normally, several GEMs are be placed in front of each other to greatly increase the avalanche gain since the gain of e.g. a double GEM structure should be close to the product of the individual gains. This can also be used to allow a reduction in the gain for the individual GEMs which leads to less risk of a discharge. After amplification the charge is collected directly on the pads. In this way, the ions are not involved in producing the signal which avoids the problem of limited time resolution due to the slow drift of the ions.

A large advantage of the GEM is the almost complete lack of $\mathbf{E} \times \mathbf{B}$ effects. Another advantage of GEMs is that they can provide their own backdrift suppression with the proper configuration of the electric fields. If the field in front of the GEM is lower than behind the GEM, most of the field lines going through the hole ends on the upper surface (the surface closest to the drift region). Thus, the ions will be swept onto the upper foil as they drift out of the hole. The electrons on the other hand will leave the GEM and continue in the pad direction since the higher field means that only a few field lines end on the lower surface. The GEMs also relaxes the demands on the support structure, whereas anode wires need to be held at a high tension. This minimizes effects on traversing particles due to thick chamber walls. In a wire chamber, the pads have to be of the same order in size as the distance between the wires not to distort the field to much. Here they can be made a lot smaller and the GEM holes also has a smaller pitch than traditional wires.

Chapter 4

Experimental setup and The Large TPC prototype

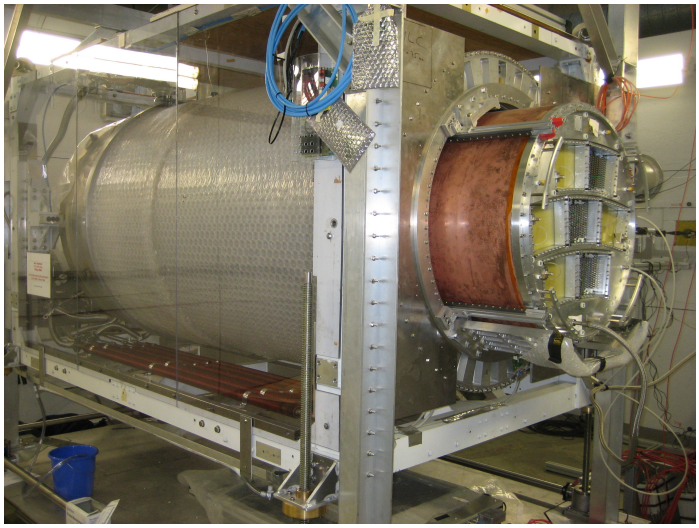

Figure 4.1: The Large TPC Prototype partially inside the magnet, before connecting the electronics.

The TPC studied in this thesis is constructed by the LCTPC (Linear Collider TPC) collaboration. It has been used to test different readout structures in a testbeam area at DESY (Deutsches Elektronen Synchrotron) in Hamburg since the end of 2008. The beam can deliver electrons of momentum up to 7 GeV/c. A superconducting magnet, PCMAG, provides a nominal field of up to 1.2T. The chamber itself consists of two major components which are the field cage and the endplate. They will be described in this chapter along with the readout system and the experimental setup at the testbeam.

4.1 Test beam

The tests were performed at the test beam area 24 at DESY. The DESY II electron synchrotron delivers a photon beam by guiding the circulating electrons towards a carbon fibre inside the vacuum tube. The photons are produced through bremsstrahlung and the energy spectrum follows a 1/E dependence. The photons hit an external metal sheet to produce electrons and positrons in a pair production process.

By passing the resulting beam through a dipole magnet it is spread out and then passed through a collimator. The nominal electron energy can be selected by the setting of the magnet and the energy spread is given by the size of the collimator.

4.2 The field cage

In order to have a homogeneous field, the chamber is equipped with a field cage. It consists of conducting strips placed along the inside of the chamber wall. Connected through a chain of resistors they lie on a decreasing potential ladder from anode to cathode. A second layer, called the mirror strips, covers the gaps between the strips of the first layer and lie on a potential between the neighbouring strips (connected through the foil). Together with the first layer it serves to shield the chamber from external fields and make the field near the wall even more homoegeneous. A homogeneous drift field is important for a uniform drift velocity. For example, a varying drift velocity might lower the resolution in the drift direction.

For the final TPC, a number of considerations are important when it comes to the field cage. To limit the effects of electric field inhomogeneities on the spatial resolution, the goal is to keep such inhomogeneities below 10^{-4} which in turn requires a mechanical accuracy of the field cage of about 100 μm. In order to minimize scattering of the particles and conversion of photons in the inner wall of the TPC, i.e. between the TPC and the vertex detector, a low material budget is necessary. At the same time the chamber has to be able to withstand a certain gas pressure without deforming. An overpressure of up to 10 mbar needs to be possible without deformations larger than 100 μm. In the Large Prototype, the material budget was required to be close to 1% X_0 (the radiation length of the material) which is also the requirement for the ILD TPC. The high drift field of hundreds of V/cm means that high voltages need to be applied to the cathode without causing breakdown to ground.

The field cage was designed considering the dimensions of PCMAG and the homogeneity of the magnetic field. The field is only sufficiently homogeneous in the middle of the magnet (where the variations are $< 3\%$) which was considered for the length of the TPC (61 cm). The diameter was decided at 77 cm, with an inner diameter of 72 cm, to allow for a 4 cm gap between the field cage and the magnet (PCMAG has an inner diameter of 86 cm) where a silicon strip detector would be mounted to define the impact position of the electrons. The silicon detector was however not ready to be mounted during any of the data taking described in this thesis.

The outermost layer of the field cage barrel provides electrical shielding and consists of a 10 μm grounded copper foil on a 50μm polyimide layer.

The supporting walls of the field cage are made out of an aramid honeycomb structure sandwiched between two layers of glass-fiber reinforced plastic (GRP) and an insulating polyimide layer. The polyimide layer is 125 μm thick which has proved to be more than enough to prevent breakdowns at long term usage at 20 kV [22]. The thickness of the GRP layers were minimized to achieve a low material budget and tests were performed to make sure that the goals for high voltage stability and resistance against deformation were met. It was shown that the overpressure has to be kept below 400 mbar to limit wall deflection to 100 μm. The goal of 10 mbar overpressure is thus well below this limit.

To shape the field and give it a high level of homogeneity, 210 copper rings, or field strips, cover both sides of a kapton sheet which is glued to the inside of the barrel. They are connected through a chain of 1MΩ resistors which place them on a potential ladder from anode to cathode where the anode is held at ground potential and the cathode at a large negative potential (<-14kV). Calculations show that the expected resistance deviations, less than 0.1%, give deviations no larger than the design requirements[23]. The pitch of the strips is 2.8 mm. To keep the deviations $\Delta E/E$ of the drift field below 10^{-4} and prevent the field outside the strip foil to penetrate into the drift region near the chamber walls, a design with mirror strips on the intermediate potentials between the field strips was chosen. They are displaced by

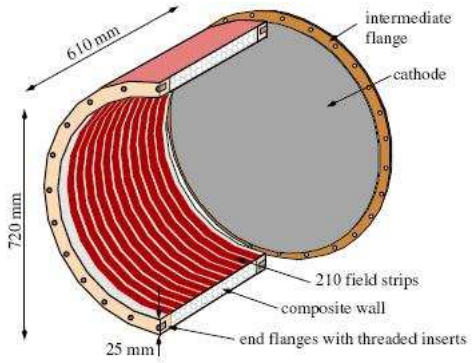

Figure 4.2: Sketch of the field cage [24].

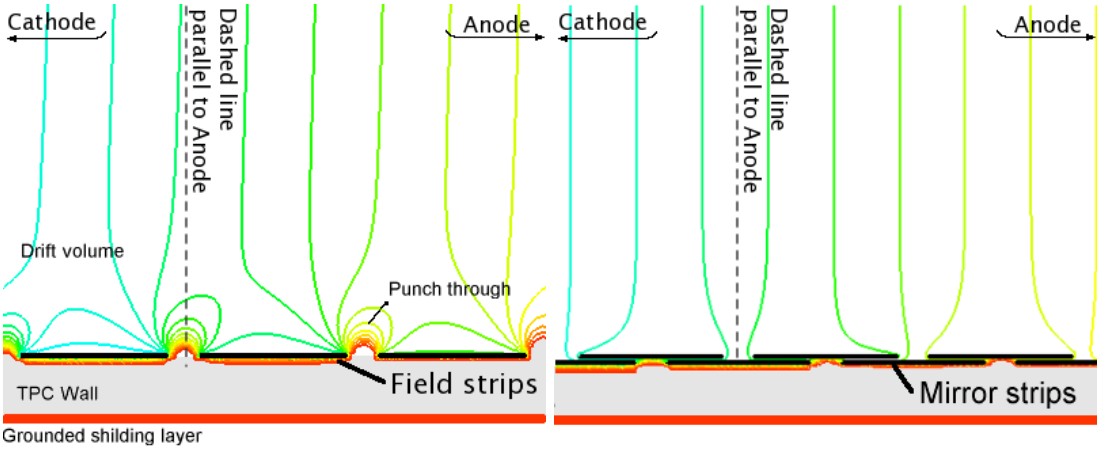

Figure 4.3: Equipotential lines of the drift field close to the chamber walls. The effect of the external field is called "punch through". As can be seen in the right figure, the situation is significantly improved by the inclusion of mirror strips. [25]

half the pitch of the field strips, thus covering the gap of 0.5mm between the field strips. Fig. 4.3 shows the effect of the mirror strips.

The cathode is a circular copper disk supported by a G10 (glass-epoxy laminate) endplate. It is mounted at the other end of the field cage from the readout plane. The high voltage is supplied to the cathode which in turn is connected to the first field strip and thus the entire chain of strips is connected.

4.3 End Plate And Pad layout

The end plate is made from aluminium and has an outer diameter of 77 cm. It contains seven slots where readout modules can be placed. The readout plane of the LP TPC is designed to represent a small section of the ILD TPC. In the ILD TPC, the modules will be organized in circles around the beam axis, where every module will be shaped as a keystone circle segment with origin on the chamber axis. This means that the modules will have a slightly different shape between the circles. For simplicity, the modules of the Large Prototype have the same shape and are constructed as segments of a circle with the first module row at 1440.01mm from the origin (Fig. 4.6). The modules are exchangeable so that the same end plate can be used to test both Micromegas and GEMs. In addition, some of the slots can be fitted with dummy modules if one does not wish to instrument the entire end plate. Fig. 4.4 shows a sketch of the proposed ILD endplate and fig. 4.5 shows the design of the end plate for the Large

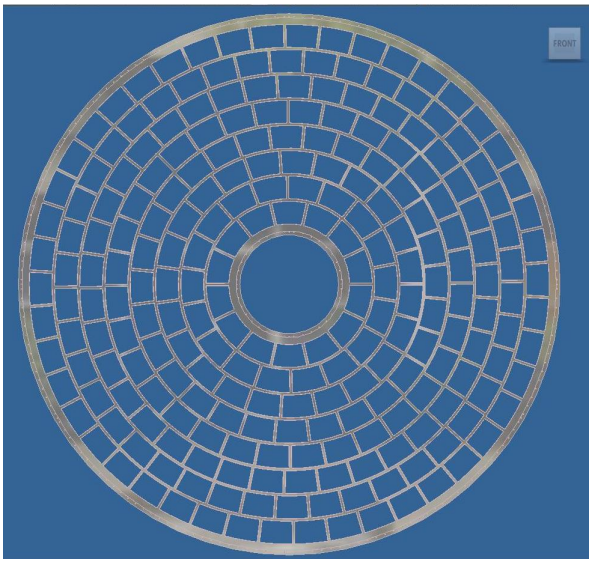

Figure 4.4: Sketch of the proposed design for an end plate in the ILD TPC.[26]

Prototype.

The pad modules used contain 5152 pads, organized in 28 rows. Of these rows, the 14 in the upper half contain 192 pads and the other 14 contain 176 pads with a gap of 0.10mm between the pads. All pads have a height of 5.26mm and a width of about 1.1mm that varies slightly between rows since the module does not have a rectangular layout. Between the rows, the pads are staggered by half the pad width to minimize the so called hodoscope effect which occurs when the drift length is short so that the diffusion no longer provides enough charge sharing between the pads, resulting in a resolution that is on the order of the pad size. Fig. 4.7 shows a sketch of the pad layout.

On the module outside, connectors are mounted that provide an interface between the pads and the electronics. The pads are organized in units of 32 that share one connector. The connectors are supplied by the JAE [27] and has 40 connections of which eight are used for grounding which leaves the 32 mentioned to be used for readout. The correspondence between connector and region of the pad plane is shown in figures 4.8 and 4.9.

Only a subset of the pads were instrumented during the experiments. The pads are connected to Front End Cards (FECs), which contains the readout electronics, via kapton cables. The current number of available Front End Cards is 80 whichs allows for a maximum of 10240 channels to be instrumented. This is sufficient for the purposes of the measurement since the direction and impact position of the electron beam is well known and the pads can be instrumented in such a way that they cover the interesting region, i.e. the part where the electron beam is aimed. A more detailed description of the instrumented regions is provided below.

4.3.1 GEM Modules

A number of GEM modules have been built by the Asian TPC group. The GEM foils, manufactured by SiEnergy, consist of 5 μm thick copper layers separated by a 100 μm thick liquid crystal polymer insulator [27]. The holes are 70 μm in diameter and have a pitch of 140 μm. Due to a different etching procedure than the chemical etching used for the modules manufactured at CERN, the holes are cylindrical rather than biconical which is the case for the CERN GEMs. The pad boards, manufactured by Tsinghua University [29], are etched onto a multi-layer printed circuit (PC) board.

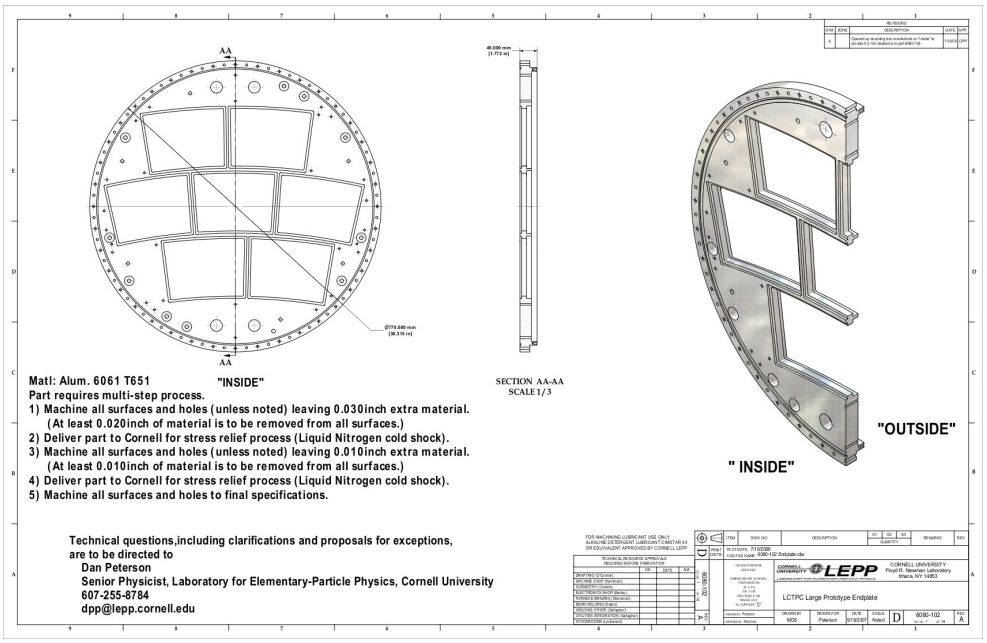

Figure 4.5: The design of the LP end plate.[26]

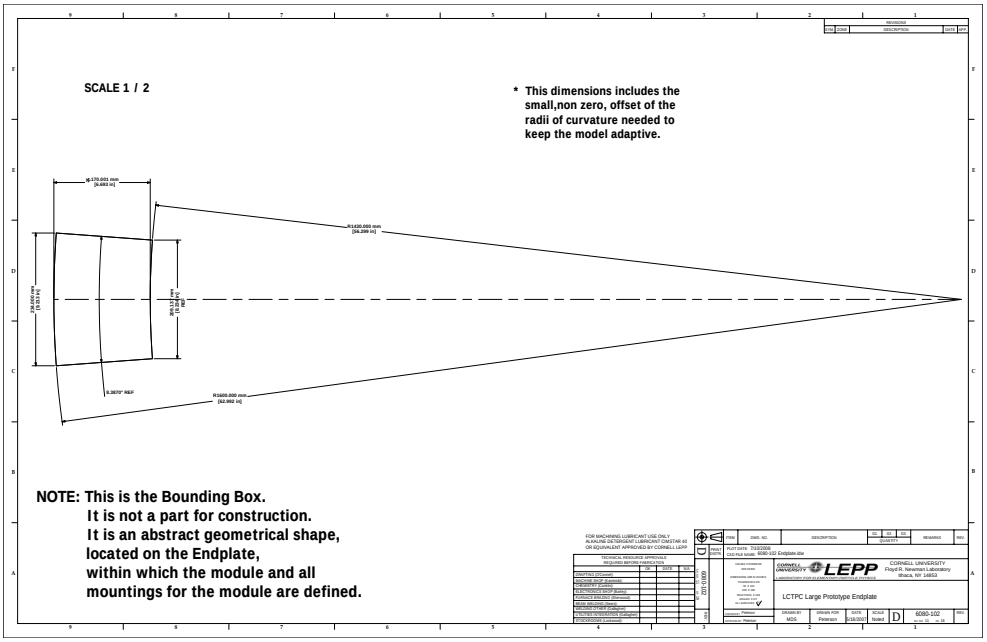

Figure 4.6: The slots in the endplate, and therefore also the module shapes, are defined as part of a circle segment.[26]

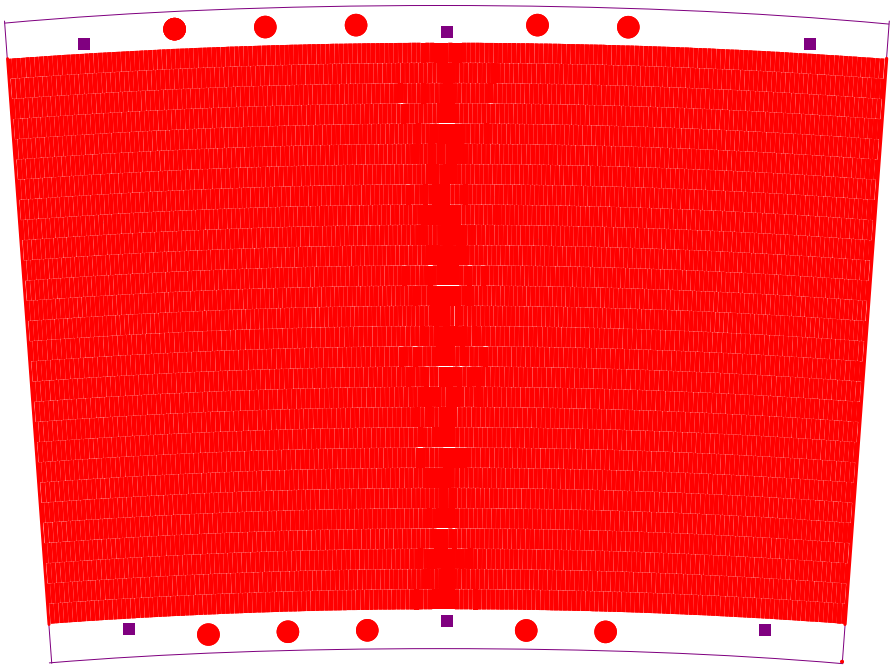

Figure 4.7: Sketch of the pad plane. The rows of the bottom half contain 176 pads while the top half contain 192 pads per row. The widhts are slightly varying from row to row to account for the fact that the module is arc shaped, keeping the gaps between the pads constant at 0.10mm. The location of the support pillars are indicated by squares at the top and bottom of the module. The circles indicate locations of the high voltage lines for the GEMs.

The GEM foils are glued with epoxy adhesive to a set of G10 frames in order to stretch them and allow mounting over the PC board. To minimize dead areas between the detector modules, only the long sides of the GEM foils are attached to frames. Two GEMs are mounted over the pad plane, which may provide a total avalanche gain of about 10^4 [27]. This is quite high and is possible because the 100 μm of insulator allows stable operation with higher gain from a single module than the usual 50 μm. For these measurements, the GEM foils were biased with a voltage of 360V which gives a gas gain of about 3,000 [28]. In the experiment described in this thesis, a gating GEM structure was planned but not mounted. Because of this, the support structure of the gating GEMs was exposed to the drift region. This created a distortion in the electric field close to these support pillars, where the field was no longer parallell to the drift axis of the chamber. To correct for this, a field shaper, covering the support pillars, was designed to set the voltage of the field shaper to the appropriate value corresponding to its location (at the 7th field strip counting from the anode). The field shaper was installed during the measurements in September 2010. This did not remove the distortions however, due to a miscalculation of the required voltage, such that the voltage of the field shaper was wrong by 30V.

The thickness of the G10 frames decide the spacings in the GEM stack. This gives a transfer gap (i.e. the gap between the two foils) of 4mm and an induction gap (the gap between the last GEM foil and the pad plane) of 2mm. The electric field in both gaps is set to 900V/cm.

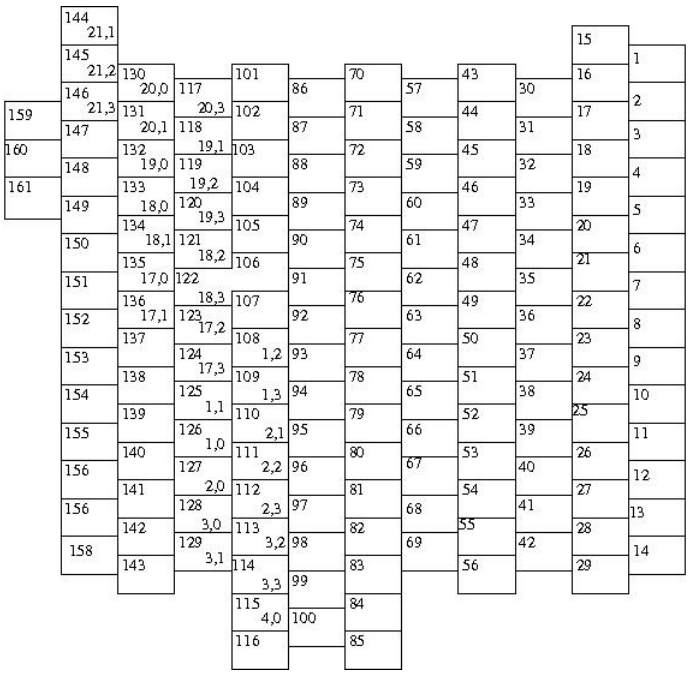

Figure 4.8: Layout of the connectors on the module backside.

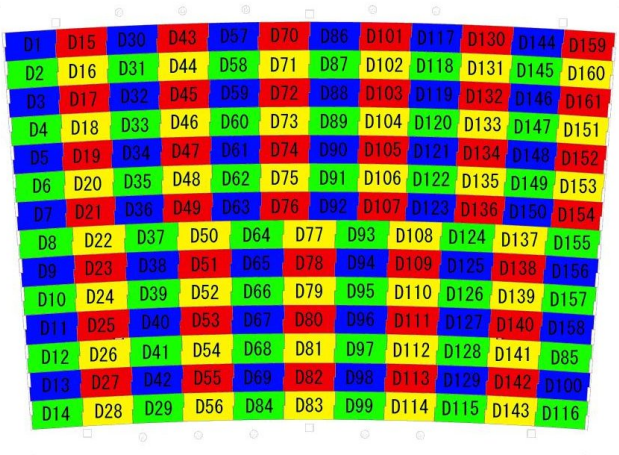

Figure 4.9: Schematic view of a pad plane. The regions corresponding to different connectors are indicated.

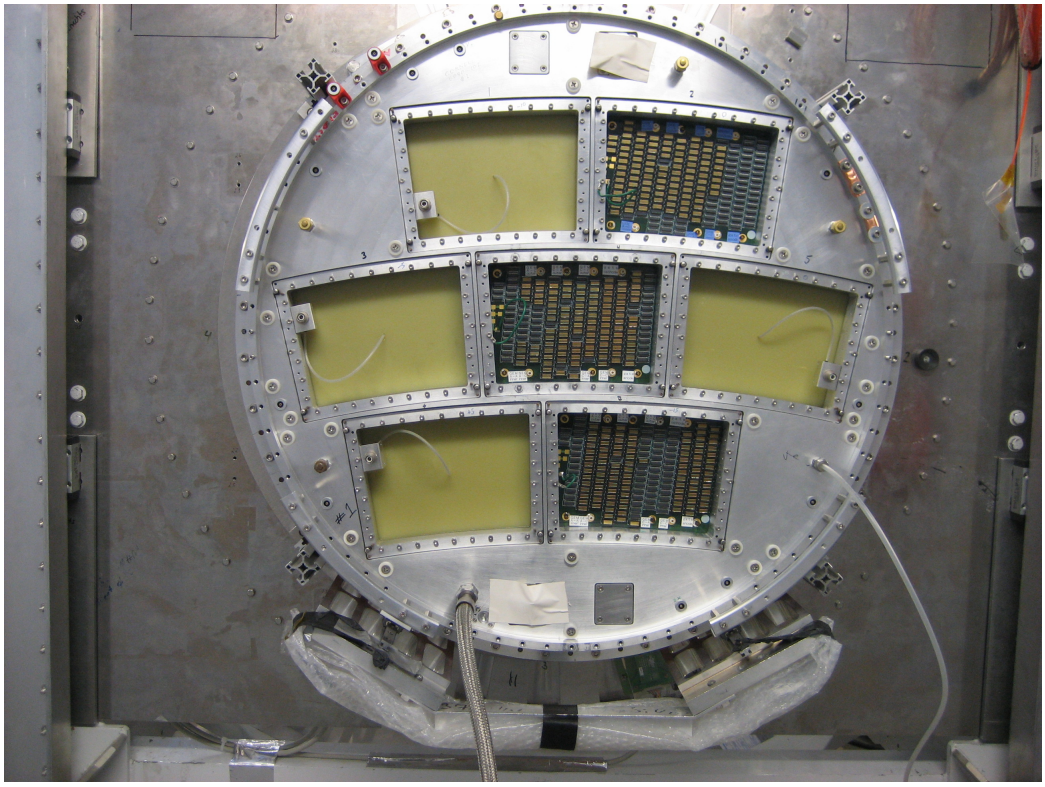

Figure 4.10: The end plate seen from the outside. Only the positions 0, 3 and 5 are equipped with pad modules.

4.4 HV-system

The high voltage to the cathode is provided by FUG Elektronik HV power supplies. It is capable of delivering voltages of up to 20 kV. For the HV of the GEMs and dummy modules, a CAEN based system is used. The electrodes of the dummy modules and the field shaper designed to compensate for the distortions created by the support structure of the missing gating GEMs are at the same position (in the drift direction) as the 7th strip of the field cage. The field cage has two HV inputs, one at the cathode and one at the 7th field strip, and by connecting the 7th strip, the dummy modules and the field shaper to the same output, they can be kept at the same potential. This is important since the GEM electrode (or the dummy modules and field shaper in this case) facing the drift region has to be on the same potential as the corresponding strip in order not to distort the drift field. Due to the miscalculation however, a distortion was present. The GEM foils themselves are connected to a separate HV-source which includes a protection mechanism in case of a discharge. To do this, the system monitors the current and switches of the voltage if a threshold current on the order of μA is exceeded for a few seconds.

4.5 Magnet and support structure

A superconducting solenoid magnet, PCMAG (permanent current magnet), has been placed in the test beam line and is used to provide the magnetic field for the TPC. It was originally built within the Japanese-American Collaborative Emulsion Experiment. There, it was used for cosmic ray experiments in balloon flights over the Antarctica. The magnet has a cylindrical bore with a radius of 86 cm, where the LP is placed during test runs. The maximum current is 520 A which corresponds to a magnetic field of about 1.2 T. During these measurements, the field was set to 1T. Liquid He is used to cool the magnet

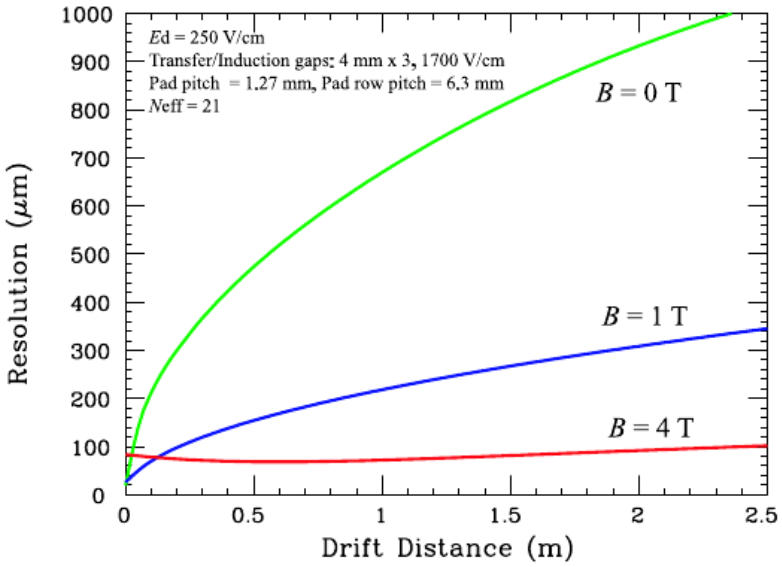

Figure 4.11: Calculated resolution for a GEM TPC in different strengths of the magnetic field using T2K gas and a pad pitch of 1.27mm. [19]

down to its operating temperature.

Inside the magnet, rails are mounted which makes it easy to slide the TPC back and forth. It is also possible to rotate the TPC in order to get the desired angle of the beam with respect to the pad plane.

The design of PCMAG gives a high homogeneity in the center of the solenoid, which is where the TPC is placed during data taking. Here, the field should be homogeneous to within 3% accuracy. The higher field gradients at the ends of the coil introduces the need to be able to move the magnet itself if one wants to measure at different drift lengths. The magnet is placed on a movable table which allows movement of the entire setup with respect to the beam. In the first runs described in this thesis however, the table was not yet installed so the TPC was moved inside the magnet in order to have the beam at different distances to the pad plane. This meant that only drift lengths of up to 30 cm was available if the TPC was to be kept inside the homogeneous region of the magnetic field. In the later runs, the movable table was installed and so the TPC could be kept at the same position inside the magnet which gave access to longer drift lengths.

4.6 Gas

The gas mixture of the TPC, hereafter referred to as the T2K gas since it was used in a TPC at the T2K experiment in Japan [30], is a mixture of 95 % Ar, 3 % CF_4 and 2 % isobutane. Its properties have been investigated in both analytical calculations and measurements, e.g. in [19] and [31]. The T2K gas exhibits a low diffusion and should be well suited for achieving the resolution goal, especially at the high magnetic field envisioned for the ILD detector. Simulations have been done in [19], showing that a drift field of 250 V/cm is advantageous because it maximizes the drift velocity while also minimizing the diffusion. Fig. 4.11 shows the expected resolution for different field strengths.

For the used drift field of 230 V/m, the diffusion constant C_D of $93.7 \pm 2.4 \mu\text{m}/\text{cm}^{1/2}$ was measured [31]

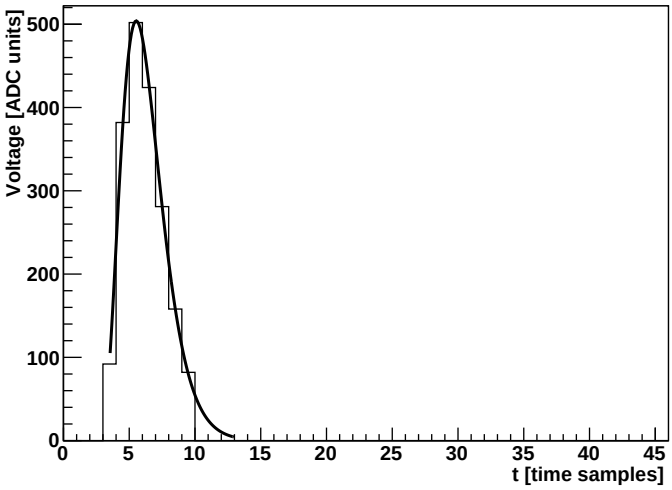

Figure 4.12: Fitting of a digitized pulse using the Γ_4-function $A\left(\frac{t-t_0}{\tau}\right)^4 \exp\frac{-4(t-t_0)}{\tau}$ with the parameters $A = 27517.5, t_0 = 2.4578$ and $\tau = 3.07499$ resulting from the fit.

which agrees well with simulations [19].

The properties of the gas vary with environmental conditions such as temperature, pressure and oxygen content. These properties were therefore logged for each run.

4.7 Data acquisition electronics

The electronics for the experiment is based on the readout system used in the ALICE experiment at the LHC. Each connector is connected to a FEC through a kapton cable. Each FEC can be connected to four connectors which means that 128 readout channels can be handled by a single card. The FECs are placed in an electronics crate (Fig. 4.7) designed for the experiment. The circular crate is attached to the end plate of the TPC and rests on the rails that are used to support and push the TPC into the magnet. A grounded copper screen is placed between the electronics and the end plate to shield the cables from noise from the electronics and elsewhere.

The signals are amplified using a 16-channel charge sensitive amplifier called PCA16. It is a version of the Pre-Amplifier Shaping Amplifier chip (PASA) used in the Alice TPC, modified to allow a programmable gain. The gain can be set in four steps between 12 to 27 mV/fC. It also contains a shaper function with programmable peaking times between 30 and 120 ns. The response function of the amplifier is very well approximated by a Γ_4-function as shown in fig. 4.12 [32].

The amplified signal is digitized by an ALTRO chip (Alice TPC ReadOut) originally developed for the ALICE TPC at the LHC. It has a sampling rate of up to 20 MHz (there are also a number of chips capable of providing 40 MHz). An onboard memory is capable of storing 1024 10bit ADC samples of an event which corresponds to 50 μs at 20 MHz sampling rate. This is quite enough since a drift velocity of about 7.6 $cm/\mu s$, gives a drift time of about $6.5\mu s$ for the longest drift distance (500mm). The ALTRO is also capable of pedestal subtraction and suppression of zero data which reduces the demands on data transfer and storage capabilities. The pedestal values are aqcuired by performing runs with the beam shutter closed and using a pulse generator for triggering. The pedestals are then loaded into the ALTROs. Zero suppression is done on the pedestal subtracted signals. A pulse passes the zero suppression when two consecutive samples are above the programmable threshold. These two and all samples above the

threshold that follow them are considered to belong to the same pulse. In addition, the three samples preceding the pulse and the seven after the pulse falls below the threshold again, are included in the pulse. Generally, it is a good idea to set the threshold to a value of a few times the RMS of the pedestal. Since not all of the 1024 samples are saved, time information needs to be saved along with the pulse. This is taken as the timestamp of the last sample included in the pulse [33]. All in all, each FEC contains 8 PCA16s and 8 ALTROs, giving the mentioned 128 channels per FEC.

The FECs are controlled from a Readout Control Unit (RCU). One RCU can control 32 FECs via a data bus (a backplane) connected to the back of the FECs. The number of RCUs needed depends on the number of FECs and how they are arranged in the crate. With the current arrangement a maximum of three RCUs can be used. A readout sequence starts with the RCU receiving a trigger indicating that a particle has entered the chamber. Triggering is provided by four scintillators situated between the TPC and the beam aperture as depicted in fig. 4.13. The RCU then tells the ALTROs to start digitizing the analogue signals from the PCA16 chips. Data passing the zero suppression is then collected from the ALTRO memory and sent to a PCI-card (DRORC, Detector ReadOut Receiver Card) in a computer and then further on to the DAQ software which has been written specifically for the Large Prototype [34]. It is using the ALICE drivers and libraries with a readout system built on top. It performs the setup (e.g. configuration of the PCA16 and ALTRO chips), readout and data storage. Run control is provided in a JAVA-based graphical user interface (GUI) where options such as gain and shaping time for the PCA16s can be set. Other options include the possibility to turn data logging on and off and a choice between doing a pedestal run, where the run is done without beam to measure the pedestal of the readout channels, and a physics run with beam with the measured pedestals uploaded to the ALTROs. For online event monitoring a ROOT-based event display is implemented. Also included is a temperature monitoring system to make sure that the temperature of the electronics does not rise to dangerous levels.

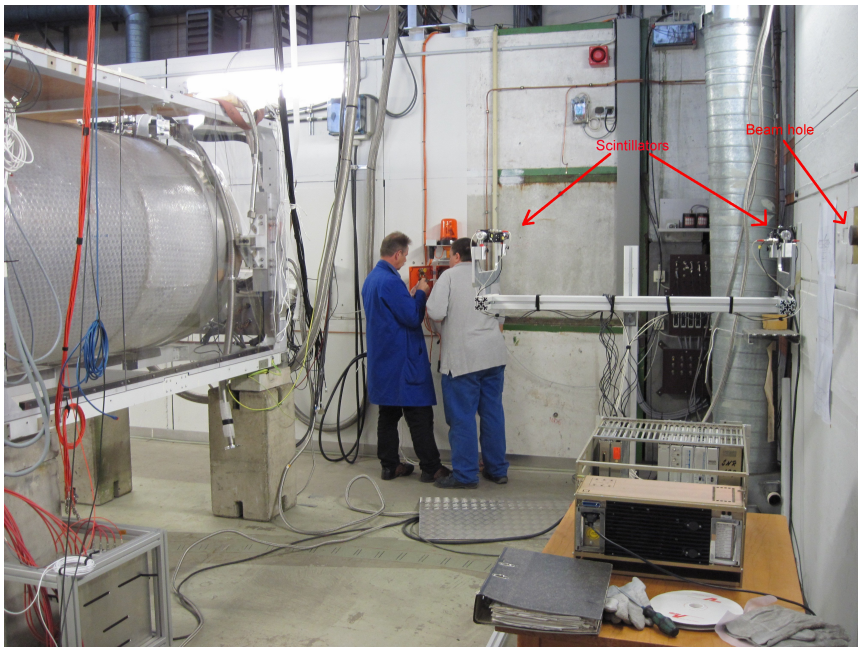

Figure 4.13: Four scintillators are used in coincidence to provide the trigger of an incoming electron. A measurement is started when all four scintillators fire simultaneously. The setup with four scintillators grouped two by two with a 100cm gap in between ensures that the a particle producing a trigger has to travel in the beam direction which minimizes the risk of an accidental triggering by e.g. a cosmic muon. By placing a delay between the two pairs it is also possible to get an estimation on the number of accidental coincidences.[38]

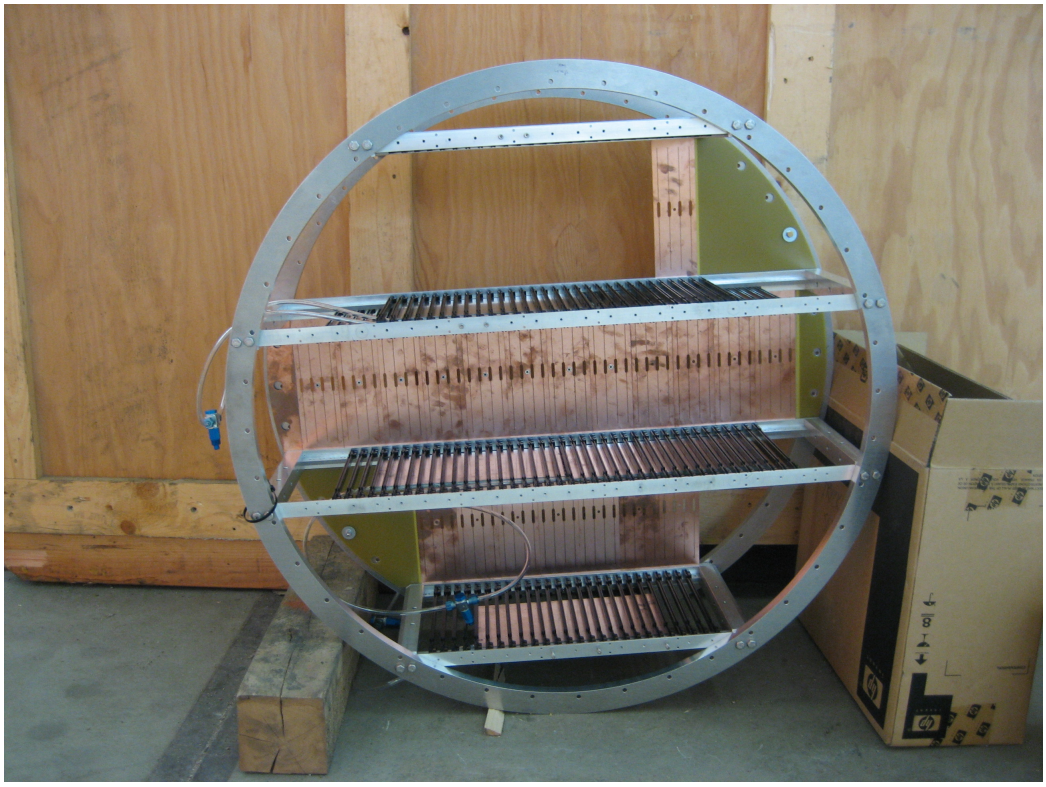

Figure 4.14: The electronics crate.

4.8 Cooling

During operation, the temperature in the electronics rises quickly. A cooling system is therefore required to keep the temperature on a level that will not damage the circuits. Originally, a large fan connected to aluminium tubes was used. To minimize the size of the cooling system, a new design was used in this experiment. Copper tubes with drilled holes connected to a compressor were placed in between the FEC levels on the crate. This air cooling system was significantly smaller than the fan solution. To monitor the temperature, sensors were placed on the voltage regulator chips on every fourth FEC. Measurements indicated that the temperature rose to a certain value, depending on its position in the electronics crate, where it remained constant. Measurements are not done before it is constant since the pedestals drift with temperature.

The temperature monitoring system gives a warning when the temperature of any regulator rises above 50 degrees Celcius. When it goes above 60 degrees, the system is shut down to protect the equipment. The electronics should however be able to handle larger temperatures but this setting gives some safety margin. Fig. 4.15 shows the temperature of four FECs during a day. It is clear that the temperature stabilizes at well below 60 degrees during operation.

4.9 Coordinate system and instrumented region of the pad plane

In Fig. 4.17, a visualization of the pad plane, seen from a position outside the TPC facing the endplate. In this case, with data from the measurements in September 2010, three modules were used. The black regions of the modules indicate instrumented pads, whereas the gray area shows the pads without instrumentation. The instrumented pads were chosen in this way to be able to measure tracks over the

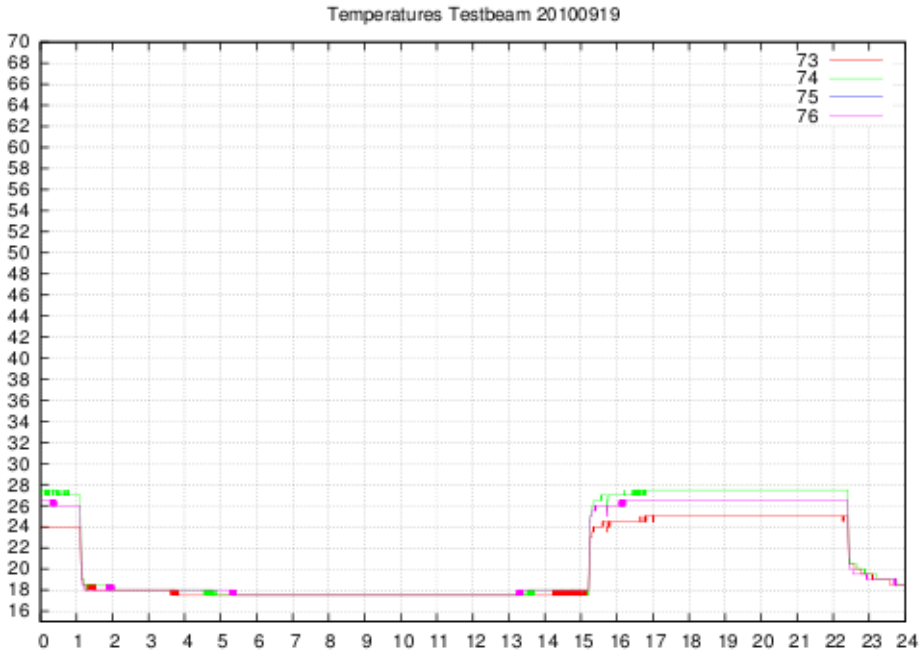

Figure 4.15: The temperature monitored on the voltage regulators of four FECs during one day. The vertical axis shows the temperature in °C while the horizontal shows time in hours. When the system is running, the temperature rises to about 28 degrees where it remains constant.[38]

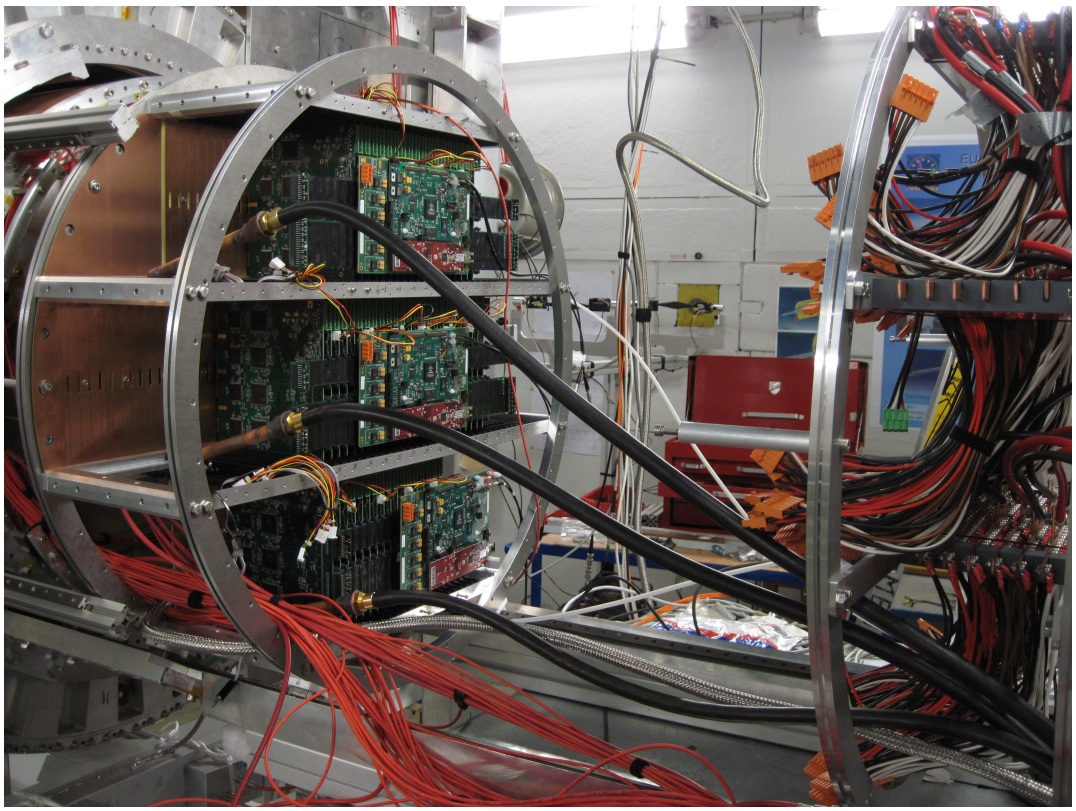

Figure 4.16: Cooling is provided by a system copper tubes with drilled holes, placed in between the FEC levels in the crate. These are connected to a compressor by the three hoses seen here.

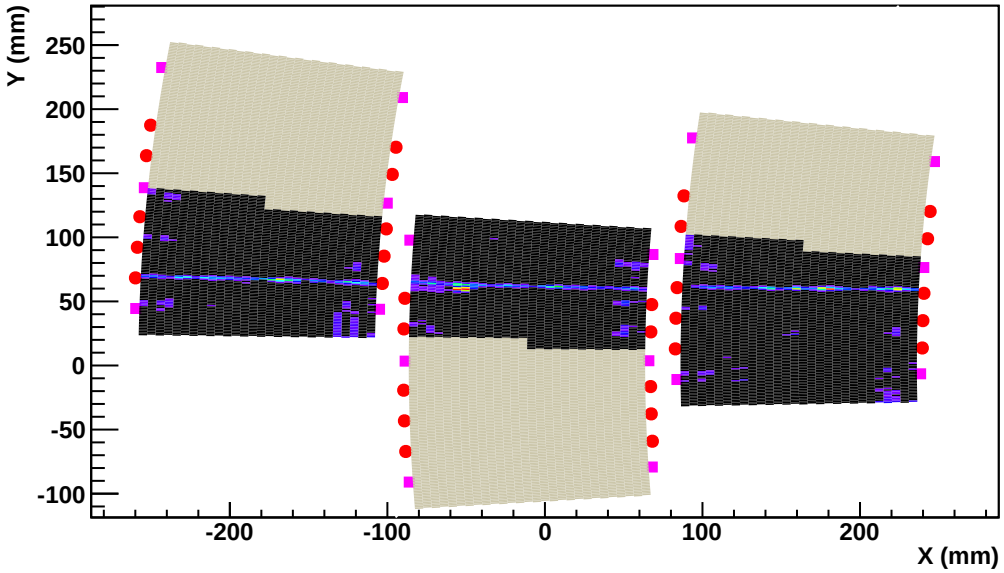

Figure 4.17: The pad modules used in September 2010 seen from the outside of the TPC, with the beam coming in from the right side. The instrumented region can be seen here (in black), as well as a typical event. The squares and circles on the long module edges represent the support pillars of the gating GEM and the high voltage lines of the GEMs respectively.

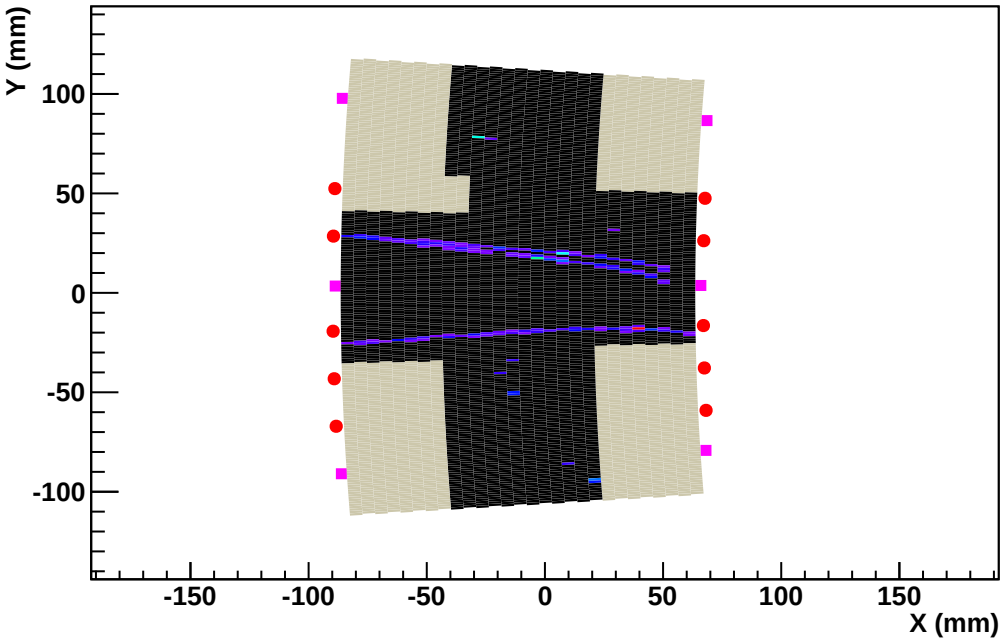

Figure 4.18: In July 2009, only the middle module was used, instrumented as indicated by the black region.

full radial length of the TPC. The support pillars of the gating GEM are indicated by the squares on the module edges. The circles represent the high voltage lines for the GEMs. A typical event is also drawn, where the track can be seen in all three modules with the beam entering from the right side. In

Fig. 4.18, the corresponding figure is shown for the measurements of July 2009 with only one module being instrumented.

The coordinate system is defined with the origin in the middle of the pad plane, as indicated in Fig. 4.17 and Fig. 4.18. The z-direction is parallell to the drift direction, with the positive z-direction pointing from the pad plane towards the cathode (into the picture). The two other axes, x and y, are also indicated in the figure, with the x-axis approximately perpendicular to the pad rows and the y-axis approximately parallell to the rows.

Chapter 5

Reconstruction

As described in the previous chapter, the recorded data consists of the charge collected on the pads, sampled and digitized at 20 MHz. The raw data thus contains the sampled ADC values, channel number and time information of the collected *pulses*. A pulse is here defined as the samples that get grouped together as described above in section 4.7, containing at least two consecutive samples above a programmable threshold. The pulses are used as the basis for the recontruction procedure that is used to obtain an image of the original track and its properties. Because of diffusion, the primary electrons spread out during drift and the amplified charge collected at the readout plane will spread out over several pads. The centroid of the collected charge is determined to get an estimate of the position of the original track.

The first step is to reconstruct the individual pulses to get the arrival times and charges of the pulses. Since pedestal subtraction and zero suppression is done by the ALTRO, there is no need for this in the software.

After pulse reconstruction, pulses on adjacent pads that lie close to each other in time are grouped into *clusters* to get a projection of the track on the pad plane. A reconstructed image of the original track is obtained when the time information is used to calculate the third spatial coordinate.

After the clustering, a track finding routine is used to group the reconstructed clusters into tracks. This is an important part of the reconstruction. For example, it is essential to separate track clusters from clusters where some kind of noise, e.g. electronics noise, is the origin. A cluster chosen by the track finder is very likely a track cluster. The clusters grouped into a track are then used to reconstruct the properties of a track, such as the curvature and the energy loss of the particle.

The software performing the described reconstruction is written in C++ and is based on the ROOT framework developed at CERN. ROOT provides a large number of tools for data analysis, such as histogramming and fit methods. It is also useful for storage and quick access to the stored data. Every individual pulse, cluster and track is stored as a separate object using storage methods provided by ROOT.

In the following sections, the reconstruction steps are described in more detail.

5.1 Pulse reconstruction

Upon receiving a trigger, each ALTRO can sample and buffer 1024 10-bit ADC values. To limit the storage demands, only the data deemed relevant is saved to memory. As mentioned, this is done when at

least two consecutive samples have ADC values above the threshold (usually 4 ADC units). In addition to the samples lying above the threshold, three samples before and seven after the ones above the threshold are included in the pulse and saved. Thus, zero suppression is taken care of by the electronics. By doing dedicated pedestal runs between the data runs, with the beam shutter closed, the mean value and RMS of the pedestals can be determined. These values are stored in pedestal files, one for each data run, and are used for online pedestal subtraction performed by the ALTRO. Later, the pedestal files can be used in the data analysis, e.g. to find pulses where the electronics have been saturated. Thanks to the zero suppression and pedestal subtraction, the data will contain only a small amount of noise. Some noise will remain however but is later removed to a large extent by the tracking.

Two pulses in the same pad that are sufficiently close to each other in time will be stored as one pulse. This happens when the second pulse arrives before the first has fallen below the threshold. For an efficient track reconstruction, these pulses need to be separated and stored as separate pulses. To do this, the pulse reconstruction algorithm goes through the ADC values one by one and compares them to the preceding ones. It stores the value of the largest encountered ADC value and if one of the following samples have a value that is lower than this value, a peak has been found. A minimum difference of three ADC values are required to avoid false peaks resulting from noise fluctuations. A pulse object is created, where all samples in a peak are included up to the points where either the ADC values are below the threshold or if more than two subsequent samples are higher than the previous one, which would indicate a second peak. This second peak is stored in a new pulse object. The procedure is repeated in the event that even more pulses are encountered.

Since the second pulse arrives on the tail of the first one there will be some pile up. Hopefully this will be a small effect in most cases thanks to the fast decay time. For the first pulse it is of no concern that the tail is cut when the second pulse arrives since the tail is not used in the analysis.

When the samples have been assigned to pulses, the arrival time and the charge is calculated for every pulse. The ADC-value of the largest sample is used as an estimate of the pulse height and is taken as a measure of the charge. The time of the pulse is obtained as a voltage weighted mean of the five samples around the pulse. This value will be biased towards the central bin but this can be corrected for to a large extent. A discussion of this will follow in section 7.1. The output of the pulse finder is a new collection of pulses with reconstructed charge (in ADC units) and time values.

5.1.1 Bad channels

When a large number of readout channels are used, it is likely that some of them will be bad in some way. A number of channels might become more or less dead, i.e. they never or very seldom give any signals. They have to be taken into account when doing the clustering to avoid badly reconstructed clusters. A dead pad in the middle of a cluster will make two clusters out of signals that would normally be grouped into one single cluster.

In the beginning of the September 2010 run, a number of readout channels were dead or largely inactive. (Some channels can in fact get a negative pedestal which means that the pulse height will be misrepresented and such channels should be treated as bad). As the data taking progressed, more and more channels seemed to go bad. As of yet, we have no good explanation for this. One theory is that the channels were damaged in connection to the GEM voltage tripping but no such correlation has been established.

Whatever the reason for the damaged readout channels, the measurements can be improved if taking them into account. The current solution is to simply count the number of pulses in a certain channel and flag the channel as bad if the number is lower than a threshold value of 10 counts. This threshold is well below the average number of counts for a good channel while it is high enough for removing the bad channels since they, if they get any signals at all, typically register one or two pulses for an entire measurement of 20,000 events (most bad channels do not get any signals). The channel analysis is done

together with the pulse finding algorithm so that the bad channels information is available when doing the clustering.

5.1.2 Overflow

The ADC is capable of storing 1024 10 bit values. The amount of charge will be recorded up to the maximum ADC value. Pulses with larger amplitudes will be truncated above this value. (Actually it is a bit less, the maximum value is the maximum ADC value minus the mean pedestal value.) Naturally, the charge reconstruction will be affected by this but also the arrival time reconstruction since it uses the ADC values. Really high pulses will saturate the amplifier. Not only will they be truncated but they will also get an abnorm shape with a very long and high tail, see Fig. 5.1. In the reconstruction, pulses are flagged as being in overflow when the maximum ADC value of the pulse plus the pedestal value exceeds 1022.

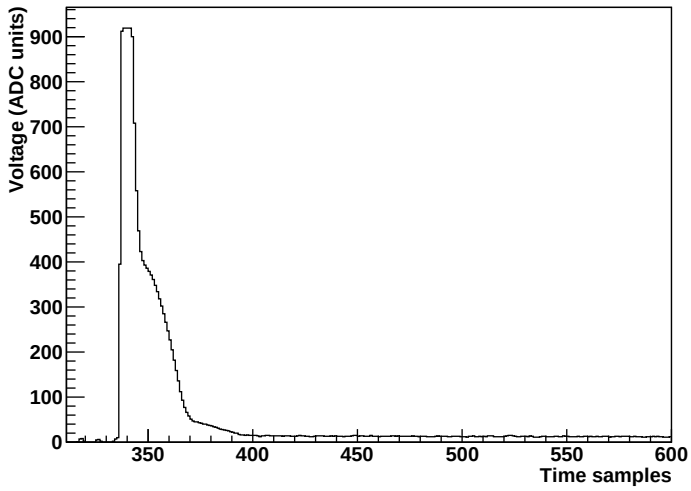

Figure 5.1: A pulse in overflow since the pulse height plus the pedestal is above the range of the ADC. The shape is distorted and the peak is trunctated. The pedestals are subtracted in the electronics so the pulse does not go all the way up to the maximum range of the ADC.

5.2 Clustering

The coordinates of a pulse is taken as the coordinates of the pad center on which the charge was deposited. Using these coordinates, neighbouring pulses in a single pad row are associated to form *clusters*. From these clusters, an image of the track, sampled at every $\sim 5mm$ (the length of a pad), can be reconstructed.

Working on a row by row basis, the first step of clustering in a row is to find the pad containing the pulse with the largest amplitude. Using this pad as a starting point for the cluster, a search is conducted outwards in the same pad row. If a pulse is found on a neighbouring pad, it is added to the cluster. To minimize the risk of associating pulses that are not really related, a time window in which the pulses must lie is defined around the first pulse. Should two pulses be found in the same pad, the one closest in time to the start pulse is chosen. The search continues until an empty pad or the edge of the instrumented region is reached. At this point, the algorithm stops and flags all included pulses as used. This allows the algorithm to find the remaining clusters in the row should there be more. Fig. 5.2 shows an example of a cluster.

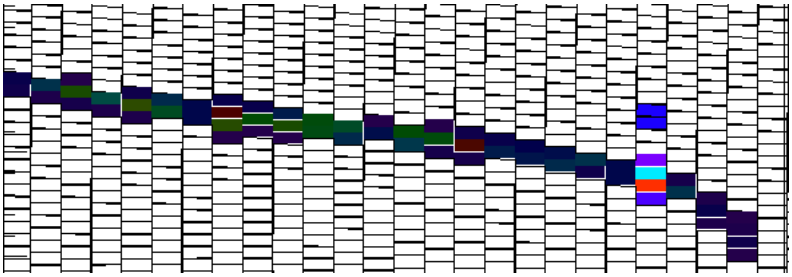

Figure 5.2: A magnified part of the pad plane, where a filled pad indicates a registered pulse. The highlighted row has two clusters, separated by two empty pads.

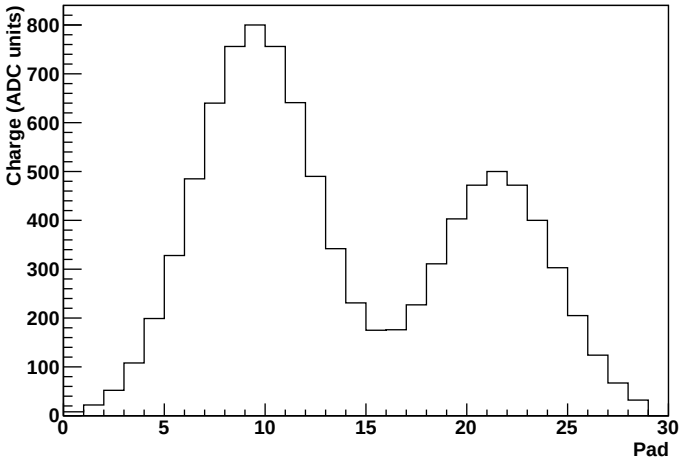

Figure 5.3: Example of what two clusters close to each other in space might look like in a single pad row. They will need to be separated in the software in order to be able to separate tracks which go close to each other.

If the algorithm reaches an empty pad that is marked as bad, it does not stop but skips the pad to see if there is a pulse on the other side which is then added to the cluster. A cluster formed around a dead channel is flagged to allow for its removal from the analysis. It should be possible to interpolate the charge for such an empty pad from its neighbours but since the amount of data is large it is better to just remove it. Another flag indicates if the cluster contains a pulse in overflow. Here it is probable that both time and charge is misrepresented and they should therefore also be removed.

Just as for individual pulses, there is a possibility that two clusters need to be separated. For example, if two tracks pass close to each other, in both time and space, the collected charge might be interpreted as one cluster. Since an individual cluster should have the largest amount of charge in the middle, due to the gaussian nature of the diffusion, two clusters lying close to each other will give a measurement looking approximately like Fig. 5.3. Such clusters are split in a similar way as the pulses described above.

When a cluster has been found, a number of quantities are calculated. Using the pulse charges as weight, the coordinates are found as the center of gravity of the involved pad coordinates, e.g.

$$x_i = \frac{\sum x_i Q_i}{\sum Q_i} \tag{5.1}$$

where x_i is the x-coordinate of the pad i and Q_i is the charge deposited in this pad. The same method is applied to the y and z coordinates where z is then the arrival time of the pulse. The total charge Q of the cluster is calculated as the sum of the included pulse charges Q_i.

5.3 Track finding

For tracking, a simple algorithm is used that performs well in a low track density and low noise environment. A cluster at the edge of the pad plane is chosen as starting point for a track following procedure. Since the pad plane is oriented with the beam along the long side (x-direction) of the pads, the next cluster in the track should be found in the neighbouring pad row. A search window is therefore defined around the start cluster in the drift direction (z) as well as in the y-direction. If a cluster is found within the y-z-window in the next pad row, it is added to the track candidate. If no cluster is found, the search continues in the next row. Here, a cluster must be found or the track candidate is rejected so that the track is not allowed to contain holes larger than one row. If more than one cluster is found, the one lying closest to the previous cluster in y is chosen.

The procedure is repeated with a new search window around the previous cluster until the other edge of the pad plane is reached. In order to be accepted, a track candidate needs to include at least 10 clusters and no more than two empty pad rows. The algorithm has been tested extensively and visual cross checks have confirmed that it works well.

When a track has been found, the involved clusters are flagged as belonging to a track. This enables reconstruction of multiple tracks in one event. To find as many tracks as possible, all clusters are used as seeds for a track (if they are not already in a track when their turn comes), one after the other. It is important to find multiple track events since they can often consist of low momentum tracks from conversion (most likely in the magnet) that will have an effect on the energy loss distribution. Also, low momentum tracks are more prone to multiple scattering which will have an effect on momentum determination.

In the end of the tracking procedure, a fit is made to the coordinates of the clusters. The straight tracks in the runs without magnetic field are fitted with a straight line and the helical tracks with magnetic field are fitted with a second order polynomial.

After the track finding has been performed one can have more confidence in that the selected clusters are part of a track. The occasional noise cluster might still be included in the analysis but given that the amount of noise clusters in a single event is fairly low to start with it should not be too common that an unwanted cluster fulfills the criteria (is inside the window) for both space and time.

5.4 Cuts

A number of cuts were implemented to ensure a high quality of the used data. Here a summary of all cuts is given, including the ones mentioned elsewhere. These cuts are used everywhere if nothing else is stated.

- First of all, a track candidate is discarded if a "hole" of more than two rows is encountered during the tracking. Second, a track is not used if it has a total of more than two misses, even if the individual holes are only one row wide.
- The tracks are required to have no clusters near the edges of the instrumented region in the y-direction (clusters in the edge rows are of course used). In this way, any edge effects are avoided. For example, clusters near the edges may be poorly reconstructed since parts of them are missing.
- Although the tracking is capable of finding multiple tracks, only single track events are used in the following analysis. This will minimize the inclusion of bad quality tracks that are the result of conversion in the TPC or magnet walls (at least the ones where more than one of the resulting tracks go through the sensitive region).

- Clusters containing pulses in overflow are not used since both charge and time information will be distorted by this.
- Clusters formed around bad channels are removed since the quantities calculated for this clusters, e.g. the cluster position, will be of bad quality. Since the amount of data is large, this can be done while still having sufficient statistics.
- The data taken in September 2010 contains noise from the electric motor used to move the table on which the magnet was placed. Even when the magnet was kept in position, the motor was used to keep it in place since there were no mechanical brakes. In the data, this is seen in some events as short intervals in time where all (or almost all) pads record pulses. Since this is highly localized, many of these events can still be used if the noise does not lie close in time to the track. Therefore, only the events containing noise close in time to the track are removed.

Chapter 6

Alignment correction

The data recorded in September 2010 suffers mainly from two problems. One is the distortions of the electric field caused by the improper setting of the field shaper. Like in July 09, the gating GEM was not installed but the ambition was to remove the distortions. However, the miscalculation of the voltage needed for the field shaper that was designed for this purpose seems to have made the distortions worse. The second problem is that the modules seem to be somewhat misaligned. It would of course be preferable to fix the problem directly in the hardware. However, since the data was already recorded and no additional measurements were scheduled before the scheduled completion of this thesis, a software solution was necessary.

A common approach in treating misalignment is to fit a large number of tracks and then calculate the residual distribution of the measured points. If this is done for each individual subdetector, the mean of the residual distribution for each such subdetector can be subtracted from the coordinates of the points measured there. This approach was used for some of the data taken in July 2009. This method has a slow convergence, many iterations are necessary, and the end result is likely to be biased in some way. Furthermore, it will not be possible to disentangle the distortion from the mechanical misalignment. Another approach will be described in this chapter. It is based on the Millepede program package, written by Volker Blobel [35], which will be described in section 6.2.

6.1 Least squares fitting

Given a set of measured points $(\mathbf{x}_k, y_k)$, where $\mathbf{x}_k$ is a vector containing the n independent variables of the measurement, the standard way of fitting a model to the data points is the least squares method. Say that one wants to fit a linear model to the points such that $y_k = \sum_{i=1}^{n} x_{ik} a_i + r_k$, where a_i are the n model parameters and r_k is the residual of the point, i.e. the deviation of the point from the fitted model. Here, linear means that the model is linear in the parameters, a linear least squares fit can for example be made for a parabola, which is not linear in the independent variables (x_i), as long as it is linear in the parameters (a_i). The linear least squares method amounts to minimizing the sum of the squared residuals for each point:

$$S = \sum_k \frac{(y_k - \sum_i x_{ik} a_i)^2}{\sigma_k^2}. \tag{6.1}$$

S is minimized, with respect to the parameters a_i, when the partial derivatives of S with respect to the parameters are zero. The sum runs over the number of measurements. With a bit of rearrangement, this

can be written as a set of n linear equations called the normal equations

$$\sum_k w_k \sum_i^n x_{kj} x_{ki} a_i = \sum_k w_k x_{kj} y_k \ (j = 1, 2, ..., n) \tag{6.2}$$

where j runs over the number of parameters and k over the number of measurements. w_k is here the weight of the measurement k given by the variance as $w_k = \frac{1}{\sigma^2}$. Eq. 6.2 can be written in matrix notation as

$$\mathbf{Ca} = \mathbf{by} \tag{6.3}$$

where $\mathbf{C} = \mathbf{X}\mathbf{X}^T$, $\mathbf{b} = \mathbf{X}^T$ and $\mathbf{X}_{ki} = w_k x_{ki}$. The best fit parameters are then obtained by inverting the matrix $\mathbf{C}$:

$$\mathbf{a} = \mathbf{C}^{-1}\mathbf{b}. \tag{6.4}$$

6.2 The simultaneous fit of global and local parameters ; the Millipede principle

If one subdetector is misaligned with respect to the other, e.g. one of the pad modules in this case, an alignment correction can be found by including it as a parameter in the fit. First, consider the case for one single track. Here, e.g. with a straight track, the sought parameters are the intercept and the slope of the track with respect to the defined coordinate system. These will be referred to as the local parameters, only relevant for one single track so that for one point y_k on the track

$$y_k = a_o^{loc} + a_1^{loc} x_k \tag{6.5}$$

where a_o^{loc} and a_1^{loc} are the intercept and the slope, respectively. A local solution can be found by matrix inversion just like in the previous section so that

$$\mathbf{a}^{loc} = \mathbf{\Gamma^{-1}}\beta \tag{6.6}$$

where $\mathbf{\Gamma}$ and β are defined in the same way as $\mathbf{C}$ and $\mathbf{b}$ in the previous section. In addition, because of the misalignment, there is one or more additional parameters that are relevant for all tracks, known as global parameters. In the example with a straight track, this means that the model becomes

$$y_k = a_o^{loc} + a_1^{loc} x_k + a_k^{glob} \tag{6.7}$$

where the global variable in this case represents a shift of the subdetector in the y-direction. The goal of the fitting procedure is therefore to find the global variables.

A simultaneous fit of all parameters will, when using a large number of tracks, give a huge matrix to invert which results in a long computing time. However, since the matrix is symmetric, and we are only interested in the global parameters, the problem can be greatly simplified. The complete equation is given by

$$\begin{pmatrix} \sum \mathbf{C}_i & \cdots & \mathbf{G}_i & \cdots \\ \vdots & \ddots & 0 & 0 \\ \mathbf{G}_i^T & 0 & \mathbf{\Gamma_i} & 0 \\ \vdots & 0 & 0 & \ddots \end{pmatrix} \cdot \begin{pmatrix} \mathbf{a}^{glob} \\ \vdots \\ \mathbf{a}_i^{loc} \\ \vdots \end{pmatrix} = \begin{pmatrix} \sum \mathbf{b}_i \\ \vdots \\ \beta_\mathbf{i} \\ \vdots \end{pmatrix} \tag{6.8}$$

In the upper left corner of the matrix, contributions $\mathbf{C}_i$ from all individual measurements are added to give a $n \times n$-matrix where n in this case is the number of global parameters. The matrices $\mathbf{\Gamma_i}$ for the individual measurements gives a contribution on the diagonal of the matrix. The last contribution to the matrix is given by the matrices $\mathbf{G}_i$ which contain information that relates the parameters of the

inidvidual measurements. The contributions to the rightmost vector are $\sum \mathbf{b}_i$ for the global parameters and $\beta_\mathbf{i}$ for the local parameters. Since we are only interested in $\mathbf{a}^{glob}$, the equation can be manipulated to give

$$\mathbf{C'a} = \mathbf{b'}. \tag{6.9}$$

The matrix **C'** and the vector **b'** are then given by

$$\mathbf{C'} = \sum_i \mathbf{C}_i - \sum_i \mathbf{G}_i \mathbf{\Gamma_i^{-1}} \mathbf{G_i^T} \qquad \mathbf{b'} = \sum_\mathbf{i} \mathbf{b_i} - \sum_\mathbf{i} \mathbf{G_i} \mathbf{\Gamma_i^{-1}} \beta_\mathbf{i} \tag{6.10}$$

Thus, the global parameters can be obtained without having to invert the large matrix. The only matrices that have to be inverted are the $\mathbf{\Gamma_i}$-matrices and the matrix **C'**, a square matrix of the same size as the number of global parameters, to give

$$\mathbf{a}^{glob} = \mathbf{C'}^{-1}\mathbf{b'}. \tag{6.11}$$

Millepede was used to perform the matrix inversion. It is written in Fortran and allows for linear least squares fits with a maximum number of 1000 global alignment parameters.

6.2.1 Constraints

If no constraints were applied to the parameters, the fit could move the detector in an arbitrary way, a large rotation of the entire detector could still give a good fit. To constrain the result, a parameter could for example be removed from the fit. For example, if the fit contained one parameter per subdetector that represented a translation, the parameter for one detector could be taken as reference and removed from the fit. Therefore, the translation of that detector is zero. If the position of this subdetector is considered to be known well enough, this can be a good method.

Another option available in Millepede is to use Lagrange multipliers. This can be useful if there is supposed to be a relation between the parameters. A linear constraint of the parameters a_i of the form

$$\sum a_i f_i = f_0, \tag{6.12}$$

with the Lagrange multipliers f_i, can be used to add the requirement to the fitting procedure that the above sum amounts to f_0. This modifies the normal equations to include the constraints but does not change the overall procedure since the new equation can be reduced in a similar way as described above.

6.3 Reference frame

To make the problem linear, the measured coordinates are translated from the detector system, defined in section 4.9, into a frame of reference related to the track. This means that every track has its own coordinate system but this will not have any significance for the global χ^2-calculation. The coordinate system is thus translated and rotated to have two points, the ones measured at row 14 and row 70 (the middle points of the outer modules), on the x-axis and at equal distance to the new origin. This makes a straight track essentially parallell to the x-axis and a curved track can be approximated by a parabola with symmetry axis at $x = 0$.

In the original reference frame, the (aligned) coordinates, $x_{k,al}$ and $y_{k,al}$, of a cluster are given by

$$\begin{pmatrix} x_{k,al} \\ y_{k,al} \end{pmatrix} = \begin{pmatrix} x_k \\ y_k \end{pmatrix} + \begin{pmatrix} 0 & -d\phi \\ d\phi & 0 \end{pmatrix} \begin{pmatrix} x_k - x_{modc} \\ y_k - y_{modc} \end{pmatrix} + \begin{pmatrix} \Delta x_{mod} \\ \Delta y_{mod} \end{pmatrix} \tag{6.13}$$

where x_k and y_k are the respective coordinates before the alignment correction, $d\phi$ is a (small) rotational misalignment of the pad module with respect to the center point of the module (x_{modc}, y_{modc}) and Δx_{mod} and Δy_{mod} is the translational misaligment in x and y respectively. The distortion is ignored for now.

In a rotated frame, with a translation of the system origin to the point (x_0, y_0) and a rotation with the angle θ the coordinates are given by

$$\begin{pmatrix} x'_{k,al} \\ y'_{k,al} \end{pmatrix} = \begin{pmatrix} cos\theta & -sin\theta \\ sin\theta & cos\theta \end{pmatrix} \left[\begin{pmatrix} x_k \\ y_k \end{pmatrix} + \begin{pmatrix} 0 & -d\phi \\ d\phi & 0 \end{pmatrix} \begin{pmatrix} x_k - x_{modc} \\ y_k - y_{modc} \end{pmatrix} + \begin{pmatrix} \Delta x_{mod} \\ \Delta y_{mod} \end{pmatrix} - \begin{pmatrix} x_0 \\ y_0 \end{pmatrix} \right] \tag{6.14}$$

Now, the aligned y-coordinate in the new reference frame will be given by

$$\begin{aligned} y'_{k,al} &= (x_k - x_0)sin\theta + (y_k - y_0)cos\theta + d\phi\left[(x_k - x_{modc})cos\theta - (y_k - y_{modc})sin\theta\right] + \Delta x_{mod}sin\theta + \Delta y_{mod}cos\theta \\ &= y'_k + \mathbf{a}^T \cdot \delta_{\mathbf{k}} \end{aligned} \tag{6.15}$$

where

$$\mathbf{a} = \begin{pmatrix} d\phi \\ \Delta x \\ \Delta y \end{pmatrix} \text{ and } \delta_{\mathbf{k}} = \begin{pmatrix} (x_k - x_{modc})cos\theta - (y_k - y_{modc})sin\theta \\ sin\theta \\ cos\theta \end{pmatrix} \tag{6.16}$$

In the example with straight tracks, the model for a single track is now

$$y'_{k,al} = a_0^{loc} + a_1^{loc}x'_k + \mathbf{a}^T \cdot \delta_{\mathbf{k}} \tag{6.17}$$

which is a linear model that can be used with the Millepede package.

6.4 Simulation

To verify that the written code does perform in the desired way, a simulation program was written to test it. A large number of tracks were therefore generated as straight tracks with random parameters close to the ones of the actual beam so that the simulated "beam" had about the same spread and a small variation in track angles. The simulated tracks were then sampled at 84 points with the y-coordinates smeared according to a gaussian distribution of width 0.07mm to simulate the finite resolution. The tracks were divided into three parts to simulate having three modules, and then the coordinates were given misalignment in x, y and a rotational misalignment corresponding to the specific module. Using 5000 tracks and the method described above, the misalignment parameters could be recontructed in a good way, see table 6.1.

Parameter	Simulated	Reconstructed
Δy_{mod1}	0	fixed
Δy_{mod2}	-1.55mm	-1.55577
Δy_{mod3}	1.33mm	1.33147
Δx_{mod1}	0	fixed
Δx_{mod2}	1.12mm	1.12089
Δx_{mod3}	-1.23	-1.2368
$d\phi_{mod1}$	0	fixed
$d\phi_{mod2}$	0.01434	0.0143401
$d\phi_{mod3}$	-0.005256	-0.00526997

Table 6.1: Simulated geometric misalignment parameters and the parameters reconstructed by Millepede.

In reality, the distortions of the electric field makes the situation more complicated. Not only is there a possible misalignment of the module coordinates, but the distorted electric field will have an effect on the drift of the electrons near the amplification structure. In this work, the assumption is that this produces a shift in the y-coordinate of a cluster, even if the situation in reality is more complex. The distance to the source of the distortion should determine the size of the shifts. Therefore, the size of the shift should depend on the row number and the y-position of the track. The assumption is that

the distortions vary sufficiently slow so that for one run, i.e. with the beam aimed at the same impact position during the entire run, the distortions will only be row-dependent even if the beam has a certain spread. Thus, the distortions will have the same (row dependent) magnitude throughout an entire run. For another run however, with the beam aimed at a different location, the distortions will have a different size. Therefore, any alignment attempt must take this into account. This is done here by adding an alignment parameter that represents a translation in y for every row. For each row, this parameter is different for different impact positions. Of course, the distortion will vary within a row as well, but there is no better information on the x-position. Furthermore, it should be safe to say that the size of the distortions is at a minimum in the middle pad rows since they are the farthest away from the source of the distortion. Therefore, the distortion correction parameters for the three middle rows of each module are kept fixed. To simulate the distortion, a fourth order polynomial was used to shift the cluster coordinates so that the middle clusters received only very small shifts. By varying the parameters of the polynomial, the different distortions of different runs were simulated. Three different runs with different impact parameters were simulated in this way, i.e. with different parameters of the distortion polynomial between the runs. The track model now becomes

$$y'_{k,al} = a_0^{loc} + a_1^{loc} x'_k + \mathbf{a}^T \cdot \delta_{\mathbf{k}} \tag{6.18}$$

with

$$\mathbf{a} = \begin{pmatrix} d\phi \\ \Delta x \\ \Delta y \\ \Delta_{y,row} \end{pmatrix} \text{ and } \delta_{\mathbf{k}} = \begin{pmatrix} (x_k - x_{modc})cos\theta - (y_k - y_{modc})sin\theta \\ sin\theta \\ cos\theta \\ cos\theta \end{pmatrix} \tag{6.19}$$

Using this model, on the simulation with distortions added, the precision of the reconstruction is reduced. However, combined with a constraint on the row by row-corrections, it is still possible to get back the original misalignment parameters with pretty good accuracy. Without constraint, it is possible that the free movements of the row-by-row distortion correction parameters amounts to a net rotation of a module, absorbing part of the rotation that should have gone into the rotation parameter $d\phi$. Using Lagrange multipliers for the constraint, according to

$$\sum_{row} \Delta_{y,row}/(x_{row} - x_0) = 0, \tag{6.20}$$

the net rotation produced by the distortion correction parameters is constrained to 0. Here, x_{row} is the x-coordinate of the center of the middle pad in the row and x_0 is the x-coordinate of the middle pad of the middle row. One such constraint is added per module and impact position. Now, the reconstructed alignment parameters are (not citing the distortion correction parameters) given in table 6.2.

Parameter	Simulated	Reconstructed
Δy_{mod1}	0	fixed
Δy_{mod2}	-1.55mm	-1.54611
Δy_{mod3}	1.33mm	1.34671
Δx_{mod1}	0	fixed
Δx_{mod2}	1.12mm	1.11796
Δx_{mod3}	-1.23	-1.20834
$d\phi_{mod1}$	0	fixed
$d\phi_{mod2}$	0.01434	0.0141653
$d\phi_{mod3}$	-0.005256	-0.00533523

Table 6.2: Simulated geometric and distortion misalignment parameters and the parameters reconstructed by Millepede.

Of course, the real situation is more complicated with many sources of error not accounted for in this simulation but these results should give confidence in the method.

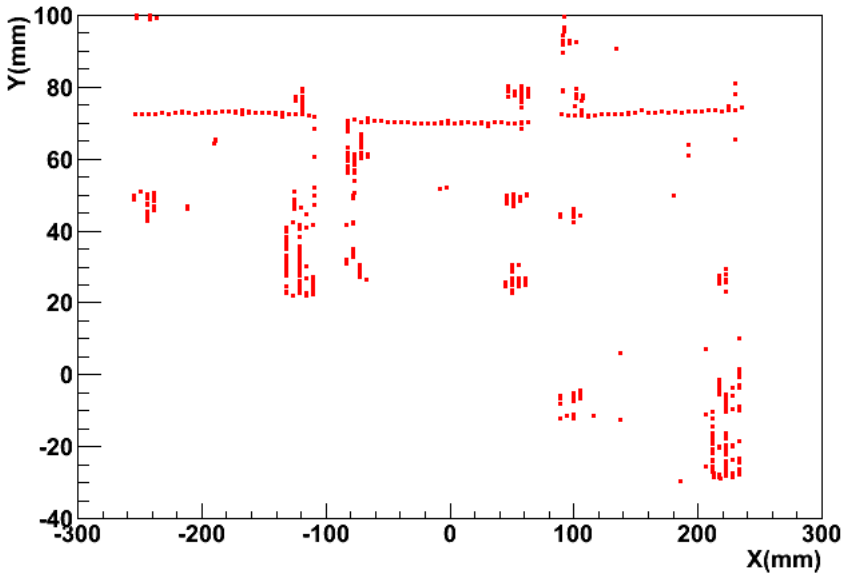

Figure 6.1: Example of a track that should be straight since the magnetic field is turned off.

6.5 Alignment for straight tracks

By looking at reconstructed tracks from data taken without magnetic field, it is easy to get an appreciation of the misalignment. Fig. 6.1 shows an example of a track that should be straight (since the magnetic field is turned off). Since it is clearly not straight, it is misrepresented in some way, whether it is from mechanical misalignment (or perhaps mapping issues in the software) or related to the distortions of the electric field. Another way to see the misaligment is to look at the residual distribution from a fit to the cluster coordinates of each track. If it is plotted against pad row, the distribution should line up around zero. In Fig. 6.2 it is clearly seen that they do not. The different shapes of the residuals for the different modules is obviously dependent of the impact position of the track.

An attempt to correct for the errors present was made with the method described above. If the errors are due to both mechanical misalignment and the distortions, a correction should take both into account. The magnitude of the coordinate deviation of a specific cluster depend on the distance of the cluster to the support pillar causing the distortion. If it is assumed that the distortions are not y-dependent (which, as we shall see, is not true) it should be possible to make a row-by-row correction of the distortions as described in the previous section. The magnitude of the deviation should vary within a row as well but there is no better information on the x-position than the one given by the coordinate of the center of the pad. In addition to distortion corrections, one alignment parameter corresponding to a translation in y and one corresponding to a small rotation was added. Also, some kind of constraint is necessary. Without a constraint, the detector could for example rotate in an arbitrary way and still give a good fit. To avoid this, one module is fixed by removing the translation and rotation parameter of that module from the fit. Since the distortions should be smallest in the module centres, the parameters for the distortion correction are fixed for the middle row of each module. Furthermore, the distortion parameters in each module are constrained to produce an overall rotation of zero. Without this constraint, the modules could receive large translation parameters which together with a large rotation by the distortion parameters would still give a good fit. The rotation constraint is added using the Lagrange mulitiplier method discussed earlier, using one such constraint for each module and run.

The track model is therefore

$$y'_{k,al} = a_0^{loc} + a_1^{loc} x'_k + \mathbf{a}^T \cdot \delta_{\mathbf{k}} \tag{6.21}$$

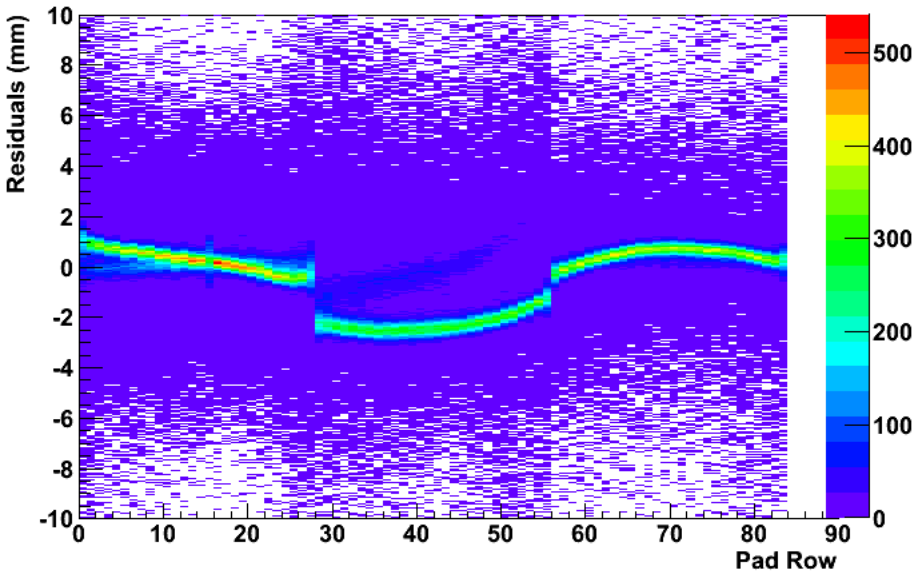

Figure 6.2: Residuals from a straight line fit to the cluster coordinates of a large amount of tracks going in the region close to the track shown in Fig. 6.1. Clearly, they are not distributed around zero as they should be.

with $\mathbf{a}$ and δ_k defined in eq. 6.19.

When the above procedure is applied to data from a run without magnetic field, the resulting residual distribution, with corrections added to the cluster coordinates, looks like Fig. 6.3. The residuals line up around zero as they should. However, if the same corrections are applied to tracks from another run, where the beam particles are impacting through a different region of the chamber, the result looks like Fig. 6.5. The different regions are indicated in Fig. 6.4, together with the locations of the support pillars. The distribution of residuals in Fig. 6.5 shows that the correction does not work for tracks from a different region. This is to be expected since the distorsion depends on the impact position of the track.

To account for the distorsion being different depending on the region where the track goes, different distortion correction parameters are used. The tracks are required to be within a narrow region (defined differently for different regions) of about 1 centimeter. In this way, tracks with large scattering angles from interactions in the magnet or chamber walls are removed. In such a narrow region, the distortions should be reasonably similar for all clusters in one row. In practice, three different runs were used where the beam was aimed at a different position in y for each run. Therefore, each impact point had a different set of distortion parameters, in contrast to the module rotation and translation parameters where the same parameters were used for each run. For a single point then, the track model was modified to have different distortion correction parameters for the different impact points.

The residual distributions for two different impact points of the beam particles, after corrections from the procedure described above have been applied, are shown in Fig. 6.6. As can be seen here, the correction now manages to line up the residuals around zero in both cases. It should be noted, that the lack of external reference points makes it difficult to reconstruct absolute alignment parameters, i.e. there could for example be a misalignment of the module kept fixed in our alignment procedure. However, the method should give an appreciation of the internal misaligment and provide a new geometry description of an internally aligned detector. Of course, the distorsion, being more complicated than the simple approximation made in section 6.4, complicates the alignment procedure and a more detailed investigation should include some kind of modeling of the distortions.

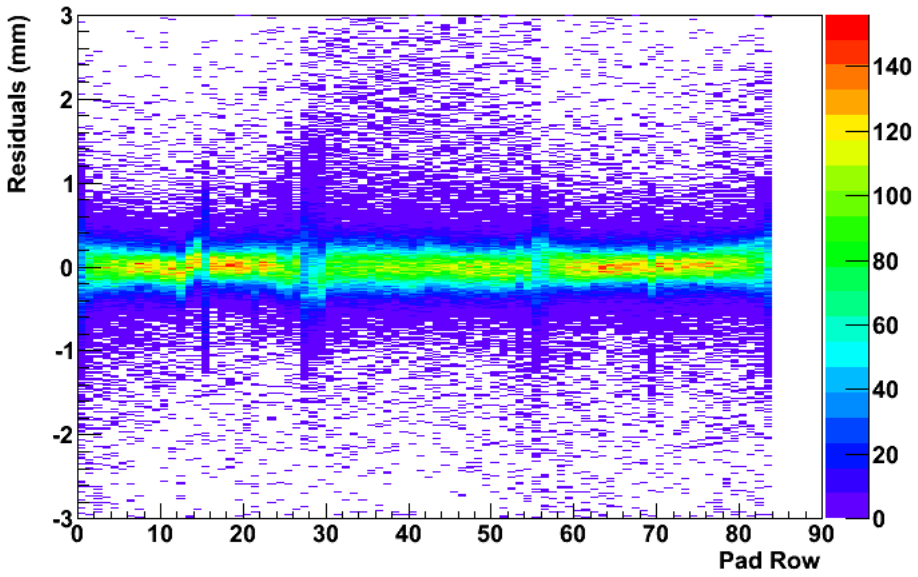

Figure 6.3: Residuals from a straight line fit to the cluster coordinates of tracks in the same region as in Fig. 6.1 after corrections have been applied. The situations is obviously improved compared to Fig. 6.2

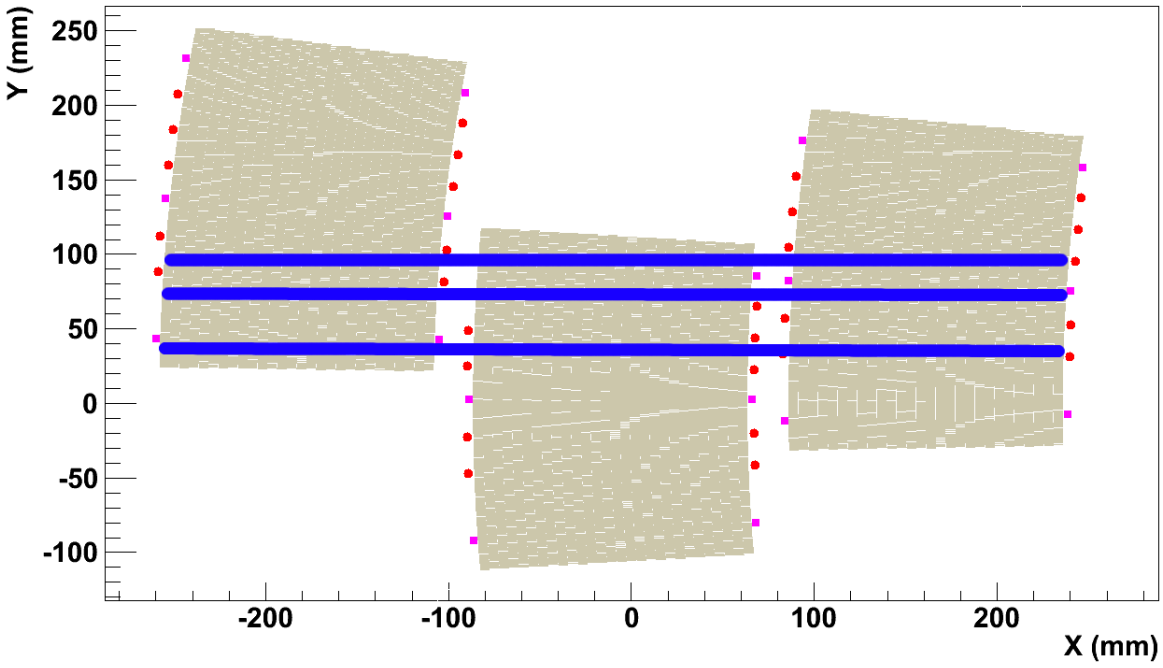

Figure 6.4: Sketch of the three modules used in the measurements. The approximate location of the beam, in the three different regions used, is indicated by the lines in the figure. On the module edges, the location of the GEM support pillars are indicated by squares.

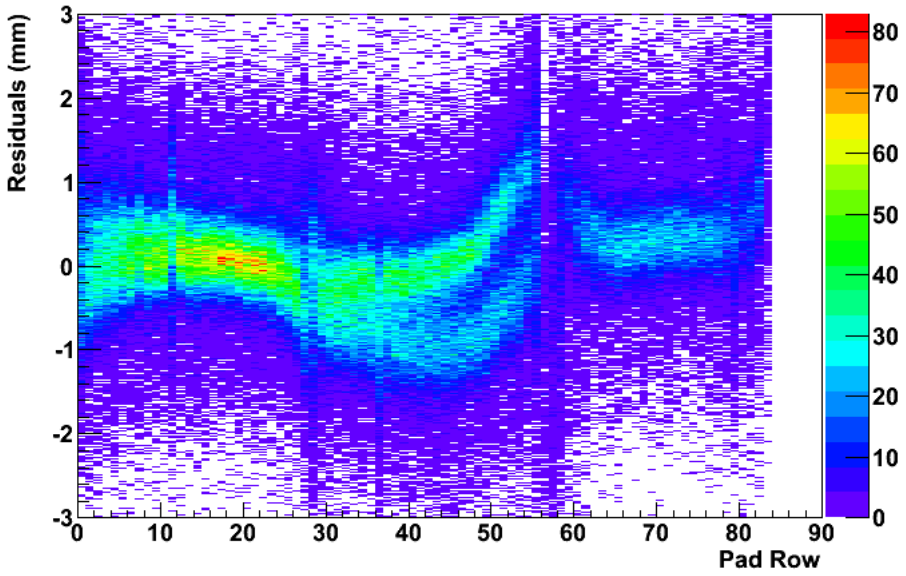

Figure 6.5: Residuals from a straight line fit to the cluster coordinates for tracks with the lowermost impact position shown in Fig. 6.4 after corrections corresponding to the middle impact position in Fig. 6.4 have been applied.

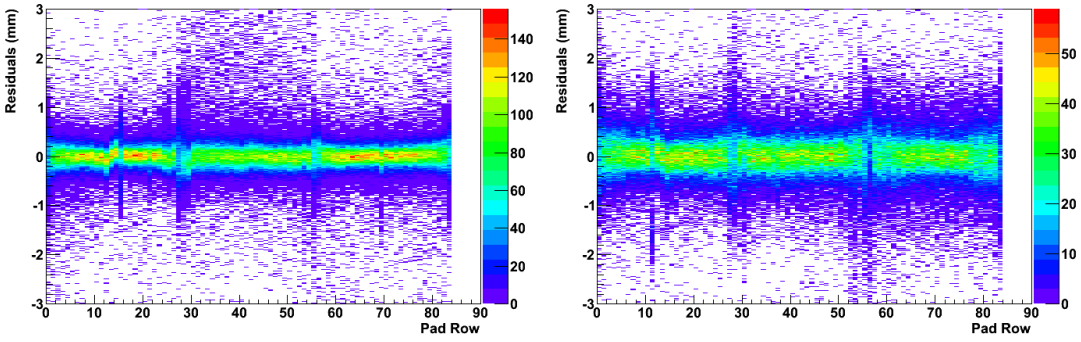

Figure 6.6: Residual distributions plotted against pad row for tracks with impact positions corresponding to the middle (left) and lowermost (right) impact positions shown in Fig. 6.4. The different widths of the distributions is due to different drift lengths where the drift length to the left is 50mm and the one to the right is 100mm. Since the y-dependence of the distortions have been taken into account, the correction works better.

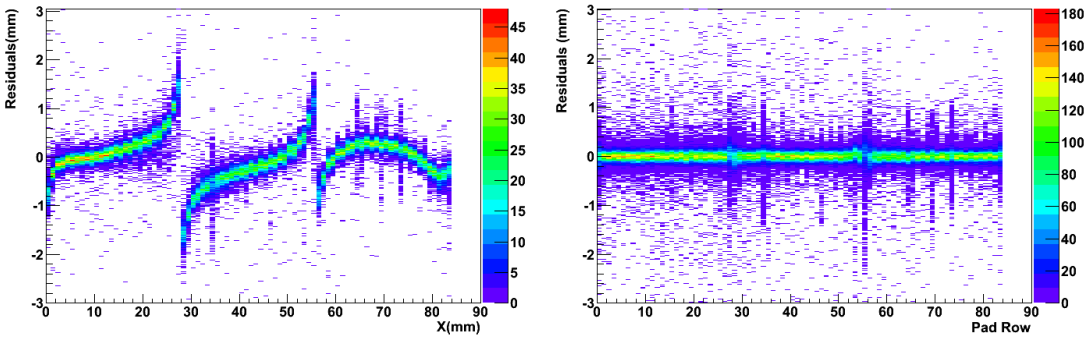

Figure 6.7: A comparison of the residual distributions versus pad row before (left) and after (right) distortion correction. After doing the correction, the residuals line up nicely around zero.

6.6 Alignment for tracks in the magnetic field

When a magnetic field is applied over the detector, $\mathbf{E} \times \mathbf{B}$-effects, resulting from the fact that the $\mathbf{E}$-field distortions give rise to an electric field that is not parallell to the magnetic field, will be present. This means that the distortions will not be comparable to the ones found with straight tracks. However, the alignment of the modules should still be valid. Thus, keeping the alignment corrections for the modules and locking the modules in this position, it should be possible to find the distortions also for the magnetic field runs. Thus, the model in a single point, with module alignment corrections already applied, is:

$$y_k = a_0^{loc} + a_1^{loc} x_k + a_2^{loc} x_k^2 + a_{row}^{glob} \tag{6.22}$$

where the only global parameter is the distortion correction and the circular track has been approximated with a second degree polynomial. Again, it is assumed that the distortion is smallest at the module center and the distortion correction parameters, a_{row}^{glob} are kept fixed for the middle three rows. A simulation, similar to what was made for straight tracks, was made also in this case. Using a fifth degree polynomial to simulate the S-shape given to the residuals by the $\mathbf{E} \times \mathbf{B}$-effect, the alignment procedure reproduces the row by row-shifts with good accuracy.

In Fig. 6.7, a comparison of the residual distributions before and after the distortion correction, made using 10000 tracks, can be seen.

Chapter 7

Analysis

7.1 Pulse timing

When analogue pulses with the rise times available here (30, 60, 90 or 120 ns) are digitized at a frequency of 20MHz (see Fig. 4.12), typically one or two samples are included to describe the rise of the pulse. This causes the arrival time of the pulse to be ill defined. Therefore it does not work well to use timing methods depending on the rising slope, like in constant fraction discrimination which is otherwise commonly used. A fit to the pulse shape should provide the best result but gives long computing times if a fit has to be performed for every single pulse. A less demanding approach is to take a voltage weighted average time (i.e. using the ADC values of the samples as weight) of the samples around the peak value. If this can be shown to give results comparable to the fit, a large reduction in computing time can be achieved. To begin with, the case with a shaping time of 120 ns will be described.

When this method is used for a large number of events, it becomes clear that the calculated values are biased. In Fig. 7.1 one can clearly see that the distribution is biased towards integer values which gives large empty regions in between. In Fig. 7.2 on the other hand, the same distribution calculated from a fit to the pulse shape is shown. The result is a smooth distribution without the holes observed in Fig. 7.1. Note that in both figures, t is given in time samples, i.e. number of time samples after a trigger was received, rather than actual time where one sample corresponds to 50ns.

To investigate how the reconstructed time is related to a known absolute time, a simple simulation was made. The time dependence of a pulse can be described by the Γ_4-function $A\left(\frac{t-t_0}{\tau}\right)^4 \exp\frac{-4(t-t_0)}{\tau}$, where t_0 marks the starting point of the pulse, and τ and A are related to the width and the height, respectively. By generating a pulse using this function and sample it at integer values, i.e. evaluating the function at integer time values and round off the corresponding amplitude to an integer value, a digital representation of a known pulse shape is obtained. The empty regions in the reconstructed distribution and the fact that they are of the same size and location with respect to the integer values, indicate that the effect depends on where the pulse arrives with respect to the sampling. By varying the parameter t_0 of the Γ_4-function, the starting point and therefore the entire pulse will be moved. If this is done in small steps between two integer values, it is possible to reconstruct the effect seen in the recorded data (Fig. 7.1). The right plot in Fig. 7.3 shows how the values reconstructed from the digitized function are distributed for 1000 samples where the pulse has been moved in time steps of 1/1000. For comparison, the t-distribution of the peak values from the Γ_4-function is shown to the left Fig. 7.3. This is of course a flat distribution.

By plotting the time from the function maximum against the values obtained from the voltage weighted average method (Fig. 7.4) it becomes clear that some values cannot be reached with the method using

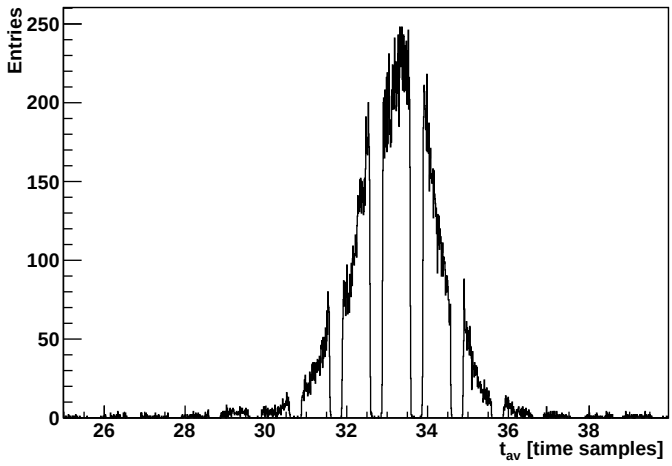

Figure 7.1: Pulse arrival time reconstructed using a weighted average of the five samples around the peak. The values are clearly biased towards the integer values, leaving large empty regions in the distribution. The shaping time of the pulses in this run was 120 ns.

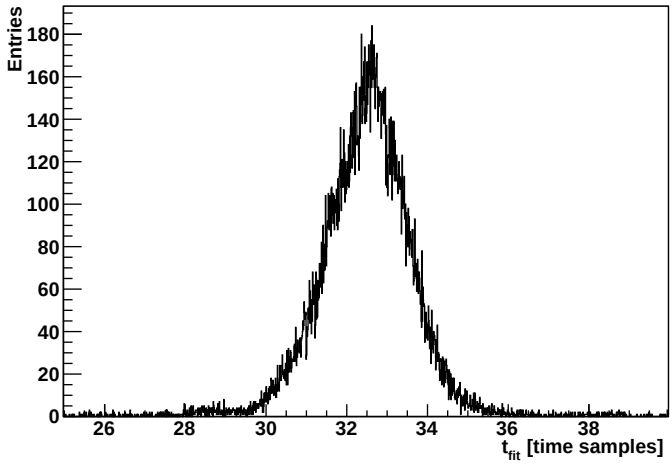

Figure 7.2: Pulse arrival time for the same run as in Fig. 7.1, but now with the time taken as the point where the function fitted to the pulse has its maximum value. It does not contain the empty regions observed in the previous plot.

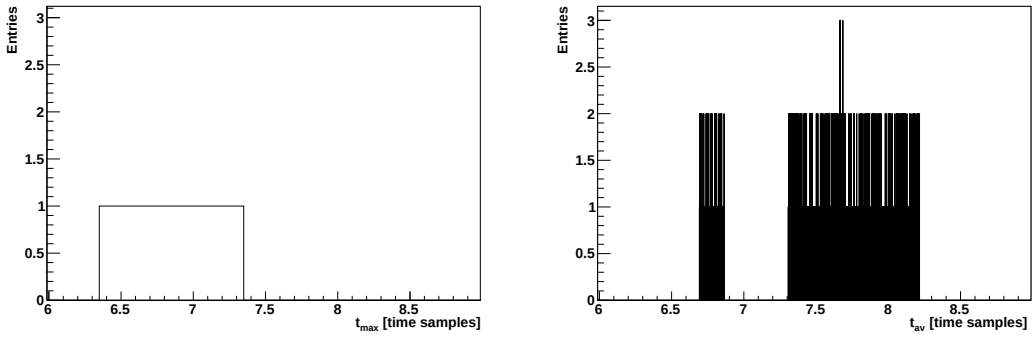

Figure 7.3: The left figure shows the distribution of t_{max} for simulated data, where t_{max} is the time value where the Γ_4-function has its maximum. The right figure shows the distribution of values obtained from the voltage weighted average method for the same sample. It exhibits the same features as the recorded data with an empty region in the middle.

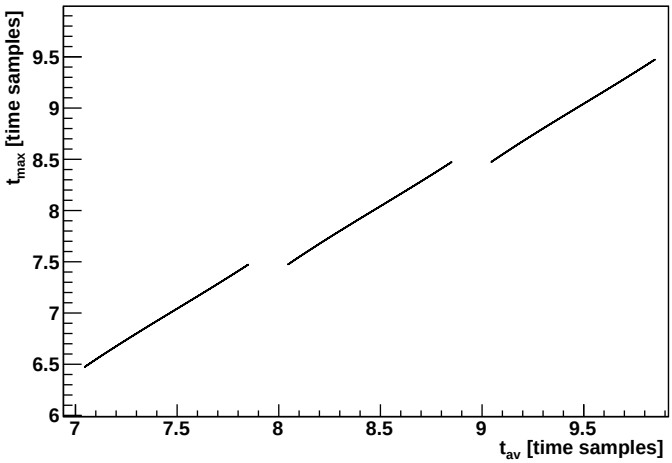

Figure 7.4: The time of the peak value from the Γ_4-function against the time value obtained from the voltage weighted average method for simulated data.

the average. Luckily, there seems to be a largely linear relationship between the values from the voltage weighted average method and the "true" value from the function. It should therefore be possible to apply a correction to the reconstructed values to reduce the bias. If examined closer, the relationship is not entirely linear, there is a slight wiggle. This is however very small and the effect becomes even smaller if the procedure is performed without a truncation of the sampled values. In real data, this effect is not seen since the width of the pulse is not as sharply defined as in the simple simulation used above. Thus, since the width varies somewhat, the lines of Fig. 7.5 (explained in the two following paragraphs) are not as sharp as in Fig. 7.4 and the non linear effects are therefore hidden.

In real data, there is no absolute time available for comparison. A fit should however provide the best time estimation provided that the pulse shape is accurately described by the fit function. To avoid noise interference, a maximum of two samples before the peak is used in the fit of the complete pulse.

To extract a time from the fitted function, the point where the function has a local maximum to the right of t_0 is chosen (the function has its minimum in this point and grows rapidly on the left side of t_0). When this is plotted against the values reconstructed by the charge weighted average method (Fig. 7.5), a similar structure as the one observed in the simulation can be seen.

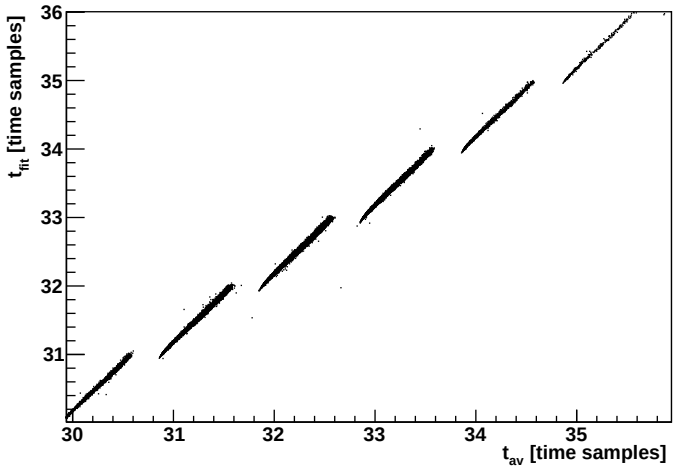

Figure 7.5: Time calculated from the fit plotted against the time value obtained from the voltage weighted average method for real data.

By applying a linear correction to the reconstructed values, it is possible to close the gaps in the distribution with the result that the averaged values represent the fit values more accurately. From Fig. 7.5 it is evident that each time value reconstructed from the weighted average (t_{av}) corresponds to a unique time from the fit (disregarding that there is a certain width in the distribution) and that the values of t_{av} are biased towards the integer values. The slope from a straight line fit to (one of) the cohesive regions of the plot can therefore be used to close the gaps in the distribution. The result can be seen in Fig. 7.6 and Fig. 7.7.

To investigate the pulse shape more closely and get a visual indication of how well the reconstructed time values can be used to determine the pulse time, another test was performed. A direct comparison to the Γ_4-function can be obtained if the ADC value V_{sample} of each sampling step, normalized to the maximum voltage V_{max} (in ADC values taken from the fit) of the pulse, is plotted against the difference $t_{sample} - t_{calc}$. Here t_{sample} is the time of each sampling whereas t_{calc} is the arrival time of the pulse obtained from a fit to the complete pulse (Fig. 7.8 left) and using the charge weighted average method (Fig. 7.8 right), respectively. By visual inspection, it seems that the pulse shape is well represented by the function. The narrow distribution of points on the rising slope indicates that the reconstructed time is stable with respect to the leading edge, for both cases. The leading edge distribution actually seems somewhat wider for the times reconstructed using the fit to the pulse shape. This can be remedied by reducing the number of points included in the pulse fit. If only two points after the largest sample are used in the full fit procedure, the leading edge looks similar to the one in the averaged distribution. It seems therefore, that the tail of the pulse contains a slow component that makes the width, and thus the time of the fitted local maximum, fluctuate. This is also supported by the fact that in both cases, the tails are wider than the leading edge.

When the fit is done with a fixed width (τ), the distribution of points on the leading edge gets even more narrow. This also has an effect on the distribution from the average method, since this is normalized to the height taken from the fit. It is difficult to tell which method gives the best results. It should be safe, however, to say that the pulse is very well described by the function once the tail has been removed. Also, it seems that both methods provide a good estimation of the arrival time, although it is difficult to say which one is the best. In any case, the average method offers a significant reduction in computing time and gives results comparable to the full fit method.

The linear correction function does not depend on the drift distance. An investigation shows that the result of Fig. 7.7 is obtained regardless of drift distance and gain, i.e. the same linear correction is valid for different distances and gains. This does not hold for different shaping times of the amplifier though.

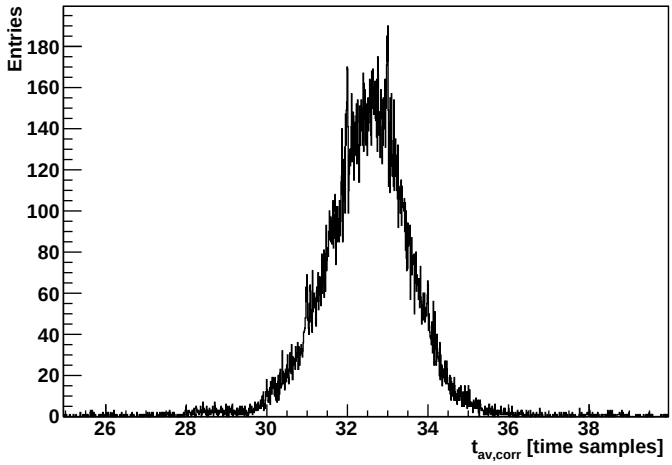

Figure 7.6: Distribution of pulse times from the average method with the linear correction applied. The holes in the distribution are no longer visible.

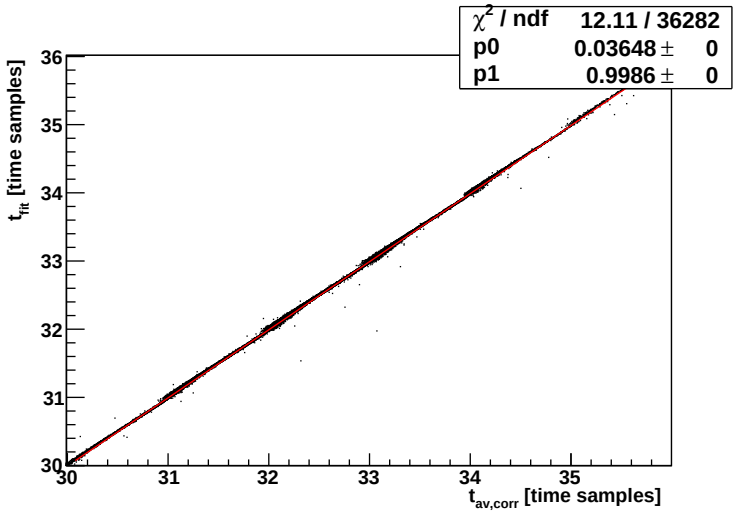

Figure 7.7: The time from a full fit of the pulse against time values obtained by the voltage weighted average method with the linear correction applied. Notice that the slope is very close to 1.

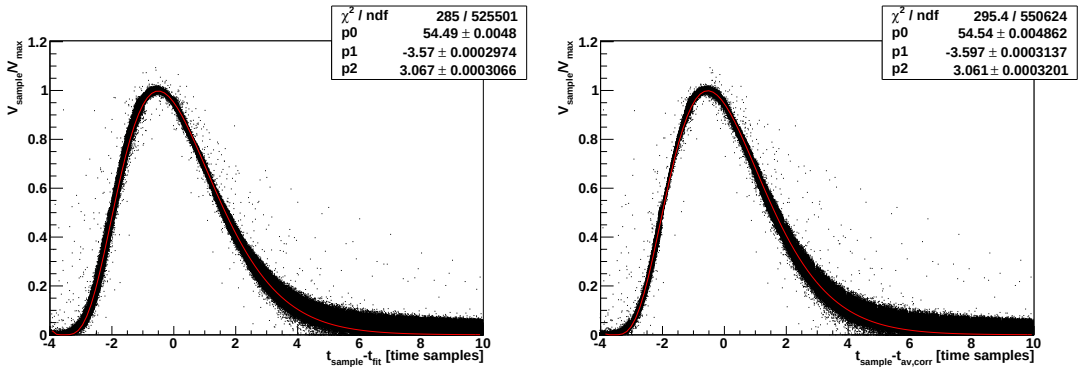

Figure 7.8: Scatterplots of the pulse shape.

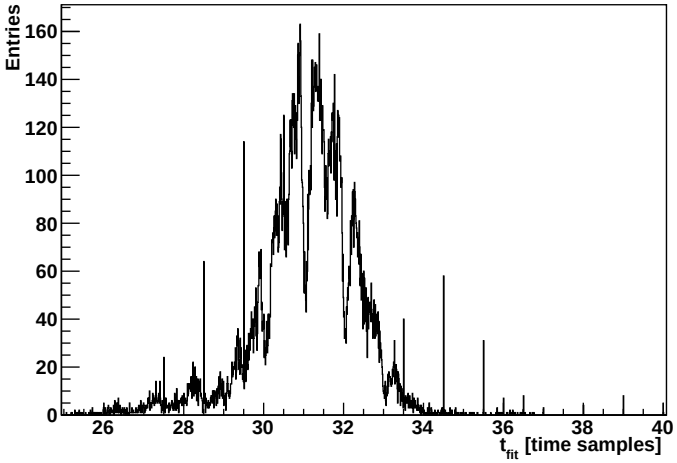

Figure 7.9: Distribution of pulse arrival times taken from a Γ_4-fit to the pulse shape. The shaping time is here 60 ns.

In this case, the pulse lengths differ between the different shaping times. It also appears to be the case that pulses with a shorter shaping time than 120 ns are not as well described by the Γ_4-function. When the function is used to extract time from shorter pulses, the distribution of arrival times looks like the one in Fig. 7.9, where data from a run using a shaping time of 60 ns is shown. An effect can be seen that is similar to the one in Fig. 7.1, i.e. there are once again empty regions in the distribution. Doing a similar scatter plot as in Fig. 7.8 also shows that the pulse is not well described as can be seen in Fig. 7.10.

To solve this, a different order, k, of the fit function was used according to

$$A\left(\frac{t-t_0}{\tau}\right)^k e^{\frac{-k(t-t_0)}{\tau}}, \tag{7.1}$$

inspired by [36]. For the example of a shaping time of 60 ns, a value of $k = 9$ was found to give a better description of the pulse as shown in Fig. 7.11 and Fig. 7.12. This works well for shaping times 60, 90 and 120ns with the order k of 9, 5 and 4 respectively. However, for a shaping time of 30ns, it is difficult to get rid of the holes in the distribution. In Fig. 7.14 this distribution is shown, where an order k of 20 has been used (a large number of k-values was tried and no improvement could be seen). It is reasonable that there should be difficulties in this case since the short shaping time of 30 ns, meaning that the pulse should reach its maximum within this time, means that the entire leading edge of the pulse is shorter than the sampling interval of 50ns (the sampling frequency is 20MHz). Therefore, only one point of the leading edge will be represented in the digitized pulse. To get a better representation of such pulses, a higher sampling rate is needed. Since the distribution of arrival times could not be used to determine what function that best describes the pulse, an order of eq. 7.1 that gave a smooth looking scatter plot of the kind shown in Fig. 7.8 was used. This gave a value of $k = 15$. This should probably be taken with a grain of salt however, since it seems to be difficult to obtain a good description without a higher sampling rate. For all the shaping times except 30ns, it was possible to make a linear correction to the time values obtained by the voltage weighted average method described above. In the case of 30ns, a plot of the "fit time" against "averaged time" gave a more obvious non linear behaviour as depicted in Fig. 7.13. No effort was made to find a correction function that better fitted this case since it will probably have a simpler behaviour with an increased sampling rate.

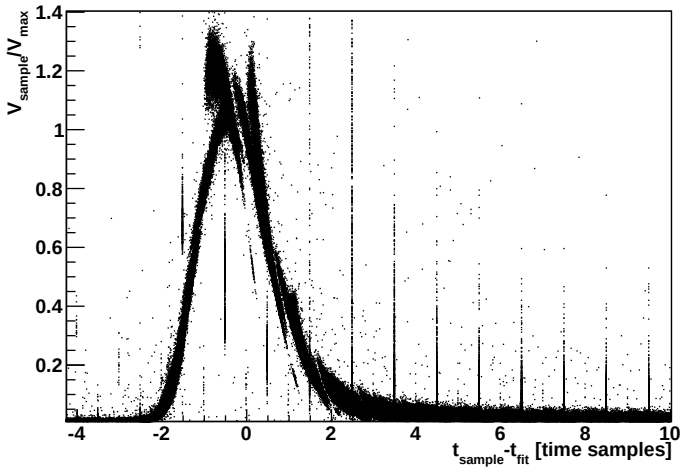

Figure 7.10: A scatter plot of the pulse shape obtained using the same method as in Fig. 7.8. It seems that the function does not describe the pulse well in this case.

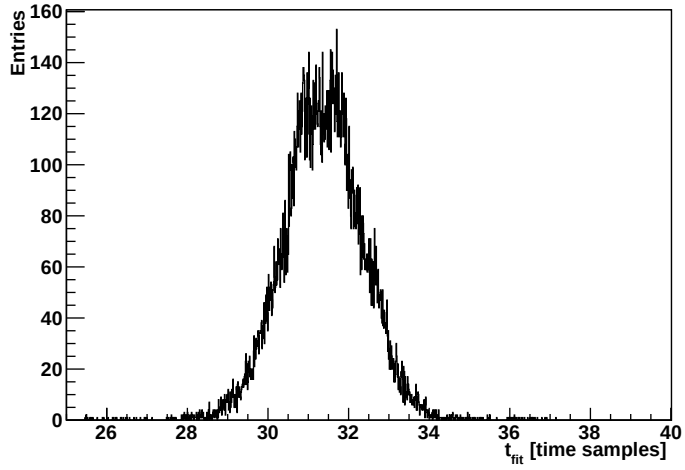

Figure 7.11: With a different function, the distribution of arrival times taken from the fit no longer has the holes shown in Fig. 7.10. The shaping time is still 60 ns and the fit function is eq. 7.1 with $k = 9$.

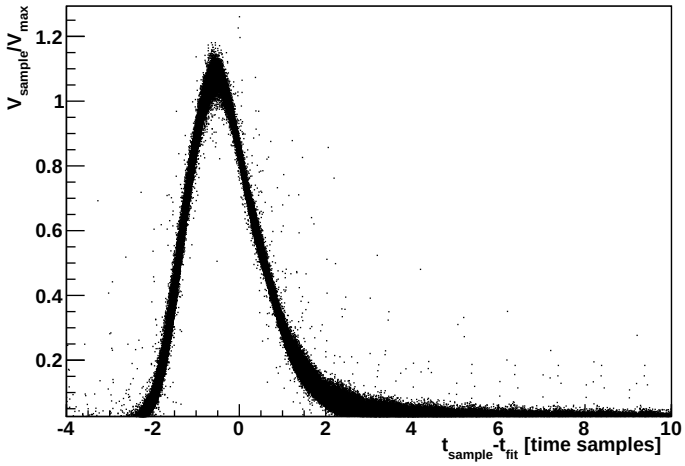

Figure 7.12: Scatter plot of the pulse shape (for a shaping time of 60ns) using an order $k = 9$ of the fit function.

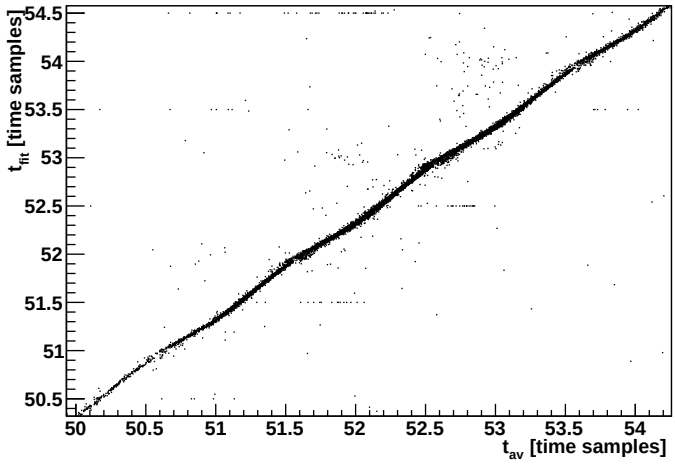

Figure 7.13: Pulse time as taken from the fit plotted against pulse time from the voltage average for a shaping time of 30ns. The behaviour is more wiggly than in the cases with a longer shaping time.

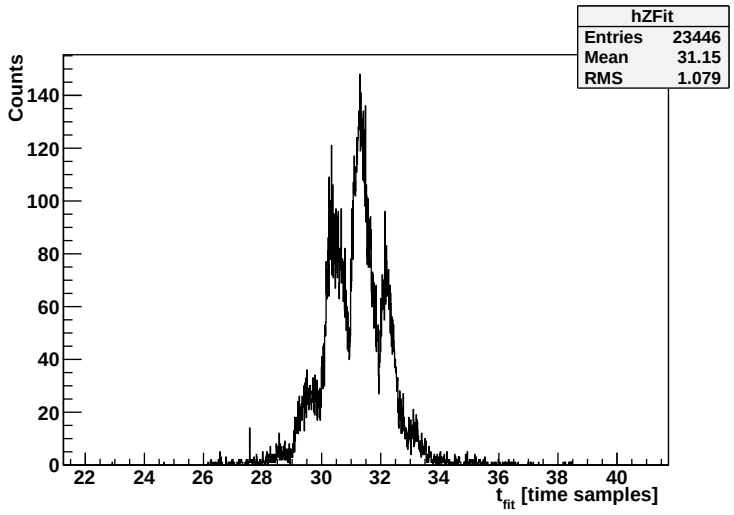

Figure 7.14: Pulse arrival time taken from the fit of pulses with a shaping time of 30ns using order $k = 20$ of the fit function.

7.2 Spatial Resolution

The spatial resolution, σ, is a measure of how well the reconstructed coordinates represent the original track. If the position of the original track was known, the measured points should thus be distributed around the "true" trajectory of the track. The resolution is usually taken as the width of a gaussian fitted to the distribution of the cluster coordinate deviations, the *residuals*, from the true track position. To find this distribution, the parameters of the track are needed. A measure of the track in another detector, with better resolution than the one expected in the TPC, would be desirable. Such a measurement would not be affected by possible detector effects in the TPC, like for example an inhomogeneous magnetic field, that might bias the track information. It could thus be used to study such effects. Unfortunately, the silicon detectors planned to be mounted around the TPC, were not ready at the time of data taking. Therefore, the tracks are in this analysis approximated by a fit to the cluster coordinates. A linear fit is made in the x-z projection and also in the x-y-projection for runs without a magnetic field. For the runs with the magnetic field on, the helical tracks are instead approximated by a second degree polynomial in the xy-plane.

The method of using a fit for the track position gives a biased resolution since the points investigated are used to get the track information. If the fit is performed without the specific cluster for which the residual is to be determined, the estimate will also be biased and give a too pessimistic value. The common solution to this is to take the geometric mean of the widths of both distributions, one calculated with the investigated point included and one without. Thus,

$$\sigma = \sqrt{\sigma_{incl} \cdot \sigma_{excl}} \tag{7.2}$$

should give a better estimation of the resolution. This is discussed in Ref. [18] and Ref. [37].

7.3 Resolution studies of data taken in July 2009 and comparison with simulation

In July 2009, the measurements were made with instrumentation only on the center module. The instrumented region of the module formed a cross as depicted in Fig. 4.18. Since the magnet could not be moved, measurements at different drift lengths were made by moving the TPC inside the magnet.

Since the magnetic field is sufficiently homogeneous only in the middle of the magnet, this limited the available drift lengths and the measurements were therefore only done with the beam at 70, 150, 220 and 300mm from the pad plane.

The data was taken using two different orientations of the pad plane. In the parallel configuration, which is the standard running configuration and the one used throughout this thesis, the pads were oriented with the long side of the pads parallel to the beam direction. In addition, data was taken with the TPC rotated 90 degrees so that the beam is directed perpendicular to the long side of the pads. The shape of the instrumented region allowed for measurements of tracks over the full length of the module also in this direction. In this way, a finer sampling of the energy loss of a track is obtained at the expense of spatial resolution. This was done in order to gain insight in the energy loss process of charged particles in the gas. A detailed simulation of the TPC was done in order to test predictions of the photo absorption ionization (PAI) model. This model includes atomic shell effects which will not show up in data taken with a large sampling length since the discrete energies of the shell effects are smeared out when electrons from several collisions are collected on one pad.

The TPC simulation was written in Lund (see Appendix A) and includes a low level simulation of the energy loss which incorporates the PAI model. A simulated electron undergoes a number of collisions with the TPC gas molecules, where the distance between the collisions is generated from the mean free path of the particle. At each collision point, the energy loss is generated from a distribution given by the PAI model. From this, the number of ionization electrons is calculated. The ionization electrons are then propagated to the readout structure, taking diffusion into account, and the gain in the GEM is modelled. The output of the simulation is of the same format as the measured data and was subsequently reconstructed using the same software (described in chapter 5).

To test the performance of the simulation, tracks in the parallell direction were simulated as well as in the perpendicular configuration. A comparison of experimental data and simulated data gives an appreciation of the performance of the simulation and gives confidence in the accuracy of the reconstruction. Comparisons between the simulation and data can be found in the following two sections and in Appendix A.

7.3.1 Resolution without magnetic field

For the runs without magnetic field in July 2009, in principle no distortion (see chapter 6)is expected. Thus, they should essentially be straight and it should be possible to use a straight line fit in the reconstruction of the tracks. The residual distributions integrated over the full length of the track, for no magnetic field runs at different drift distances are shown in Fig. 7.15.

In Fig. 7.16, the square of the resolution σ_y plotted against drift distance can be seen. Both data and simulation give a linear rise, which is expected, due to the diffusion. The data lies slightly above the simulated values. A probable explanation for this is that the distortion, although smaller than in the September 2010 data, has an effect after all which can be seen in Fig. 7.17. The effect is not present in the simulation which uses an idealized, perfectly homogeneous field. This would explain the slightly better performance of the simulation. All tracks have the same drift length in the amplification region, which means that there is a constant minimum broadening σ_0 of all clusters. For long enough drift lengths, the resolution dependence of the drift length is given by

$$\sigma^2 = \sigma_0^2 + \frac{D^2 \cdot z}{N_{eff}} \tag{7.3}$$

where D is the diffusion constant, z is the drift length and N_{eff} is the number of ionization electrons [18].

The best value is the one measured at 70mm, which is $\sigma_y = 139 \pm 3 \mu m$. A straight line fit to the measured points give a very optimistic value of the intrinsic resolution, i.e. the resolution without diffusion effects

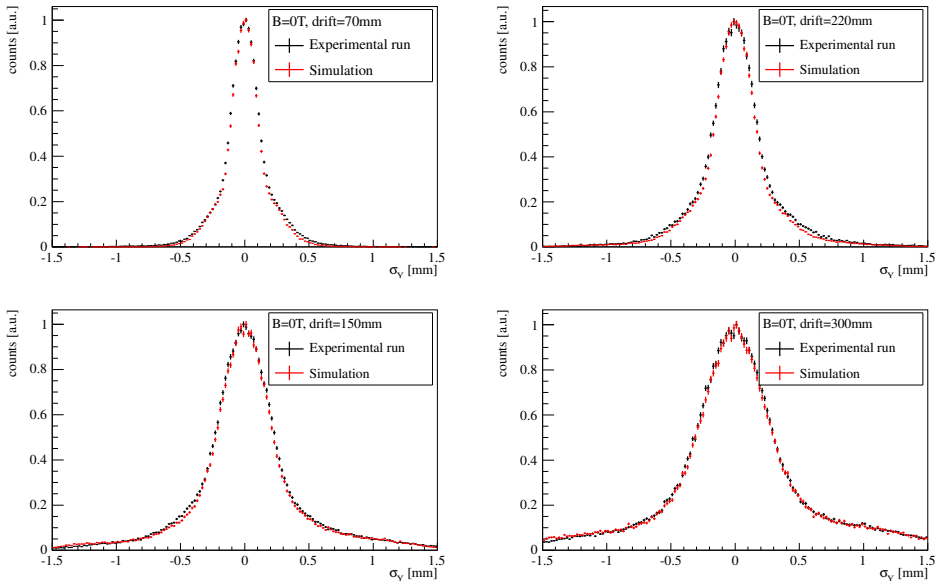

Figure 7.15: Residual distribution for four different runs with drift distances, from upper left to lower right, 70, 150, 200 and 300mm. The simulation compares well to data.

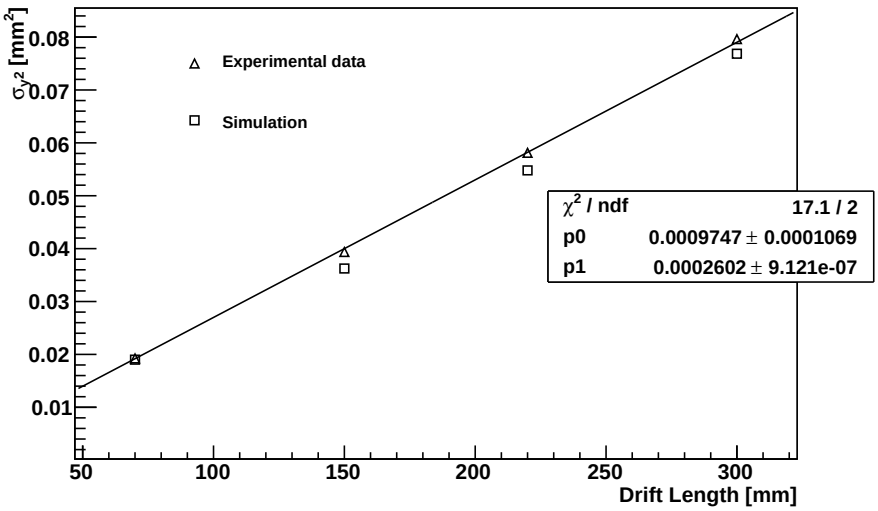

Figure 7.16: Resolution at B=0 plotted against drift length for simulation and data. The simulation performs slightly better. This is expected due to the clean environment and ideal electric field of the simulation. The fit has been made to the experimental data.

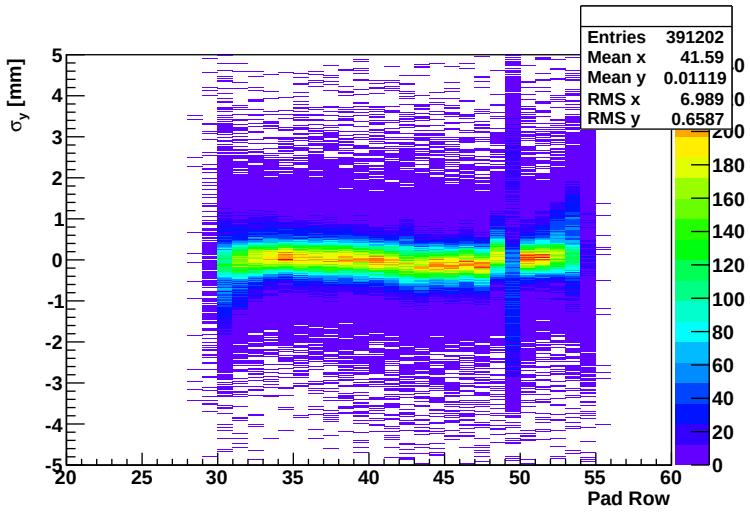

Figure 7.17: Residuals plotted against pad row for tracks with a drift distance of 300mm and no magnetic field. A slight distortion can be seen since the residuals are not centered around zero for all pad rows. 20,000 events were analyzed.

during drift (about 30 μm). However, when the width of the charge cloud becomes small enough, the finite pad size has an effect on the resolution since they are no longer small enough compared to the charge spread [18]. Thus, the resolution will become worse at shorter drift lengths for the same pad width.

7.3.2 Resolution with magnetic field

With magnetic field, a distortion is visible also in the July '09 data. This is visible mainly at the module edges and gives the image of the track a deformed shape compared to the helical shape it should have due to the magnetic field. This will make resolution studies difficult since they are based on a polynomial fit to the track. A residual based correction was therefore made. In the analysis, the outermost parts of the tracks (the five outermost pad rows at each end) were excluded since they should suffer most from the distortion. The x-coordinate of a cluster is limited by the length of a pad and thus the residuals in the y-direction can be calculated for each pad row. This will then provide an estimate of how large the distortion is in each row, as illustrated in Fig. 7.18. The effect is thus rather small but looking closer (Fig. 7.19) the effect is seen clearly. Around the reconstructed track, the residuals should have a gaussian distribution. Thus, the mean of the distribution in a single row can be used to correct the measured y-coordinates on a row by row-basis by simply subtracting the mean of the residual distribution in the corresponding row from the coordinates of the individual clusters in that row. By repeating this procedure a number of times, an image of the tracks that represents the original track better is obtained. The result can be seen in Fig. 7.21.

In the simulation, the distortion was taken into account by shifting the cluster y-coordinates to create a distortion. In Fig. 7.19, the residual distributions of clusters from real data are plotted against pad row. A fit was made to the mean of the distribution in each row as shown in the figure. Using the resulting function, the y-coordinates of the simulated clusters were shifted with the value of the fitted function in the pad row of the (simulated) cluster. Since the distortions vary significantly within the length of the pad, the displacement of the y-coordinate was chosen from the fit at a random point within the row. After the distortion was added, the simulated data was "corrected" in the same way as described above. As a result, the residual distributions of the simulation describes the data much better. In Fig. 7.20, a comparison between data and simulation can be seen for the four available drift lengths. Clearly, the simulation describes the data in a better way after the distortion has been added to the simulation. Since

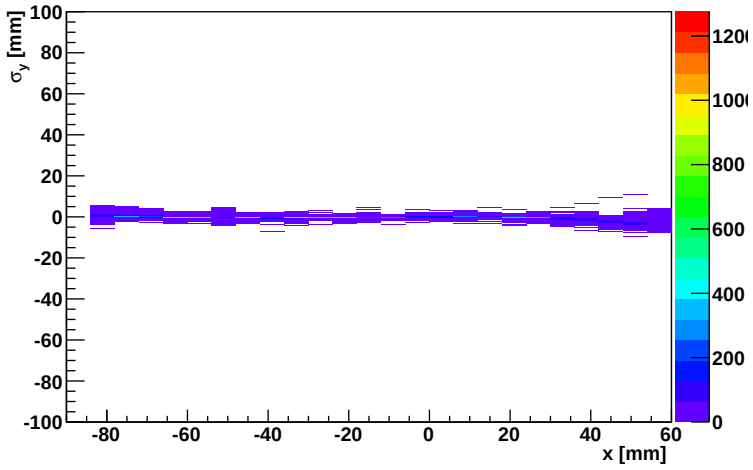

Figure 7.18: The residuals in y plotted against the x-coordinates of the clusters.

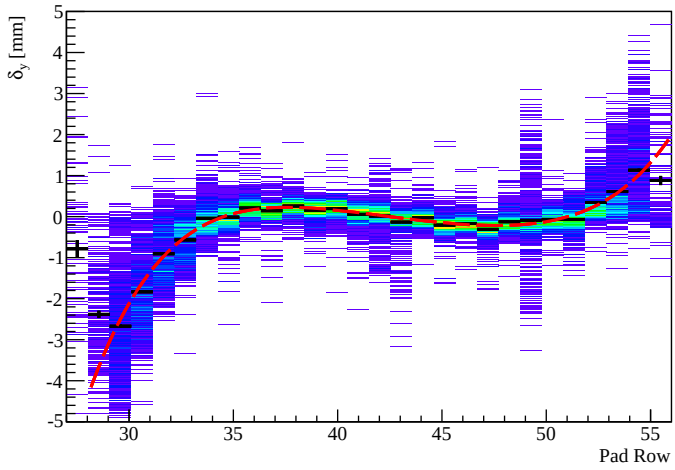

Figure 7.19: A simulation of the distortion was made fitting a function to means of the residual distributions (of clusters from real data) in each row. The function was then used to give the simulated clusters a distortion.

the simulated residuals are widened from this treatment, it can be assumed that the correction of the real data is not perfect. There is no knowledge of where along the pad length that the dominating part of the electron cloud was collected and the distortions can therefore not be fully corrected.

In Fig. 7.22, resolution is plotted for the different drift lengths for both data and simulation.

7.3.3 Drift direction resolution and comparison between the shaping times

Again, since no external reference point is available, the resolution is determined with respect to the reconstructed track. Since the magnetic field is parallell to the drift direction, the tracks should be straight lines in the xz-projection. However, when examined closely, the tracks seem to be slightly bent near the module edges. This is observed in runs with magnetic field and runs without but the effect is larger in magnetic field runs. The largest effect is near the module edges, which, in combination with

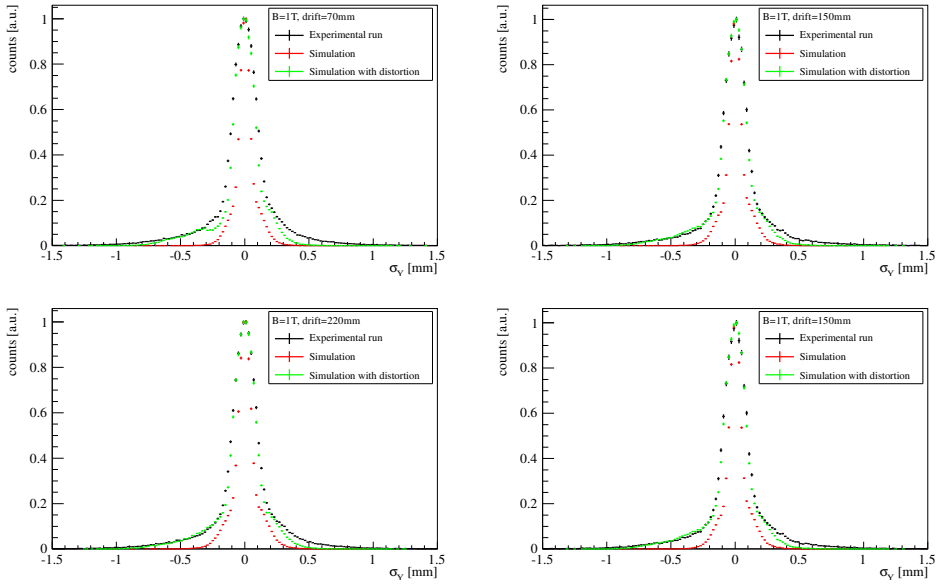

Figure 7.20: Residual distributions for four different runs with drift distances, from upper left to lower right, 70, 150, 200 and 300mm. The simulation compares well to data.

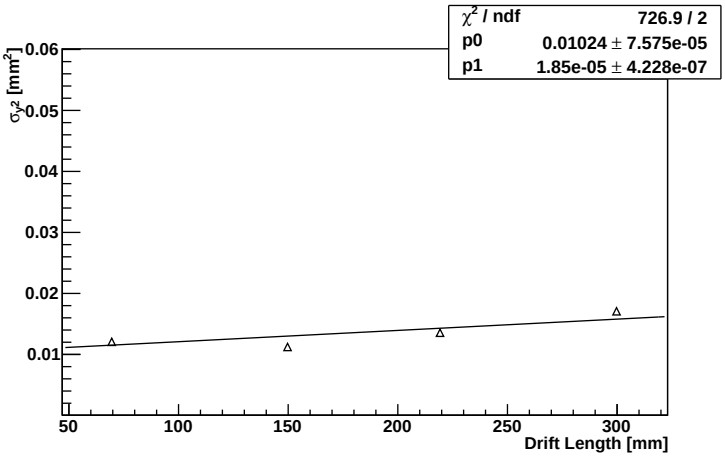

Figure 7.21: Resolution squared plotted against drift length for four runs using B = 1T.

the fact that the effect is larger with magnetic field, suggests that the electric field distortions have an effect on the drift time as well as distorting the coordinates in the transverse plane. Fig. 7.23 shows an example of a track in the xz-plane where this can be observed. In Fig. 7.24 the residual distributions row by row, for two different drift lengths (70mm and 300mm), can be seen. The fact that the deviations from the straight shape have about the same size, regardless of drift length, suggest that the distortion takes place in the GEM region. Fig. 7.25 shows a residual distribution from a run without magnetic field to indicate that the effect, although smaller, is also present without the magnetic field. Because of these edge effects, the analysis is again done on tracks where clusters from the five outermost layers of the module have been removed. Inside this cut, the effect is less severe but can still be seen. In Fig. 7.26 the residual distribution integrated over all clusters inside the cut can be seen. The bump on the right side is due to the remaining distortion of the track, which means that in order to get a good estimation of the resolution, the distortion has to be taken into account.

The fact that the residual distribution for each pad row is supposed to line up around 0 can be used for a simple correction of the cluster coordinates in the same way as described for the distorted coordinates

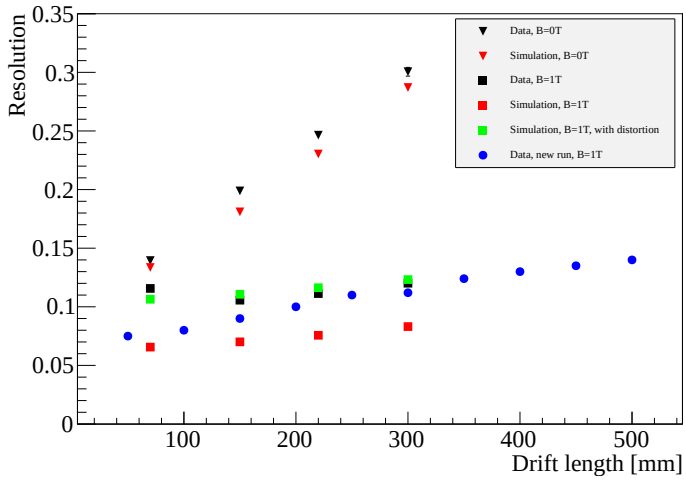

Figure 7.22: In this figure, all resolution measurements made in the parallell configuration for July'09 are included. Also included are measurements made by the Japanese group (in blue). The effect of adding the distortion to the data is seen here, as the data is described in a much better way after this. Note that the values are not squared in this figure.

in the bend plane. The result can be seen in Fig. 7.28 and Fig. 7.27.

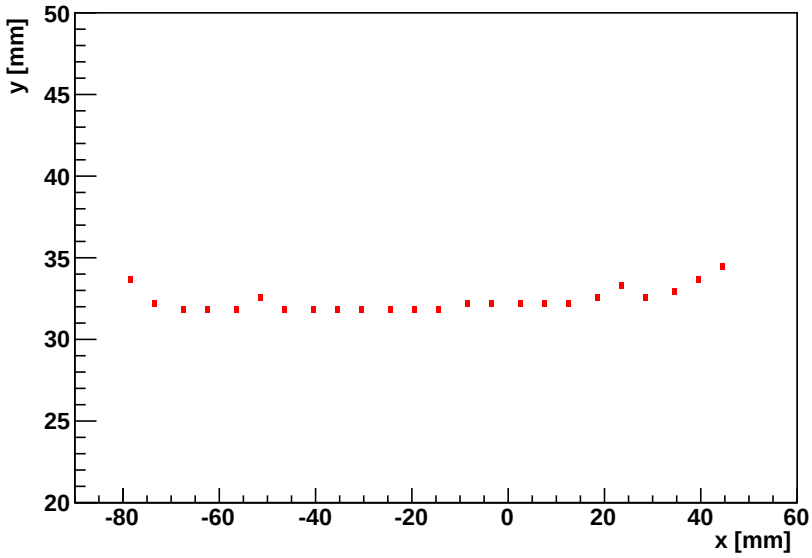

Figure 7.23: Typical projection of a track in the x-z-plane. In this scale, the distortion is clearly visible at the edges.

Resolution

The resolution in the drift direction should be influenced by both the shaping time and the sampling rate. A doubled sampling rate (from 20 to 40MHz) will mean that the amount of data to be stored is doubled so it is important to investigate if the design goals can be reached with the lower sampling rate. In Fig. 7.29, the measured resolution plotted against drift length can be seen. For all shaping times, a linear rise can be seen, which is consistent with the behaviour predicted by eq. 7.3. The resolution is

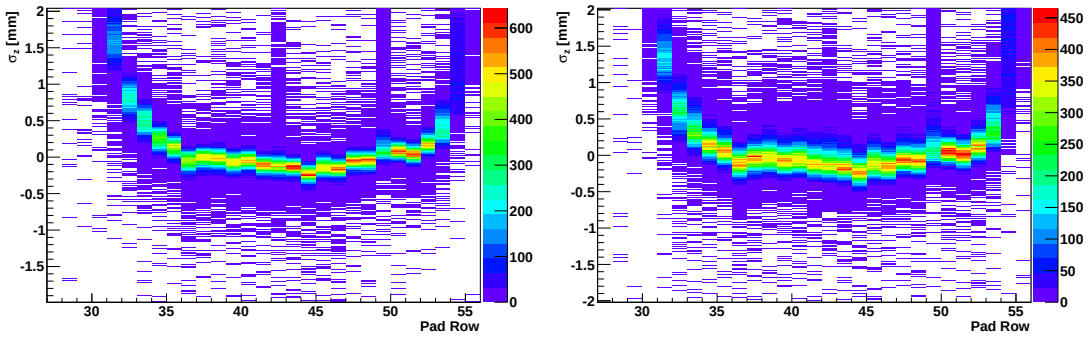

Figure 7.24: Residuals plotted against pad row. The left figure comes from a run with a drift length of 70mm while the right one comes from a drift length of 300mm. Both had a magnetic field of 1 T.

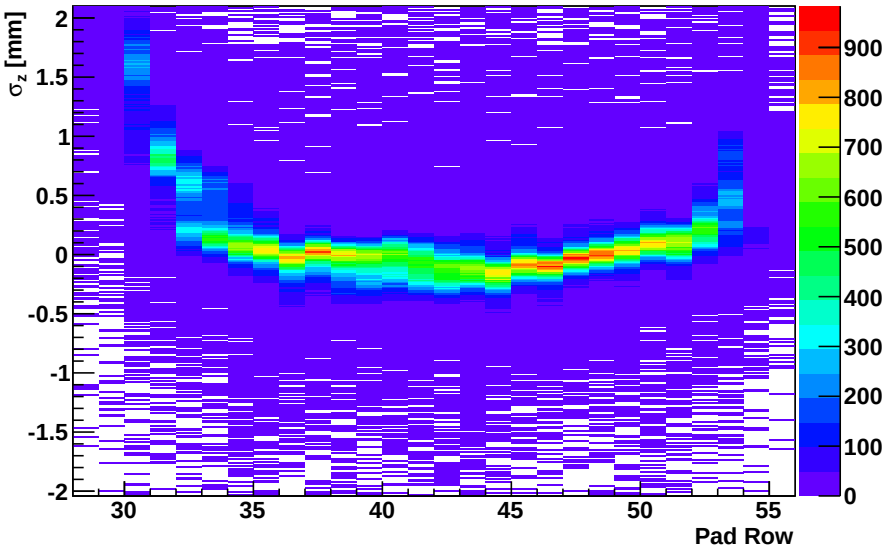

Figure 7.25: Residuals plotted against pad row for a run without magnetic field at a drift distance of 150mm.

improved with decreasing shaping time for 120, 90 and 60ns whereas it gets worse again for 30ns. This is not surprising since the pulse shape is small compared to the sampling rate for a peaking time of 30ns. To determine the arrival time with a better precision than the sampling interval, at least a few samples are required, whether the time is obtained through a fit or a weighted mean of the samples in the pulse. Therefore, the resolution should eventually get worse when the number of samples become too few. In Fig. 7.30, the resolution given in time samples is plotted against drift distance to show that it is significantly better than one time sample. The best point, at 70mm drift and shaping time of 60ns, has a resolution of $216 \pm 0.7\mu m$. A straight line fit to the best points of Fig. 7.29 (with a shaping time 60ns) gives an intrinsic resolution estimation of $\sigma_z(0) = 204 \pm 0.9\mu m$.

The design goal of the ILD TPC is a resolution in the drift direction of $\leq 500\mu m$. This is the value envisaged for half the drift length. Since the TPC is divided into two halfs, with the cathode in the middle and separate read out structures at each end, the half drift length is one quarter of the total length of the TPC (4.3m). Extrapolating the line to 1.075m gives a result of $\sigma_z(1.075) = 346 \pm 9\mu m$ which is well below the desired resolution.

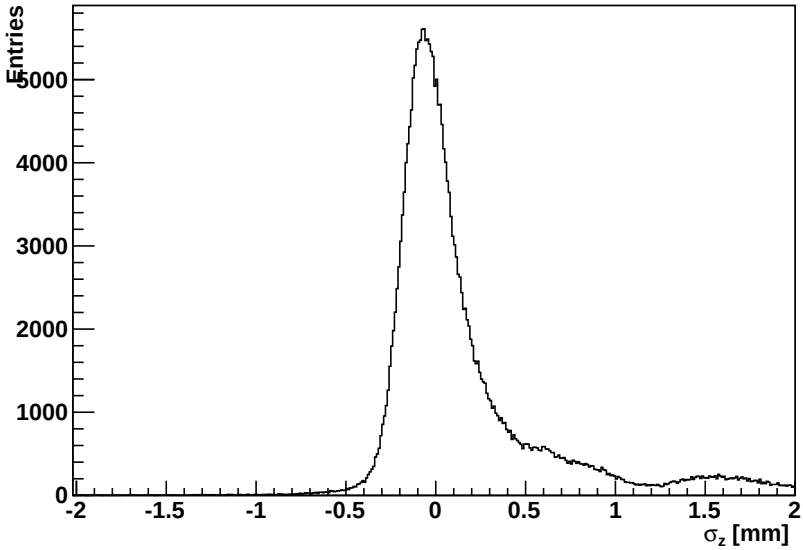

Figure 7.26: Z-residuals from a run with magnetic field and 70mm drift length. The bump on the positive side is due to the distortion.

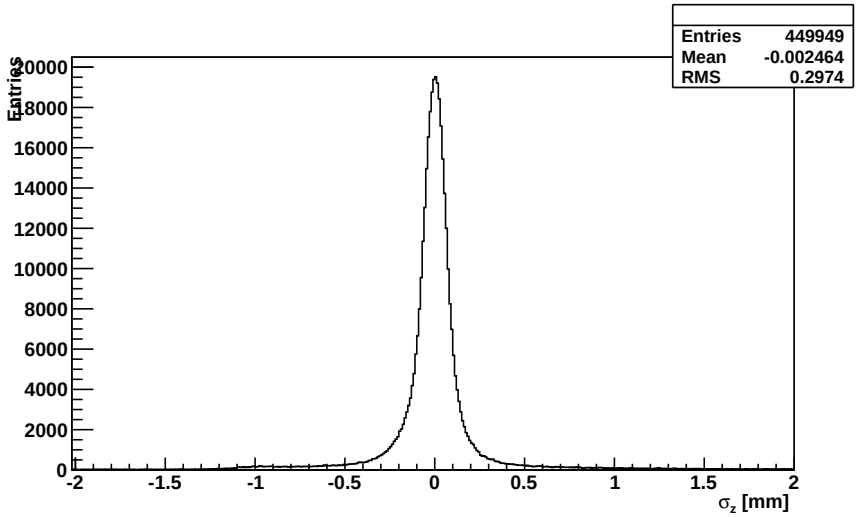

Figure 7.27: Z-residuals from a run with magnetic field and 70mm drift length. Now, the correction has been applied and the bump in Fig. 7.26 is no longer visible.

For later comparison with the data of September 2010, a fit was made also to the points with a shaping time of 120ns. The estimated value of the intrinsic resolution in this case is $\sigma_z(0) = 250 \pm 1\mu m$.

7.4 Results from September 2010

For the data recorded in September 2010, the alignment procedure described in chapter 6 was used to correct for the distortions and misalignments in the xy-plane. In addition to the runs made without magnetic field (used in the aligment procedure), a number of measurements were made using the nominal field of 1T. The measurements were made at different drift lengths, ranging from 50mm to 550mm with

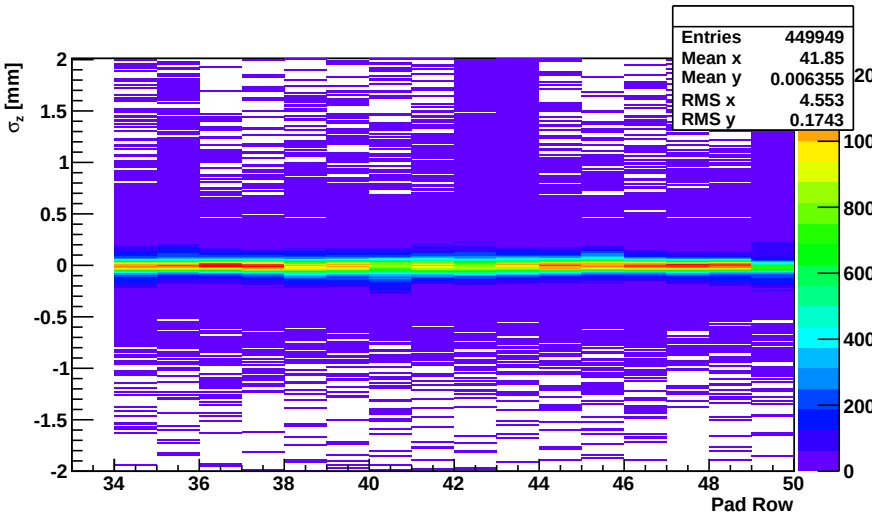

Figure 7.28: Z-residuals plotted against pad row for a run with magnetic field and a drift distance of 70mm. The correction makes the residuals line up around zero.

50mm intervals. This was possible thanks to the movable table which allowed the entire magnet to be moved and thus the TPC could be kept fixed in the region of the homogeneous magnetic field at all times.

This time, the number of readout channels was increased since more FECs were used compared to the measurements in July '09. A path was instrumented through three modules in order to measure tracks over the full radial length of the TPC. This has already been described in section 4.9 and the instrumented region and a typical event can be seen in Fig. 4.17.

7.4.1 Resolution in the drift direction

To get a good estimation of the resolution at a certain drift length, the angle of a track with respect to the xy-plane has to be as low as possible. Otherwise, the drift length for a cluster on one side of the chamber will differ from the drift length of a cluster on the other side of the chamber. The residual distribution would thus contain residuals from clusters of different drift lengths and therefore different widths of the charge clouds. The distribution of track angles can be seen in Fig. 7.31. As seen from the figure, the distribution of track angles is centered around zero. A gaussian fit gives a standard deviation of 0.0005 rad. Assuming that the peak in the distribution corresponds to the angular spread of the beam, making a cut on track angles larger than three standard deviations from the fit should exclude many of the tracks that have obtained a larger angle due to scattering along the path. These tracks will have a lower momentum and will be more prone to multiple scattering which will degrade the results of resolution measurements done in this way. For a typical track length of about 500mm, an angle of 0.0015 corresponds to a difference of about 0.7mm between clusters on each side of the track. This should be negligible compared to the spread of the beam which is about 2 cm. The drift velocity used to get the z-position of a cluster from the measured arrival time, has been measured several times, e.g. in [49]. The data used was taken with magnetic field. This has no effect on the drift in z however, since the magnetic field only reduces the diffusion perpendicular to the magnetic field. Therefore, the slope of the fitted line in Fig. 7.32 will be larger than for the corresponding plot of the residuals measured in the bend plane.

The measured residuals can be seen plotted against drift distance in Fig.7.32. A linear rise with increasing drift distance can be seen, even if some of the measurement points deviate from the line somewhat. The reason for this has not been fully investigated. If the intercept is interpreted as the intrinsic resolution, this gives $258.6 \pm 2\mu m$ which compares well to the value obtained in July '09 ($\sigma_z(0) = 250 \pm 1\mu m$). There

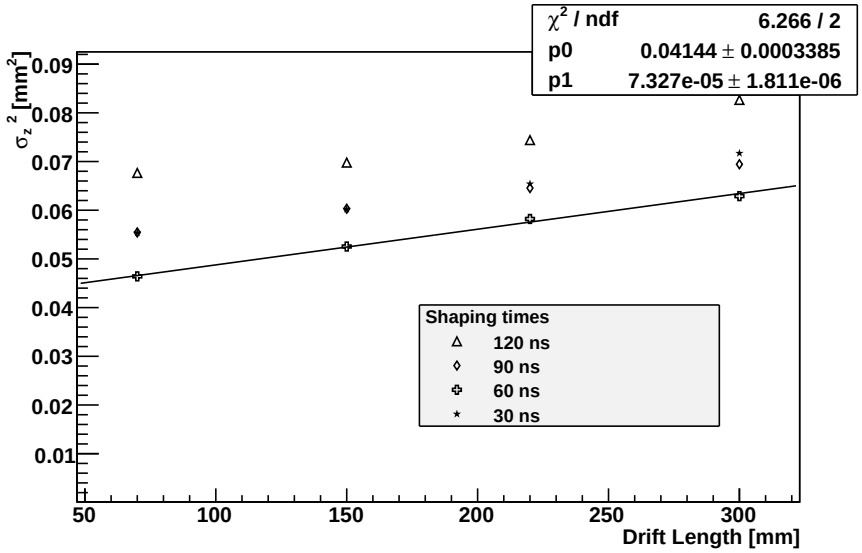

Figure 7.29: Squared z-resolution plotted against drift length for four different drift lengths and different shaping times.

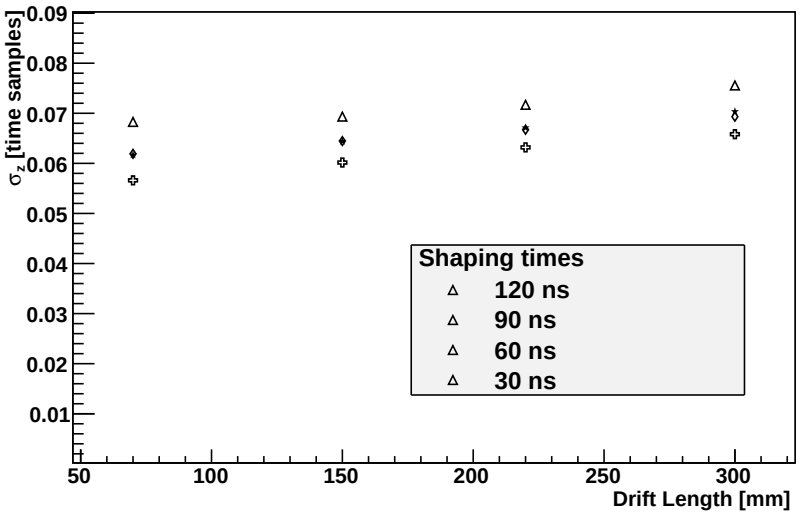

Figure 7.30: z-resolution, in time samples, plotted against drift length for four different drift lengths and different shaping times. Note that the values are not squared in this case.

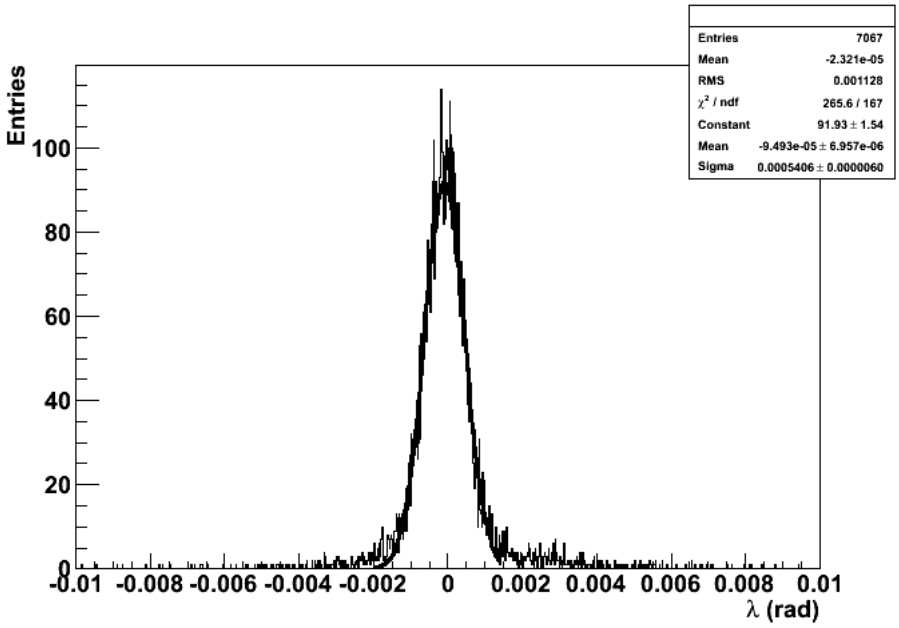

Figure 7.31: Distribution of track angles with respect to the xy-plane.

should be some room for improvement here. For example, the deviations from the expected straight line should be investigated. When extrapolating to half the drift distance of the ILD TPC, the result is $\sigma_z(1.075) = 465 \pm 13\mu m$ which meets the design demands.

7.4.2 Resolution in the bend plane

In fig. 7.33 resolution versus drift length, before and after the introduction of the corrections described in chapter 6, can be seen. The same cut on the end parts of the tracks, i.e. removing the outermost five rows on each side, as for the July '09 data has been used. As expected, the slope is smaller than in the drift direction (Fig. 7.32) since the diffusion is reduced due to the magnetic field. A significant improvement can be seen in the corrected data. The best resolution, $68 \pm 0.4\mu m$, is measured at a drift distance of 100mm. At short distance, a small rise can be seen. This is possibly due to the so called hodoscope effect, where the resolution starts degrading since the charge is no longer spread out enough over the pads. The same rise can be seen in the measurements from July '09. A fit to the data points gives an intrinsic resolution $\sigma_y(0) = 59 \pm 0.4\mu m$.

In the ILD TPC, a magnetic field of 3.5T will be used. This will give an even smaller slope than the one found here for 1T. A comparison between the theoretical curve in and the measurements at 1T in Fig. 7.34 (see also Fig. 4.11) shows that the data is slightly better than the calculation. Therefore it is reasonable to conclude that the design goal of a resolution better than $100\mu m$ would be reached with the Large Prototype in 3.5T since the 1T data in Fig. 7.33 shows a resolution that is slightly better than the one shown for 1T. It can also be noticed that the resolution for 4T (not 3.5T) is essentially constant as a function of drift distance, whereas at 1T the resolution is degrading with increasing drift length. Even if the degradation of the resolution at short drift distances is expected to have more significance for higher magnetic fields, since the charge clouds will generally be smaller due to the large magnetic field, the resolution should be well below $100\mu m$ up to at least half the maximum drift distance of 2.15m. It should be noted that the theoretical calculations in the figure were made using a range of somewhat different conditions than the ones used in the actual measurements in this thesis. For example, the calculations used a drift field of 250V/cm, a pad pitch of 1.27mm and a pad row pitch of 6.3mm. In the measurements, the drift field was 230 V/cm, the pad pitch about 1.2mm (slightly varying) and the row

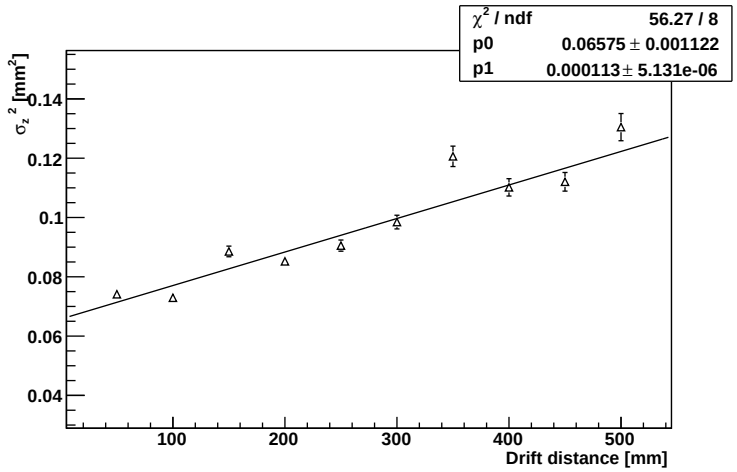

Figure 7.32: Squared resolution in the drift direction plotted against drift distance.

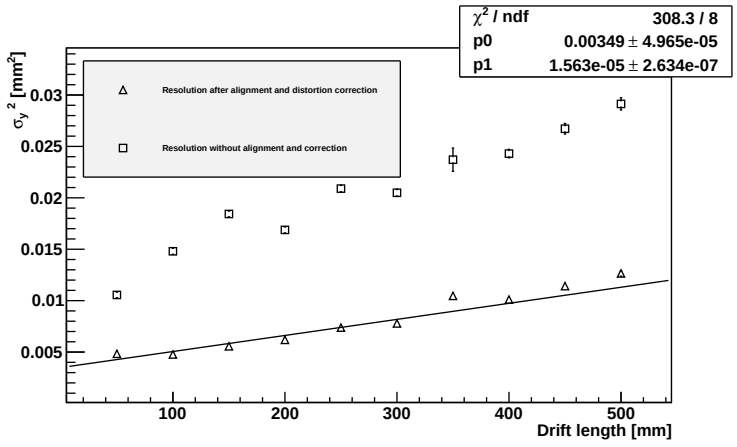

Figure 7.33: Bend plane resolution squared as a function of drift length. The situation before as well as after alignment and distortion correction is shown.

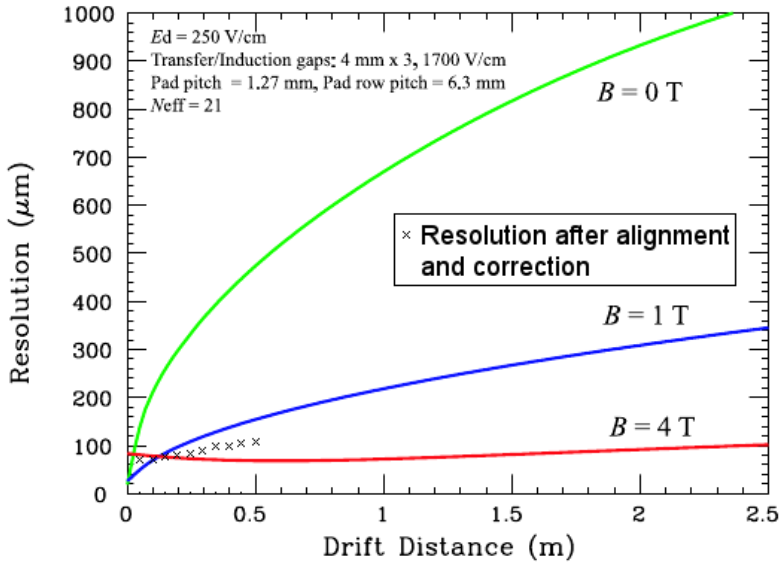

Figure 7.34: The measured resolution added to the plot from Fig. 4.11. The points show a better result than the one calculated for 1T.

pitch 5.26mm. Also, the values of the fields inside the GEM were different. Even though this means that the results are not directly comparable, it is obvious from the figure that the resolution for 3.5T will be significantly better than the one measured at 1T.

The track correction made is based on the assumption that the distortions do not vary significantly within a pad row. As already stated, the distortions however might vary also within a row. The effect of this has not been thoroughly investigated but it is reasonable to assume that the electrons are affected differently depending on where in the pad row they arrive. Electrons closer to the distortion source are therefore affected more. An investigation of what impact this has on the center of gravity of the cluster should be made. If a competely distortion free environment cannot be obtained, the results from such a study could be very useful to a future measurements. In any case, a measurement made with less or no distortions present should give better results. If an external detector was to be installed, e.g. the planned silicon detectors, alignment and distortion corrections would be greatly simplified since the position of the tracks could then be measured with greater accuracy. Thus, the alignment procedure would not have to rely only on data from the detector that is to be aligned.

7.5 Momentum measurements

A charged particle moving in a magnetic field $\mathbf{B}$ is subject to a Lorentz force according to $\mathbf{F} = \mathbf{q} \cdot \mathbf{v} \times \mathbf{B}$ where q is the charge and $\mathbf{v}$ is the velocity of the particle. In the plane perpendicular to the magnetic field, the particle will describe a circular trajectory since the force will be perpendicular to the velocity at all times. Since the centripetal acceleration a of a particle in a circular trajectory is given by $a = \frac{v^2}{R}$ the momentum can be obtained, using Newton's second law of motion $F = ma$, as $p = RqB$. With R in meters, q in units of elementary charge and B in Tesla, p can be written in GeV as:

$$p \approx 0.2998BqR. \tag{7.4}$$

Since all particles stable enough for momentum measurement in this way carry an electric charge of either +1 or -1, the equation becomes very simple.

If multiple scattering is ignored and the magnetic field is assumed to be perfectly homogeneous, the measured tracks should describe an arc of a circle. For a large circle, i.e. a high momentum track, the track can be approximated by a second degree polynomial [17]:

$$y = a + bx + cx^2. \tag{7.5}$$

Here, the parameter c is related to the radius of the circle by

$$c = \frac{1}{2R}. \tag{7.6}$$

Thus, the track momentum can be determined from this parameter, the magnetic field and the charge of the particle.

The momentum studies described here were made on the data from 2010 with corrections described in chapter 6. The momentum distribution from a run with a drift distance of 150mm can be seen in Fig. 7.35. The tail at lower momenta comes from particles that have undergone some kind of interaction between the beamline and the sensitive region of the detector, most probably in the detector walls or in the magnet. The spectrum has a clear peak slightly below the nominal value of 5GeV. A better alignment procedure could possibly improve this. Measurement points external to the TPC, e.g. obtained with the silicon detectors that were originally planned to surround the TPC, would not have been affected by the electric field distortions. Therefore, they would have been helpful in the alignment. Nevertheless, a reasonable estimate of the momentum resolution should still be attainable. A fit to the peak in 7.35 gives $\frac{\sigma_p}{p^2} = \sigma(\frac{1}{p}) = (9.19 \pm 0.18) \times 10^{-3}$ GeV^{-1}.

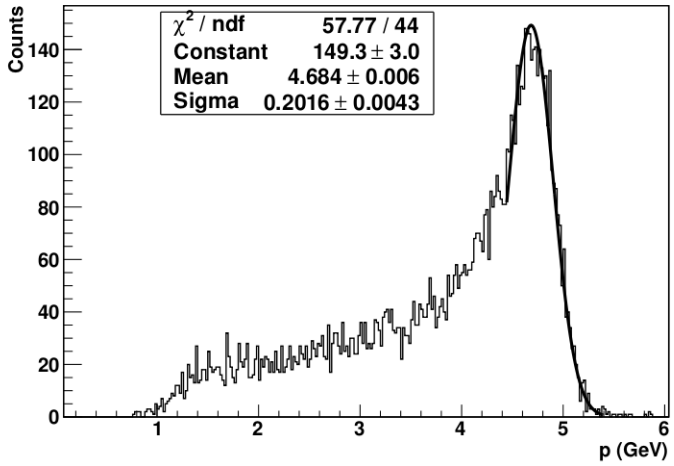

Figure 7.35: Momentum distribution from a run with a magnetic field of 1T and a drift distance of 150mm.

The measured value can be compared to what comes out from the Glückstern formula when inserting the parameters valid for the measurement, B = 1 T, N = 84 and L = 49 cm, together with the measured point resolution, at 15 cm drift length, of $\sigma_y(0) = 79$ μm, which then gives $\sigma(\frac{1}{p}) \approx 3 \times 10^{-3}$GeV^{-1}. This is a factor of about 3 better than directly measured.

However, the energy spread of the beam is about 5% [47], which results in $\sigma(\frac{1}{p}) \approx 10^{-2}$ at 5 GeV and thus fully accounts for the measured value. Consequently, the measured momentum resolution at the prototype TPC can not be used to obtain the final momentum resolution of the full size TPC by extracting a scaling factor using the Glückstern formula. Nevertheless, it is possible to get an estimate of whether the present measurements are consistent with the final goal by using Fig. 7.34. This figure shows the expected theoretical curves for space resolution as a function of drift distance at various magnetic fields. The theoretical curves are calculated for slightly different conditions compared to what was the

case for the measurements. Also included are the measured values at B = 1T over drift distances between 5 and 50 cm as comparison. As can be seen the measured values are somewhat better than the predictions except for the shortest drift distance, where one can suspect that the so called hodoscope effect becomes important. This behaviour can be understood from the smaller pad size in the measurements. The theoretical resolution curve for 4 T is almost flat as a function of drift length and corresponds to a resolution of around 60μm. It is realistic to assume that it will not be very different for 3.5 T. If now the foreseen parameters of the final TPC are inserted, B = 3.5 T, N = 224 (based on 5 mm long pads) and L = 130 cm, and assuming a point resolution of 60 μm, we get $\sigma(\frac{1}{p}) \approx 6 \times 10^{-5}$ GeV^{-1}, which is somewhat better than what is aimed for. This can be further improved by reducing the pad length to 4 mm but even more, as realized from the Glückstern formula, by increasing the track length. For a direct determination of the momentum resolution at the prototype TPC, independent measurements of the individual electron momenta are needed since the beam is not monoenergetic.

Chapter 8

Summary

Data from test measurements with a TPC with GEM readout have been analysed as part of research and development towards a tracking detector in a future linear collider. In addition, an alignment of the detector modules and correction of a distortion of the particle tracks has been made.

The TPC prototype used to obtain the data was constructed by the LCTPC collaboration and equipped with GEM modules made by the Asian TPC Group. The data were collected during July 2009 and September 2010. During the first measurement period, a support structure for a (not installed) gating GEM was exposed to the drift region which resulted in a distortion of the electric field that affected the drifting electrons. In the measurements of 2010, a field shaper was installed to rectify this. However, the mentioned faulty setting of the voltage for the field shaper meant that there was still a distortion present. The distortions made the drifting electrons deviate from their straight paths towards the pad plane, with the result that the original tracks were badly represented by the recorded track images.

The data from July 2009 was analysed with respect to energy loss in the chamber gas (see Appendix A) and compared to what was obtained from a simulation. The data was found to be in good agreement with the simulation, especially when no magnetic field was used. When the magnetic field was used, a good agreement could be reached when the distortions were included in the simulated data.

For the data of September 2010, an alignment algorithm based on the Millepede package was written and tested on a simple simulation where it performed well. The result was an estimated intrinsic resolution in the bend plane of $\sigma_y(0) = 59 \pm 0.4\mu m$. A comparison of the measured points to theoretical calculations, albeit made for slightly different parameters than the ones used in the measurement, gives reason to believe that the resolution for a magnetic field of 3.5T will be well below the required $100\mu m$.

From momentum measurements a resolution of $\sigma(\frac{1}{p_T}) \approx 10^{-2}$ GeV^{-1} was found, which is in accordance with the energy spread of the beam. An accurate measurement of the momentum resolution would require a high precision external reference detector, which enables momentum measurements of individual tracks.

In the drift direction, the shaping time of the incoming pulse was found to be important. The resolution improved with decreasing shaping time until the shaping time went below the time of a sampling interval. Thus, the best resolution was measured with a shaping time of 60ns whereas the resolution at 30ns was comparable to the resolution at 90ns. The worst resolution was measured at 120ns, the longest shaping time. The reason for the deterioration of the resolution at 30ns is probably that the shaping time is shorter than a sampling interval (which is 50ns at 20MHz) which means that there is not enough points for a good determination of the arrival time of the pulse. An increase in the sampling time could thus mean that an even better resolution would be reachable. At 60ns, an intrinsic resolution of $\sigma_z(0) = 204 \pm 0.9\mu m$ was measured. An extrapolation to half the drift length of the final TPC, 1.075m, gives an estimated resolution $\sigma_z(1.075) = 346 \pm 9\mu m$ which is well below the desired resolution of $500\mu m$.

The same extrapolation for a shaping time of 120ns gives a resolution $\sigma_z(1.075) = 0.465 \pm 0.013 \mu m$ which also fulfills the design requirements.

Acknowledgements

A large number of people helped, in big and small ways, to make this thesis possible. If anyone feels left out I assure you it was unintentional and beg your forgiveness.

First of all, I would like to thank my supervisors, Leif Jönsson and Anders Oskarsson, for invaluable support and help with analysis and writing. Thanks for continuous encouragement and patience. I would also like to thank Philippe Gros for always having time to answer stupid questions and helping with everything from debugging to telling me to write when I would rather do other things. I owe a great deal to Peter Christiansen for suggestions and help, both in getting me started and afterwards. Thanks also to Evert Stenlund for help with various statistics issues and of course the work on the pulse shape. Thanks to Ulf Mjörnmark for helping with various computer issues and teaching me the DAQ-software. Both Ulf and Evert contributed with valuable comments on the thesis. Ulf was also an invaluable help in exploring the cuisine of Hamburg. Thanks also to Björn Lundberg for help with the setup at DESY and to Bozena Wlosinska for always fixing things, even when I asked at the last minute. I am also grateful to Tuva Richert and Lene Bryngemark whose work I greatly benefited from.

I would also like to thank all the people at the Divison of Experimental High Energy Physics in Lund who were not directly involved in this work but nevertheless created a nice atmoshpere to work in. Thanks also to all members of the LCTPC collaboration and the people at DESY.

Last, but not least, I want to thank my parents, Kerstin and Erling, my brother Henrik, my sister Sara and of course my girlfriend Elin. Thanks for all the love and support.

Bibliography

[1] P. Priyadarshi "Zero is not the Only Story", 2007, ISBN 8189072145

[2] G. Kane "Modern Experimental Particle Physics", 1993, ISBN 0-201-62460-5

[3] G. Aarons *et al.* [ILC Collaboration], arXiv:0709.1893 [hep-ph].

[4] T. Li and W. Chao, Nucl. Phys. B **843**, 396 (2011) [arXiv:1004.0296 [hep-ph]].

[5] "The Compact Linear Collider Study" http://clic-study.web.cern.ch/

[6] "International Linear Collider" www.linearcollider.org

[7] J. Brau *et al.*, "International Linear Collider reference design report. 1: Executive summary. 2: Physics at the ILC. 3: Accelerator. 4: Detectors,"

[8] T. (.). Behnke *et al.* [ILC Collaboration], arXiv:0712.2356 [physics.ins-det].

[9] K. Desch, J. L. Hewett, A. Miyamoto, Y. Okada, M. Oreglia, G. Weiglein and S. Yamashita, arXiv:hep-ph/0411159.

[10] K. Nakamura *et al.* [Particle Data Group], J. Phys. G **37**, 075021 (2010).

[11] T. Abe *et al.* [ILD Concept Group - Linear Collider Collaboration], arXiv:1006.3396 [hep-ex].

[12] "TPC R&D for an ILC Detector", LC-DET-2007-005

[13] R. L. Gluckstern, Nucl. Instrum. Meth. **24**, 381 (1963).

[14] Website of the LCTPC collaboration, www.lctpc.org

[15] W. R. Leo, "TECHNIQUES FOR NUCLEAR AND PARTICLE PHYSICS EXPERIMENTS: A HOW TO APPROACH," *Berlin, Germany: Springer (1987) 368 p*

[16] U. Fano "On the theory of ionization yield of radiations in different substances", Phys. Rev. Vol 70 (1946)

[17] W. Blum, L. Rolandi and W. Riegler, "Particle detection with drift chambers," ISBN-13-9783540766834;

[18] D. C. Arogancia *et al.*, Nucl. Instrum. Meth. A **602** (2009) 403 [arXiv:0705.2210 [physics.ins-det]].

[19] K. Ackermann *et al.*, Nucl. Instrum. Meth. A **623**, 141 (2010) [arXiv:0905.2655 [physics.ins-det]].

[20] F. Sauli 1996 Nucl. Instrum. Meth. A **386**, 531 (1997)

[21] "Research with Lepton Colliders" http://www-flc.desy.de

[22] T. Behnke, K. Dehmelt, R. Diener, L. Hallermann, T. Matsuda, V. Prahl and P. Schade, JINST **5**, P10011 (2010) [arXiv:1006.3220 [physics.ins-det]].

[23] L. Hallermann and P. Schade, *In the Proceedings of 2007 International Linear Collider Workshop (LCWS07 and ILC07), Hamburg, Germany, 30 May - 3 Jun 2007, pp TRK29.*

[24] K. Dehmelt for the LCTPC collaboration, "Status of the Large TPC Prototype 2008" EUDET-Memo-2008-46

[25] T. Behnke et.al. "Status and Plans of the Large TPC Prototype for the ILC". EUDET-Memo-2007-37

[26] Cornell University website, http://w4.lns.cornell.edu

[27] A. Ishikawa et.al. "A GEM TPC END Panel Pre-Prototype", arXiv:0710.0205v1 [physics.ins-det]

[28] A. Sugiyama, private communication

[29] T.Matsuda "Beam Test Results of a GEM Large TPC Prototype Readout by New Altro Electronics", talk given in June 2009 at the 1st International Conference on Micro Pattern Gaseous Detectors

[30] T. Lux [T2K Collaboration], J. Phys. Conf. Ser. **65**, 012018 (2007).

[31] LC-TPC collaboration, T. Matsuda et al. 2010 Results of the first beam test of a GEM TPC large prototype, JINST 5 P01010

[32] Alice TPC Electronics Charge Sensitive Shaping Amplifier (PASA) Technical Specifications

[33] ALICE TPC Readout Chip User Manual, 2002

[34] L.Jönsson, U.Mjörnmark "Front-end electronics and data acquisition for the LCTPC" EUDET-Memo-2007-53:

[35] V. Blobel "Linear Least Squares Fits with a Large Number of Parameter", Institut Für Experimentalphysik Universität Hamburg, 2000, www.desy.de/ blobel/

[36] M. Mager & L. Musa "Characterization of the PCA16", Presentation given at CERN in July 2008

[37] R. K. Carnegie, M. S. Dixit, J. Dubeau, D. Karlen, J. P. Martin, H. Mes and K. Sachs, Nucl. Instrum. Meth. A **538**, 372 (2005) [arXiv:physics/0402054].

[38] Pictures courtesy of Ulf Mjörnmark

[39] B. R. Martin & G. Shaw, Particle Physics second edition, 1997, ISBN 0-471-97285-1

[40] D. Attie, Nucl. Instrum. Meth. A **598** (2009) 89.

[41] SLAC website [www2.slac.stanford.edu]

[42] F. Sauli, "GEM READOUT OF THE TIME PROJECTION CHAMBER" CERN-EP -TA1 Internal Report, July 29, 1999

[43] K. Dehmelt for the LCTPC collaboration, "TPC Task Status Report 2009" EUDET-Memo-2009-09

[44] L.Jönsson, U.Mjörnmark "Front-end electronics and data acquisition for the LCTPC", EUDET-Memo-2007-53

[45] C. Gonzales et.al. "The ALICE TPC ReadOut Control Unit" 2005 IEEE Nuclear Science Symposium Conference Record

[46] K. Ackermann et.al. Nucl. Instrum. Meth. A **623**, 141 (2010)

[47] DESY test beam website http://adweb.desy.de/home/testbeam/WWW/Description.html

[48] P. Schade, "Development and Construction of a Large TPC Prototype for the ILC", Dissertation, Hamburg 2009

[49] L. Bryngemark, "Results from in-beam test runs of a GEM based TPC prototype-noise studies and position resolution in the time direction", EUDET-Memo-2010-32

[50] T.Richert "Analysis of the Gas Electron Multiplier readout system for the International Linear Collider Time Projection Chamber prototype at DESY", EUDET-Memo-2010-31

Appendix A

EUDET-Memo-2010-36

EUDET-Memo-2010-36

Particle tracking and energy loss measurements with the LCTPC: A comparison to simulation models

P. Christiansen, P. Gros, L. Jönsson, M. Ljunggren, B. Lundberg, U. Mjörnmark,

A. Oskarsson, E. Stenlund, L. Österman

Lund University, Lund, Sweden

K. Fujii, R. Yonamine

KEK, IPNS, Tsukuba, Japan

20.12.2010

Abstract

The large prototype TPC (LCTPC), instrumented with GEM readout and front-end electronics based on the ALICE ALTRO chip was tested at the DESY T24 electron beam. Data was collected with and without an external magnetic field of 1T, and in both the standard configuration where the tracks are along the long edge (5.2 mm) of the pads and in a perpendicular configuration where the tracks are along the short edge (1.2 mm) of the pads. For electrons with momentum $p = 5$ GeV/c the straggling function (charge distribution), the specific energy loss (dE/dx), and the spatial resolution was extracted and compared to simulations based on GEANT4 energy loss calculations.

The specific energy loss resolution was in general found to be better in the simulation than in the data, due to a narrower straggling function, raising questions about the energy loss modelling of shell effects.

The spatial resolution was found to be well described by the simulations when there was no magnetic field. For magnetic field runs the large $E \times B$ effect due to inhomogeneities in the electric field, caused by the support structure of the GEMs, is found to deteriorate the resolution from 70 μm to 100 μm even when an average correction is applied. This suggests that a redesign of the GEMs would significantly improve the spatial resolution.

1 Introduction

A possible TPC for the ILC has strict performance requirements based on the requirement for the Higgs mass to be determined from the Higgs strahlung processes. The requirement on transverse momentum resolution corresponds to a spatial resolution of better than 100 μm at the magnetic field of 4 T.

A broad test beam programs has been carried out within the EUDET framework using a large prototype TPC (LCTPC) with different readout technologies.

In the study presented here the main focus has been on comparing the performance obtained in the test beam measurements to the performance expected from state of the art simulations based on GEANT4 energy loss calculations. The goal of this study is primarily to understand if the performance of the LCTPC is optimal or if it can be further improved, but secondarily it addresses the physics question of to what precision the performance can be simulated.

The note is organised as follows. In section 2-6 the test setup and the detector is described in detail. In section 7-11 the simulation, data analysis, and results are presented. Finally the conclusions of this study are given in section 12.

2 The test beam

The measurements were performed at the test beam T24 from the DESY II electron synchrotron [1]. The circulating bunches of electrons are guided towards an internal carbon fibre target to produce bremsstrahlung photons in the energy range up to 7 GeV. The so produced photons are forced to hit an external metal plate to generate electron-positron pairs. Behind the conversion target a dipole magnet causes the electrons and positrons to spread out in the horizontal plane according to their momenta. A collimator cuts out a narrow momentum slice of particles which pass through the collimator. Thus by setting the magnetic field strength, particles with a certain momentum can be selected whereas the energy spread of the electron beam is given by the opening slit of the collimator. A schematic picture of the set-up is shown in Fig. 1.

A telescope of four 3x3 cm^2 scintillators with a thickness of 3 mm, organised in overlapping pairs at a distance of $\sim$ 100 cm between the pairs, provide a beam trigger [2] in a fourfold coincidence.

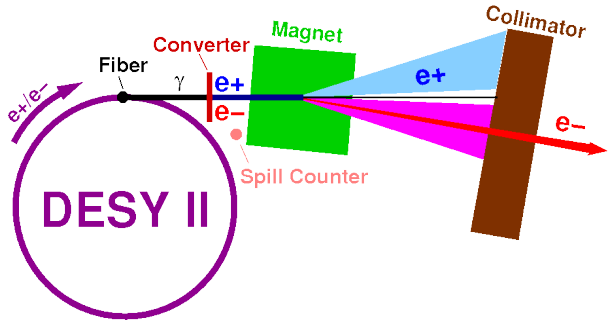

Figure 1: A schematic view of the test beam set-up

3 The large prototype TPC

3.1 The field cage

The large prototype TPC (LPTPC) [3, 4, 5, 6] consists of a cylindrical field cage and two end caps of which the anode side can be instrumented with various readout systems and the other end contains the cathode. Thus, it is essentially half a normal TPC. The inner diameter of the field cage is 730 mm and is limited by the core of the superconducting magnet (PCMAG) in which it is housed. The length is limited to 600 mm by the homogeneity of the magnetic field, which should not vary more than 3% over the length of the drift space. The field cage is constructed out of composite material. The cylinder is made of a 23.5 mm thick aramid honeycomb wall, which is glued between two layers of glass-fibre reinforced plastic (GRP) and a polymide layer for electrical insulation. This structure provides the necessary stiffness to prevent significant deformations and presents a minimum of material ($\sim 1\%$ of X_o) with which the particles may interact. The field cage should be able to stand an overpressure from the drift gas of up to 10 $mbar$. The inhomogeneity of the drift field should not exceed 10^{-4} over the drift volume and in order to meet this requirement the electrical field is provided by a series of field strips on decreasing potential from the anode to the cathode. These are 35 μm thick copper strips on both sides of a 75 μm thick kapton foil, which is glued to the inside of the field cage. The copper strips on the outside are so called mirror strips which are placed to cover the gaps between the field strips, overlapping half a strip width with the inner field strips and are on intermediate potentials. This arrangement of strips provides a homogeneous field to the order which is required. The strips are connected via a resistor chain which distributes the voltage along the drift length with the last strip (counted from the anode) on the same potential as the cathode. The potential of the cathode is about -14.5 kV giving a drift field of 230 V/cm. A schematic view of the field cage and a cross section of the cylinder wall is shown in Fig. 2.

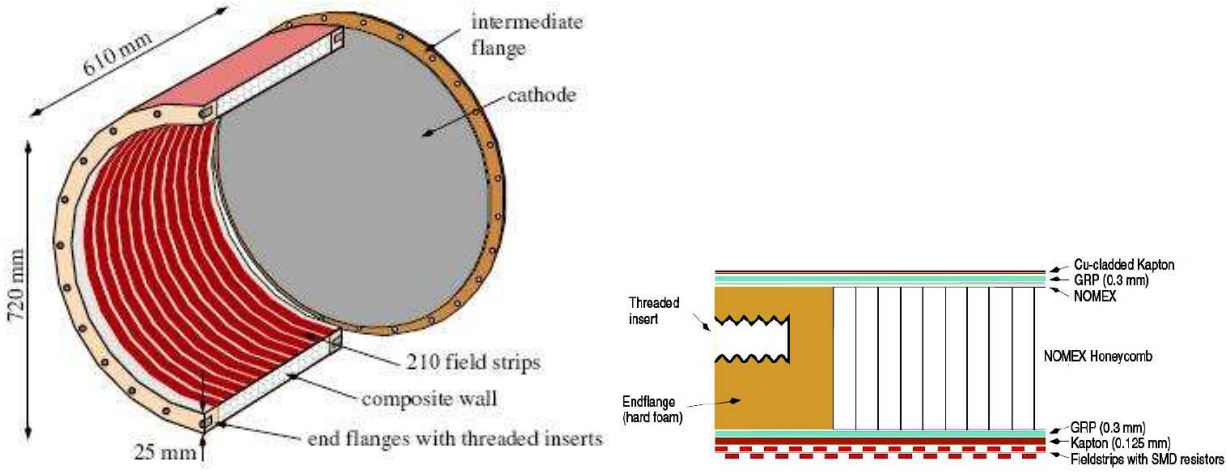

Figure 2: Left side: A schematic drawing of the field cage. Right side: A cross section of the chamber wall.

3.2 The end plate

The anode end plate is made from aluminium and the design is such that it should be able to accommodate seven gas amplification modules arranged in a way that corresponds to a subsection of the full scale TPC for the ILC. The accuracy for the insertion of the modules is better than 50 μm. A picture of the end plate is shown in Fig. 3.

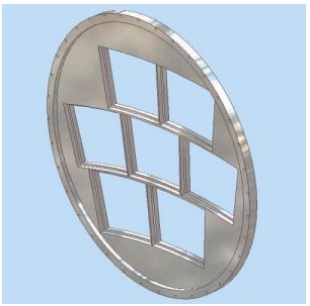

Figure 3: The end plate with the seven mounting positions for the readout chambers

4 The GEMs and pad plane

For this measurement, readout chambers based on gas electron multipliers (GEMs) developed by the Asian groups [7, 8] were used and 3200 pads were equipped with the ALTRO readout electronics. The GEM module has a keystone shape with the width of about 23 cm and the height of about 17 cm. The pad board has 5152 pads in total, arranged in 28 rows of about 1 mm wide pads separated by 0.1 mm. The length of the pads is 5.26 mm. The innermost 14 rows have 176 pads/row whereas the outermost 14 rows have 192 pads/row. Due to the shape of the module the width of the pads is increasing with its radial position so that the pad width varies between 1.15 mm and 1.25 mm. The pads of neighbouring rows are staggered with respect to each other by half a pad width. A picture of the pad plane is seen to the right of Fig. 4.

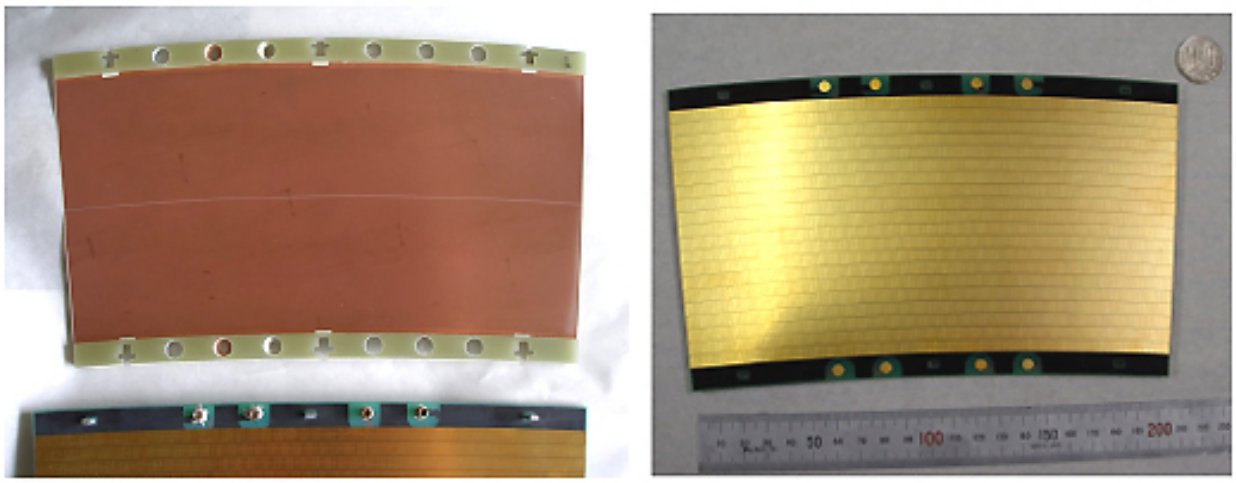

Figure 4: Left side: A GEM plane. Right side: The pad plane. The holes are for support pillars and HV supply.

The GEM modules have two copper layers of 5 μm on each side of a 100 μm thick liquid crystal polymer insulator. The holes are 70 μm in diameter and the pitch between the holes is 140 μm. A picture of a GEM plane is shown to the left of Fig. 4. The GEM system included two layers of GEMs in this test. The GEM foils are supported by two thin G10 frames along the long sides of the pad board and the GEM, respectively. The short sides have no support, which minimises dead regions between the GEMs in the ϕ direction. The distance between the two GEM foils (the transfer gap) and the distance between the last GEM and the pad plane (the induction gap) is 4 mm and 2 mm, respectively.

Since the short sides of the GEM foil have no support, metallic pillars were glued onto the long sides of the pad board, the purpose of which is to keep the GEM foils stretched and in position. Thus,

in the GEM foils and the G10 frames there are corresponding holes into which the pillars fit. An assembled module is shown in Fig. 5. A thin gating GEM was planned to prevent ions to drift back into the drift volume but was not installed at the time of the measurement. The voltage across the thick GEMs was 350 V giving a gas amplification of 10^4 for the double GEM system.

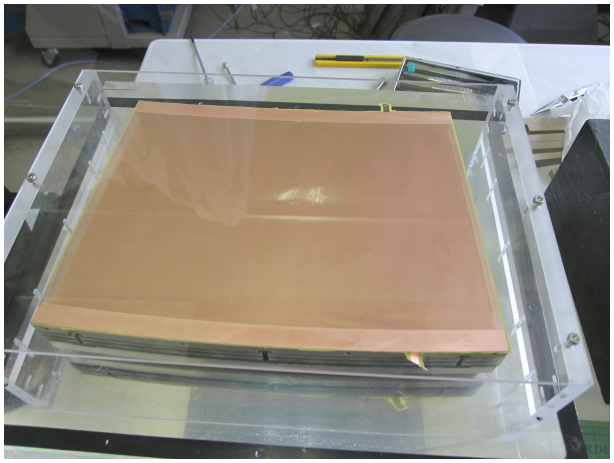

Figure 5: The assembled GEM module

The outermost GEM plane has to be on the same potential as the corresponding strip on that level in order not to cause any inhomogeneities in the drift field. For the Asian GEM module the outermost GEM should have been the gating grid on the level of the seventh strip in the field cage. However, due to the missing gating GEM this had to be accounted for in setting the potentials.

Unfortunately, since the gating grid was never introduced for this measurement, the metallic support pillars were sticking out unshielded, causing deformations of the electric field. This caused a straight track to become bent, where the magnitude of deformation depends on the distance of the track from the pillars. An example of such a reconstructed track is given in Fig. 9.

5 The superconducting magnet

The superconducting magnet (PCMAG) [9], which houses the LCTPC, was constructed by Japanese groups originally for the BESS-Polar balloon experiment to study cosmic anti-matter and has therefore a coil of low mass and no return yoke. A technical drawing of the magnet, with the position of the TPC indicated, is shown in Fig. 6.

The diameter of the magnet core is 85 cm and the length inside the magnet, with this diameter, is about 130 cm. The magnet can provide a field of 1.2 T but was in this measurement run at 1 T. The field is, however, not homogeneous over the full length of the magnet due to the non existing return yoke. Only in a region of ± 30 cm around the centre it is homogeneous to within 3% and this limits the length of the TPC to about 60 cm.

The PCMAG was at the time of these measurement sitting in a fixed position with the beam entering in the centre of the magnetic field so that the influence of the inhomogeneous regions of the field should have a small influence. The only way to measure at different drift lengths was to move the TPC inside the magnet. This is not causing any problems as long as the TPC is pushed further in to the magnet, corresponding to shorter drift lengths, but when the TPC is pulled further out the readout system is entering into the regions of inhomogeneous fields more and more. These measurements were performed at drift lengths in the range of 70 to 300 mm.

6 The readout electronics

The readout system for the LCTPC is based on the ALTRO chip [10], originally developed for the ALICE experiment at the LHC. The 16 channel ALTRO chip performs analogue to digital conversion with 10 bit precision followed by various steps of digital signal processing, including zero suppression and storage in an event buffer. The sampling can be clocked at frequencies up to 40 MHz so in principle sampling at this frequency and frequencies lower by multiples of two is possible. However, at 40 MHz sampling the full resolution is not maintained for the standard ALTRO chip. A limited number of ALTRO chips were modified to allow sampling at 40 MHz with almost full precision [11]. Up to now the system has been operated during data taking at 20 MHz only. The ALTRO chip has an event storage memory of 1 k 10-bit words, which corresponds to sampled data over a depth of 50 μs drift time at 20 MHz sampling frequency. The so called T2K gas mixture (95/3/2 % Ar/CF_4/Isobutan) was used in the TPC, which gives a drift velocity of around 7 cm/μs at a drift field of 230 V/cm. This leads to a maximum drift length of 350 cm that can be accommodated in the ALTRO memory i.e. much longer than the total length of the LCTPC of 60 cm.

In order to test recent technologies for gas amplification (GEMs and Micromegas for TPC readout) a new charge sensitive preamp-shaper has been developed. The programmable PCA16 chip [12] has, as the name indicates, 16 channels and offers different choices with respect to shaping time, gain, decay time and signal polarity. The new analogue chip required modifications to the Front End Card (FEC), compared to its original design for the ALICE TPC. These are mainly related to the programmability of the PCA16 chip which is done remotely. Data for setting the parameter values are downloaded to the board controller FPGA on the FEC via the data bus on the back plane. An 8-bit shift register delivers the digital input to set the peaking time, the gain, the polarity (common to the 8 PCA16 on a FEC) and it also provides a possibility to bypass the shaping function. An octal DAC (Digital to Analogue Converter) controls the decay time of the preamplifier. The various options will make it possible to find the optimal parameter setting for a certain gas amplification system so that the specifications for the final chip production can be quantified.

Each FEC contains 128 channels i.e. 8 PCA16 chips and 8 ALTRO chips are mounted on each

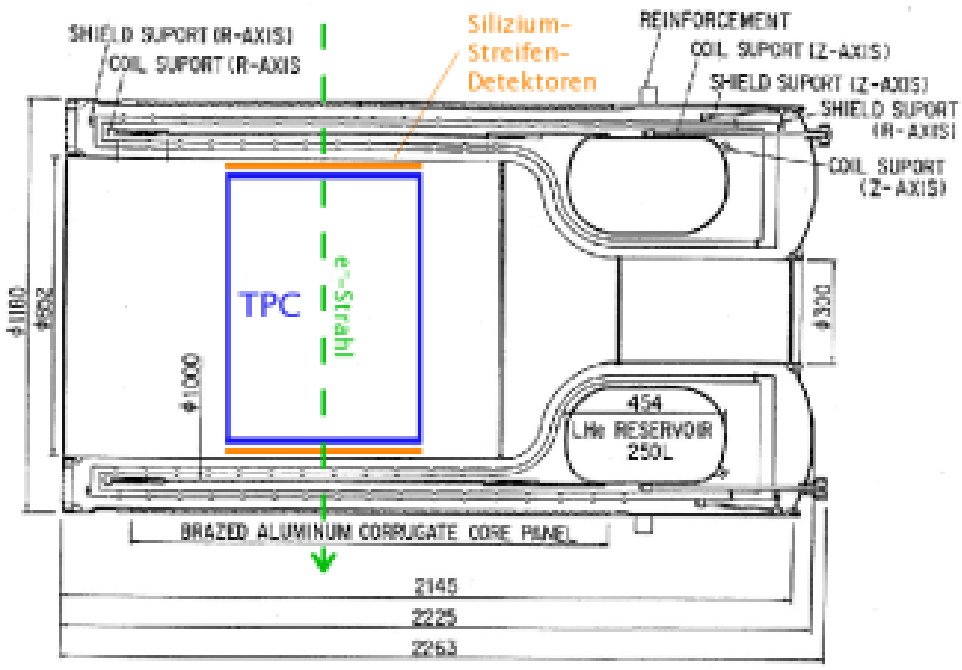

Figure 6: A technical drawing of the superconducting magnet (PCMAG) with the TPC indicated

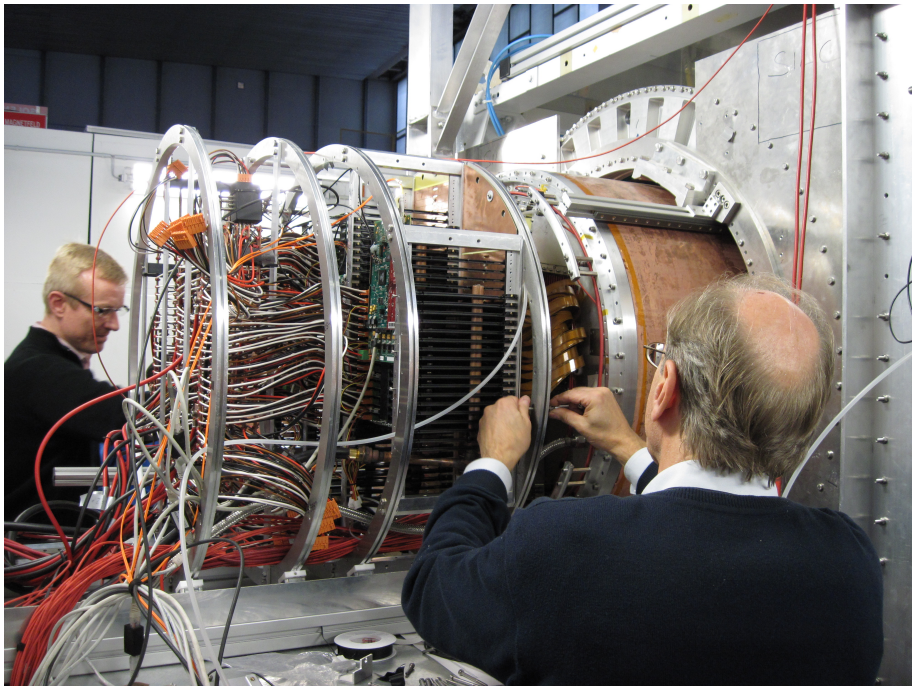

Figure 7: The front end electronics and its support structure attached to the TPC. Also seen are the optical cables for the data readout and the LV supply cables.

board. They are connected to the pad board on the TPC via flexible 30 *cm* long kapton cables. A Readout Control Unit (RCU) [13] governs the readout of the data via the back-plane to which a maximum of 32 FECs can be inserted. Data are sent via an optical cable to a Detector Read-Out Receiver Card (DRORC), which is placed in the Data Acquisition (DAQ) PC. The DAQ software uses the ALICE drivers and libraries for communication between the DRORC and the front end electronics via the optical link. At the reception of the trigger the ALTRO starts storing digitised information in the event buffer, up to a predefined number of samples. The RCU reads the ALTRO event buffer and sends the data on the optical link to the DRORC, which stores it in the memory of the readout computer. The events are stored on a local disk, a fraction of the events are sent to a monitoring program. A photograph of the test beam set-up is shown in Fig. 7.

The electronics pedestal and noise levels for all readout channels have been measured both initially as well as on a regular basis during data taking periods, mainly for pedestal subtraction and to check whether there are corrupt channels. The front end electronics has shown excellent noise performance. with a noise level of 0.5 ADC counts corresponding to an equivalent noise of 260 electrons for the longest shaping time and the lowest gain, where the noise includes random noise, coherent clock noise and long term variations on the scale of seconds. If the gain is increased to the highest value (27 mV/fC) the noise level increases to typically about 1 ADC count, which corresponds to the equivalent noise of 231 electrons at this gain.

7 Measurement principle

The first purpose of the test beam was to assess the performance of the LCTPC setup described above. In addition, this setup gave the opportunity to follow up on a study performed on the ALICE TPC using a detailed low level simulation of the detector [14].

The input to these simulations is the energy loss of the charged particle in the chamber gas, obtained from photo absorption ionization (PAI) models [15, 16, 17]. However, an accurate simulation also needs a very good description of the detector effects, such as diffusion, gain amplification variations, and pad response function coupling to different pads/rows. When energy loss calculations are combined with detector effects a good quantitative agreement can be obtained with data, see Fig. 8

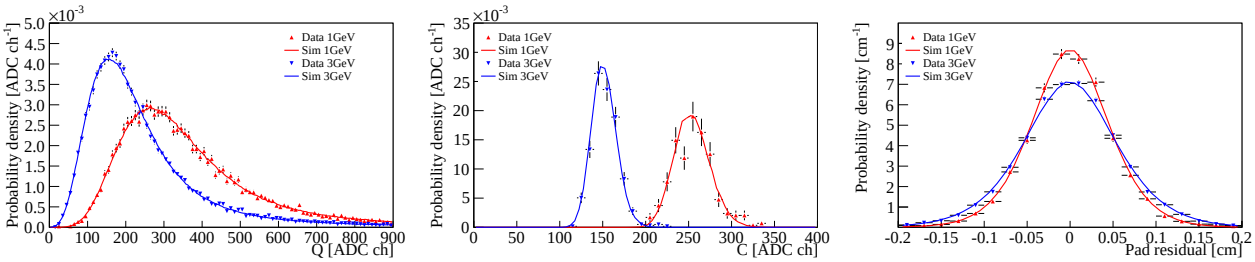

Figure 8: Comparison of simulated data to ALICE TPC test beam data (1 and 3 GeV/c protons) for the straggling function (left), truncated mean (dE/dx) (middle) and position resolution (right). Figures are from [14].

For these studies test beam data is of great importance because there the beam geometry is fixed so that one gather data/statistics under essentially the same conditions (diffusion, track angles etc.) and the identity of the beam particles is well known.

The PAI model calculations include atomic shell effects, but these are hard to observe in the data, because typically the pad length is much larger than the mean free path so that one collects the ionization electrons from several collisions smearing out the discrete energies. For this reason a measurement was performed with the LCTPC rotated by 90 degrees with respect to the test beam so that the short side of the pad (1.2 mm) was parallel to the beam direction whereas the long side (5.2 mm) was transverse to the beam direction. These runs take advantage of the fact that the GEM readout, unlike wire readouts, have no preference for track angles (this is of course not true for the pads but as we want to focus on the energy loss in these runs the worsened space point resolution is not a problem).

Using this configuration, we try to get insight on the energy loss process, in particular on the shell effects present in the PAI model.

This approach using low level simulation presents other advantages:

- It provides the basis for simulation that anyway has to be developed for a detector.
- It enables a cross check whether the measured performance is optimal or could be improved?
- It allows for calibration of the energy loss. The gain can be obtained from the matching of simulation and data.
- It fixes parameters for particle identification using the specific energy loss: mean, resolution, and shape of curve.

8 Simulation

For this study an independent TPC simulation program developed in Lund for a study of the ALICE TPC [14] has been used. The simulation has proven to give a good description of test beam data with the ALICE TPC. For the LCTPC, only the readout part was modified to describe GEMs instead of wire chambers. The processes describing the ionization of the primary particle and the diffusion in the drift volume are the same. The gas processes are:

1. The mean free path is used to randomly determine the distance to the next primary interaction.
2. The particle is propagated to the point of the interaction and an energy loss, E, is randomly determined from the model distribution.
3. The energy loss is converted into a total number of ionization electrons, N_{e}, using the expression:

$$N_{\mathrm{e}} = \frac{E - I}{W} + 1, \tag{1}$$

   where $I = 15$ eV is the first ionization potential, and $W = 25$ eV is the effective energy required to create an electron-ion pair. These values were evaluated from the data in [18][1].
4. Each electron is individually propagated to the pad plane of the readout chamber taking into account only the diffusion. The diffusion constants used were the ones measured with the prototype during the run corresponding to this study.

The simulation of the GEM readout for each drifting electron includes the following processes:

5. At the Gem plane, the electron is assigned a random gain, following an approximate Polya function with factor 1.5.
6. The charge is transfered to the pad plane according to a two dimensional pad response function (PRF). A simple gaussian model is used. Alternative models were tested, but did not seem to induce any change in the results. The width of the PRF was determined from the data. The pad geometry used is exactly the same as used for the data reconstruction.
7. Steps 1-6 are repeated until the particle leaves the active volume.
8. Background noise is added. On top of a random gaussian noise, we add cross-talk in cables. A signal is induced in neighbouring wires in the cables from the pads to the front end card. This effect has been studied from the test beam data itself, as shown is section 10, and the amount of cross-talk was tuned to these results.
9. The data is reconstructed using the same program as for the real data.

The parameters for the energy loss in the gas are directly taken from the models, without any tuning. The parameters specific to the chamber such as the drift velocity, diffusion constant, PRF width and crosstalk were all obtained from different measurements on the test beam data. The only free parameter used to tune the simulation is the absolute value of the gain. It is hard to disentangle the amplification gain from the mean number of primary electrons, and therefore the constraints on the energy loss model are difficult to quantify.

[1] This means that $N_{\mathrm{e}} = 1$ for $E \leq I + W$, $N_{\mathrm{e}} = 2$ for $I + W < E \leq I + 2W$, and so on. In the case of PAI models one can have energy losses, $E < I$. This always results in 1 electron in our simulation.

9 Track reconstruction and track selection

9.1 Geometry

In the parallel configuration (standard running configuration), the pad plane is oriented with the long side of the pads parallel to the beam direction. The coordinate system used in the reconstruction defines the z-direction parallell to the drift direction with the origin at the pad plane, pointing towards the inner of the TPC. The x-direction is oriented perpendicular to the pad rows (along the long side of the pads) and the y-direction is accordingly parallel to the pad rows (along the short side of the pads). A sketch of the pad layout with a track signal, and the coordinate system can be found in Fig. 9.

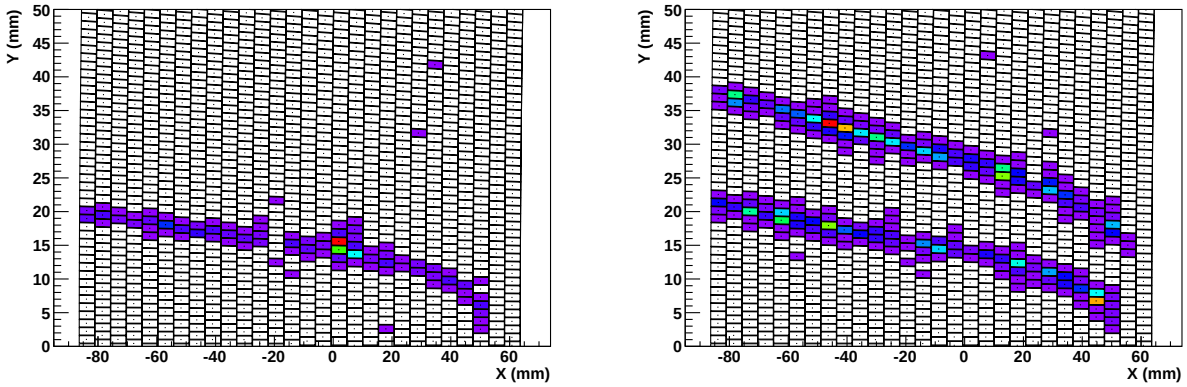

Figure 9: Display of events with one and two tracks, respectively, with the TPC in the parallel configuration. The coordinates of our reference system are also given.

9.2 Clustering

The first step of the *clustering* procedure is to reconstruct the pulses collected on individual pads. The charge collected on the pads is sampled at a frequency of 20 MHz and converted to digital information. Thus, the raw data contains the sampled ADC values, channel number and time information of such pulses (fig. 10). A pulse is defined by the hardware as two or more consecutive nonzero samples, where the threshold is set to 3 ADC counts. The largest ADC-value Q_{max} represents the pulse height and is chosen as a measure of the charge. Time information is retrieved by a charge weighted mean of the five samples around the peak of the pulse. The coordinates of the pulse is taken as the coordinates of the pad center on which the charge was deposited.

Two charge clouds close in time and space might accidentally be included in the same pulse, for example when two tracks pass close to each other. To split them, the algorithm compares the heights of all samples included in a pulse. Starting from one end, a peak is found when the value of a sample is lower than the preceding one. A difference of a two ADC values is required to avoid false peaks resulting from noise fluctuations. All samples up to the point where the values start rising again are included in the first pulse. For the values after that, the procedure is repeated should there be more than two pulses.

The reconstructed pulses are used in an algorithm that combines the pulses in a single pad row into clusters. A search is conducted outwards from the pad having the highest charge. If a pulse is found on a neighbouring pad, within a time window around the peak value, it is added to the cluster. The

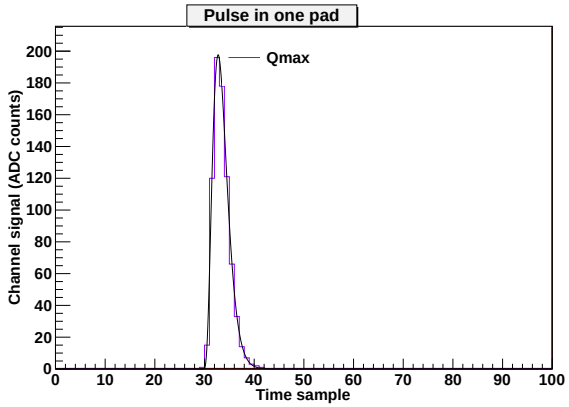

Figure 10: Typical pulse from sampling on an individual pad.

search continues until an empty pad or the end of the pad row is reached. At this point, the search algorithm stops and the pulses are flagged as used to allow the algorithm to find the remaining clusters in the row.

The x and y coordinates of a cluster are calculated from the coordinates of the center of the individual pads. Using a center of gravity method, the cluster coordinate y for example, is calculated according to

$$y = \frac{\sum y_i Q_i}{\sum Q_i} \tag{2}$$

where y_i denotes the y-coordinate of the pad i and Q_i is the charge deposited in this pad. The same method is also applied to the x and z coordinates, where in the case of z the coordinate can be obtained from the time information of the pulse and the drift velocity of the electrons in the chamber gas. The total charge of the cluster is calculated as the sum over the individual charges of the included pulses.

Thanks to the low amount of noise present, it is not necessary to perform any cuts on the clusters. After tracking has been performed, cuts on e.g. cluster size has a very small effect.

9.3 Tracking

For track finding, a simple algorithm is used that performs well in the low track density and low noise environment. A cluster at the module edge is chosen as a starting point. Since the pad plane, in the parallel configuration, is oriented with the beam along the long side (x-direction) of the pads, the next cluster in the track should be found in the neighbouring pad row. A search window is therefore defined around the start cluster in the drift direction (z-direction) as well as in the y-direction. If a cluster is found within the $y - z$-window in the next pad row, it is added to the track. If no cluster is found, the search continues in the next row. Here, a cluster must be found or the track candidate is rejected so that a track is not allowed to contain holes larger than one row. If more than one cluster is found, the one lying closest to the previous cluster in y is chosen.

The procedure is repeated with a new search window around the previous cluster until the other module edge is reached. In order to be accepted, a track needs to include at least 10 clusters and no more than two empty pad rows. The algorithm has been tested extensively and visual cross checks have confirmed that it works well.

When a track has been found, the clusters in it are flagged so that the algorithm can be run again over the remaining clusters. This allows for multiple tracks to be found. Due to conversion, multiple

track events do occur and it is important to find them since they will have an effect on the energy loss distribution.

In the end of the tracking procedure, a fit is made to the coordinates of the clusters. The straigth tracks in the runs without magnetic field are fitted with a first order polynomial and the helical tracks with magnetic field are fitted with a second order polynomial.

9.4 Track Selection

In order to have good quality tracks, two conditons had to be fulfilled for inclusion of a track in the analysis. As mentioned, a maximum number of two missing pad rows were allowed so that the track must have clusters in all but at most two rows. In addition, the track is required to go through the middle of the module to avoid edge effects such as poorly reconstructed clusters where some of the charge ends up outside the instrumented region.

9.5 Perpendicular configuration

As explained in section 7, the LCTPC was also operated in a 90^o rotated configuration. In this configuration the beam was perpendicular to the long edge of the pads and, thus, the width of the charge distribution collected on the pads should be compared to the length (5.2 mm) of the pads. Due to the fact that the width of the charge distribution is smaller than the length of the pads the space resolution is very poor and does not allow to perform a conventional tracking. The track selection is done with the following method:

First a "clean" area area is selected, far from the edges and dead regions of the module. Two "trigger" regions were defined (see fig. 11), which should contain hits to indicate the occurance of a possible track. From the signal in these two regions, a virtual track was formed. The pulses within two pads on each side of this line (in the x-direction) will contribute to the reconstruction of the real track.

On the signal in the corresponding region in $x - y$, we apply the same kind of clustering as in the parallel configuration. Instead of a pad row, we cluster along a "pad line" which connects each pad to one of its two neighbours in the next row.

The tracks defined have at most 52 clusters (see fig. 11).

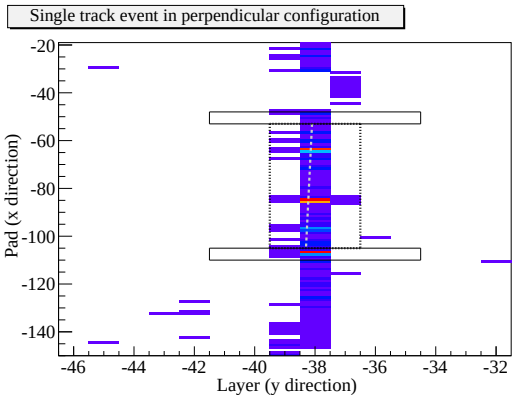

Figure 11: Display of an event with one track in the perpendicular configuration. The black rectangle represent the trigger regions. The gray dashed line is the virtual track. The fine dashed box shows the pads included in the track.

9.6 Event selection

For the following analysis, pure samples of 5 GeV/c electron tracks with the most stable conditions possible were selected, rejecting events with the following two problems:

Gain drops It was observed that a few times per run, the overall gain dropped. From a fit to the average charge of consecutive events in the low gain regions, the gain drops could be identified. Using this, we clean up the data by cutting out the low gain events as shown on Fig. 12.

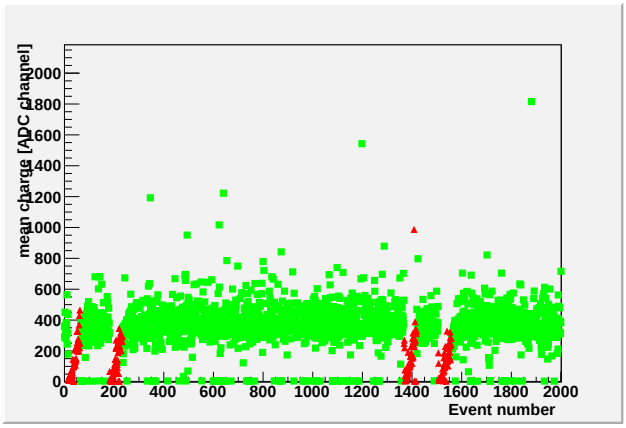

Figure 12: Average pad charge in each event for one run. Periods with gain drop (red triangles) are rejected. The events with zero charge are empty (fake trigger).

Multiple tracks To avoid events with multiple tracks in the perpendicular configuration, events where the ratio between the signal inside and outside a track is too high are rejected (the threshold is tuned for each run).

In both configurations, a cut on the dE/dx of the track is also done to remove double tracks which are too close to be separated in space and time. These look like single track, but has a dE/dx twice as large.

10 Cross talk

In the perpendicular run configuration, the width of the charge distribution from the track is smaller than the width of a pad row (5.2 mm), so that most of the time, we only get signal in one or two pad rows. This fact will be used to measure the signal induced in neighbouring channels through crosstalk in the kapton cables between the pads and the FEC.

10.1 Track selection

First, tracks are defined and selected as explained in section 9.5. From this track sample a refined selection is done to have only tracks that approximately follows the border between two pad rows (in the y-direction). Since the pad geometry is somewhat curved, and the tracks are bent in the magnetic field, a track can in practice never fulfill this requirement exactly and the poor space resolution in the perpendicular configuration does not allow a very precise reconstruction and selection of the proper tracks. However, different approximate methods of selection were tried and they all gave the same final results.

The tracks obtained are separated into two categories (see Fig. 13):

A tracks going between pad rows connected to different connectors

B tracks going between pad rows connected to the same connector

In Fig. 13, the definition of the "close" and "away" rows are given, corresponding to the two rows closest to the track, and their neighbours, respectively. Since the track is going along the border of two pad rows the charge should give signals in the pads of both "close" rows, whereas it is not expected to see any signal in the "away" rows due to the electron cloud being much smaller than the pad size tranverse to the track in this configuration. This can be verified by events from the case B where no signal should be observed on the "away" rows since these are read out by different connectors compared to the "close" rows and therefore could also not have any contribution from possible cross talk in the cables. For events fulfilling the requirements of case A the "close" rows are read out by different cables and the only explanation for an observed signal in the "away" rows must be cross talk in the kapton cable.

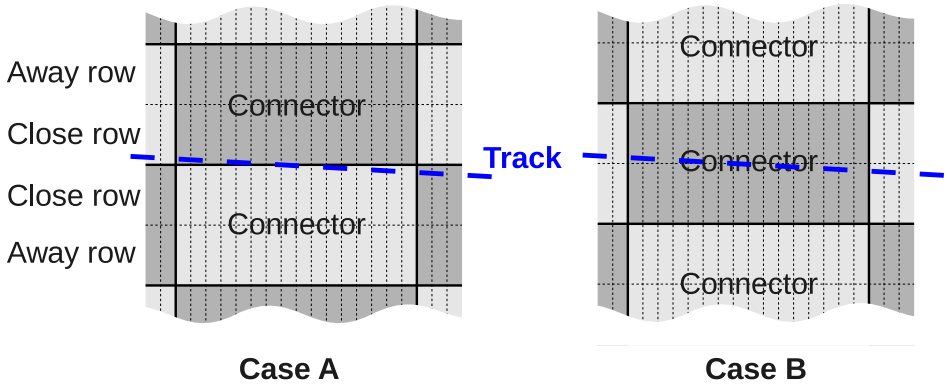

Figure 13: Schematic picture giving the definition of the "close" and "away" rows, respectively, for the two situations A and B described in the text.

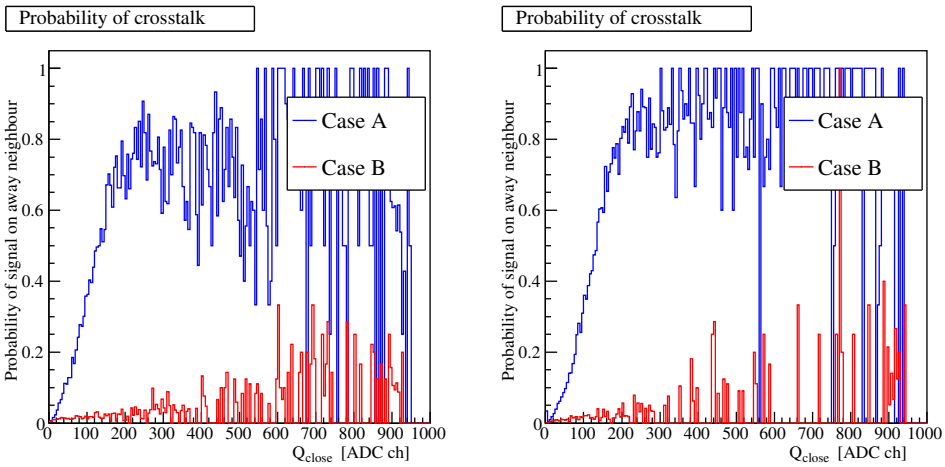

Figure 14: Probability to observe a signal in the "away" row, when a signal on the "close" row is measured. The left and right plots correspond to the pad rows on each side of the track.

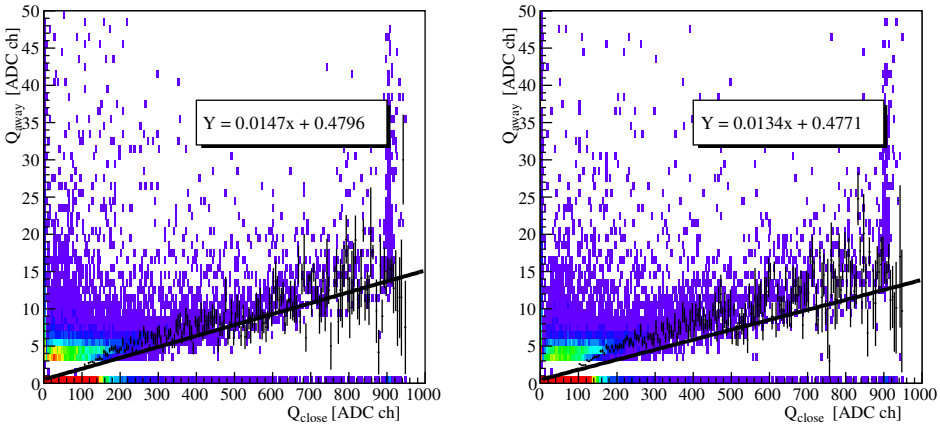

Figure 15: The charge deposited on pads in the "away" row versus that deposited in the "close" row for case A. The left and right plots show the distribution for the two neighbouring channels in the cable.

10.2 Results

The first goal was to see whether the results gave any indication of cross-talk. Fig. 14 shows the probability to get a signal in the "away" row, when there is one in the "close" row. It is clearly seen that in case A, if the "close" signal is large enough, there is almost always an "away" signal, while in case B, a signal almost never appears in the "away" row (as expected since these are read out by different cables). Exactly the same effect is observed for the pad rows on each side of the track, which excludes the possibility of a geometric effect from the track angle or the curved pad geometry.

The cross-talk results shown in Fig. 14 suggest a threshold effect around Q=200 ADC counts. In Fig. 15, the charge collected on a pad in the "close" row is plotted versus the charge collected on its neighbouring pad in the "away" row for the case A. Here the neighbour pad is chosen specifically to be one of the two closest cable lines in the readout cable. From this figure we see clearly the effect of zero-suppression for the low charges, for which the cross-talk is mostly below threshold. From the fit on the average correlation in Fig. 15, it can clearly be seen that the effect of the cross-talk is below 2% of the main signal. The results were confirmed by doing a test with a pulse generator.

11 Performance study

The data taken with the LCTPC in the two different configurations described above were analysed and compared to the results from simulations. The simulated data was created with the same format as real data. The analysis of real and simulated data were performed in exactly the same way, using the clustering and track finding as described in section 9.

11.1 Charge deposition

The main focus was on the charge deposition and the purpose was to confront the energy loss models with data. Since the absolute signal gain was the only free parameter of the simulation, it was important to match it to the data.

11.1.1 dE/dx resolution

In order to determine the gain in the simulation, the dE/dx of the tracks was measured. Since we use ultra-relativistic electrons, on the plateau region of the Bethe-Bloch curve, a very clean sample for the dE/dx is expected. The value of dE/dx is calculated as the 60% truncated mean of the signal in the track, taking the mean of the 60% lowest signals in the track.

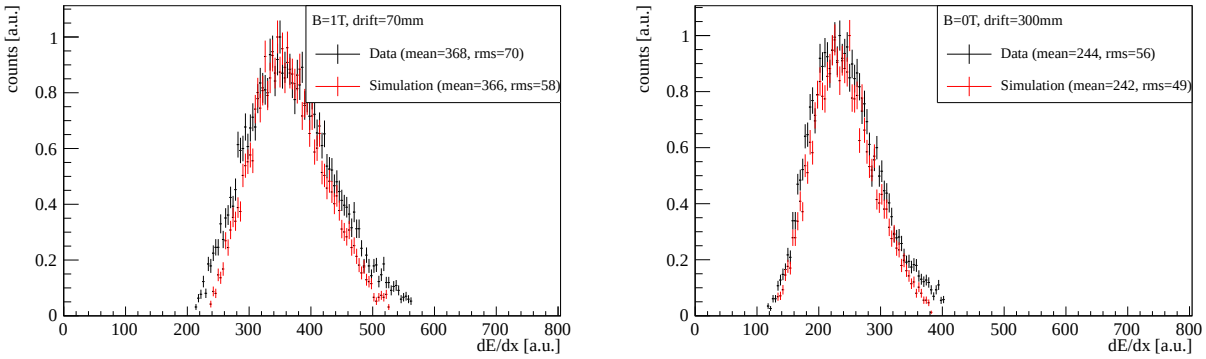

Figure 16: The dE/dx spectrum, calculated from the 60% truncated mean. A comparison between simulation (in red), using Geant4's PAI model, and data (in black) is given in the case of a 1 T magnetic field (left) and no magnetic field (right).

The results are shown for the parallel configuration in Figs. 16 and 17. The gain parameter in the simulation is adjusted so that the mean value of the dE/dx distribution agrees with the experimental data. It can be observed that the dE/dx distribution in the simulation is somewhat narrower than that of the real data.

In Fig. 17, we see that the diffusion gets more prominent as the drift distances increase, an effect that is especially significant with no magnetic field and less significant with a 1 T magnetic field on. The correlations that the diffusion induces between pad rows (i.e. between clusters in the track) alters the charge distribution and worsens the dE/dx resolution.

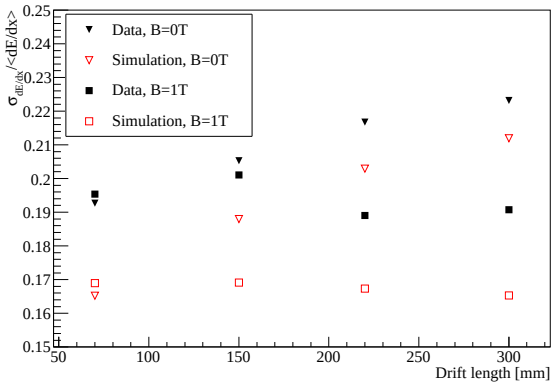

Figure 17: dE/dx resolution as a function of drift distance.

11.1.2 Charge distribution

To get a better understanding of the dE/dx results, the full charge distribution of the clusters in the tracks can be studied. The results are shown in Fig. 18. It can be observed that the simulation does not describe the data taken in the parallel configuration very well. The energy loss model is not precise enough to reproduce the details of the data. However, when the diffusion increases as is the case with no magnetic field and longer drift lengths, the correlations between clusters smear out the details of the model, and simulation and data start to agree.

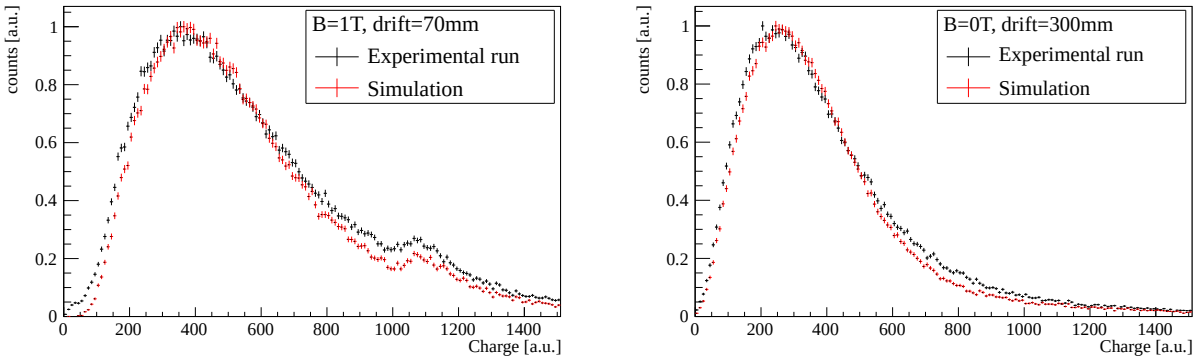

Figure 18: Charge distribution in different diffusion cases (left: minimum diffusion (short drift, B=1T), right: maximum diffusion (long drift, B=0T). With increasing diffusion, the details of the energy loss model are smeared out and the simulation gives a better description of the data. The bumps in the low diffusion case is caused by the saturation in ADC channel 1024 of the digital signal in each pad (see section 6).

11.1.3 Comparison of the charge distributions for the two configuration

With the two configurations (parallel and perpendicular), we have the opportunity to test the consistency of the energy deposition comparing sampling over short track segments (1.2 mm) and longer ones (5.2 mm). Due to different levels of correlations, the charge distribution does not scale in a simple way as the sampling length is increased [16]. However, since the size of a pad is approximately 1.2 mm by 5.2 mm, the width of four pads is 4.8 mm which is approximately the same as the length of a pad. Thus, by combining signals from 4 neighbouring pads in the perpendicular configuration, the charge distribution should be comparable to that of the parallel configuration.

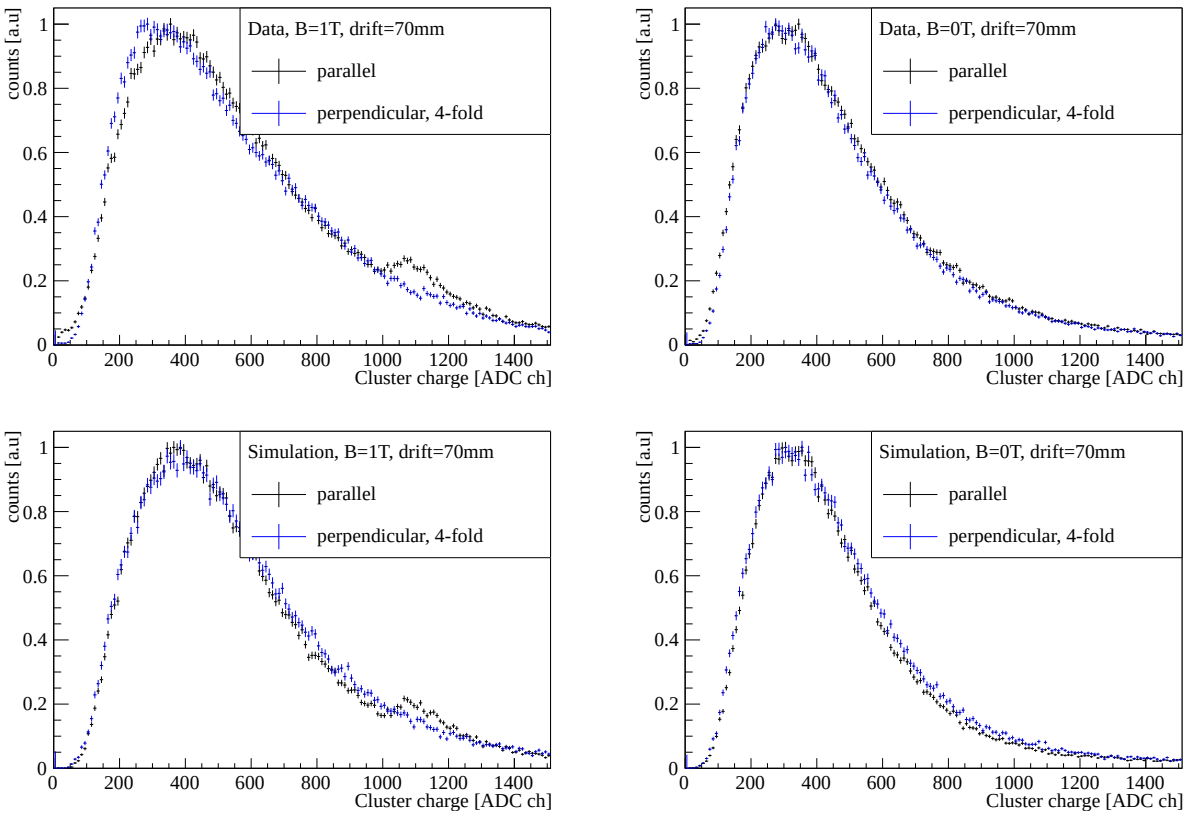

Figure 19: Comparison between the charge distribution for the parallel configuration (5.2 *mm* long pads) and the charge collected on four consecutive pads (4x1.2 *mm*) in the perpendicular configuration. A correction factor is introduced to compensate for gain difference and possible efficiency difference. The upper plots are data and the lower are simulation with the same run characteristics.

In Fig. 19, the charge distribution from track clusters in the parallel configuration, is compared to the charge distribution of clusters grouped over four consecutive pads in a track in the perpendicular configuration. The conditions for the runs which are compared are the same i.e. the drifts length, magnetic field, electronics settings are identical. An additional scaling of the charge is done for one of the configurations to account for gain variations and possible different charge collection efficiencies.

Fig. 19 gives comparisons of charge distributions for the two different configurations with (left hand plots) and without (right hand plots) the magnetic field on, for real data (upper plots) and for simulation data (lower plots). The agreement is perfect. In spite of the differences in the charge distribution (fig. 18), it is clear that the simulation reproduces the consistency between the two configurations. This indicates that besides the energy loss process, the detector is well described by the simulation. It also means that effects observed on the charge in the perpendicular configuration should be consistent with what is observed in the parallel configuration.

11.1.4 Perpendicular configuration

The final step of the energy loss study was to investigate if it was possible to observe the details of the energy loss process from measurements in the perpendicular configuration with a 1 *mm* sampling length. In Fig. 18 it was noticed that there are discrepancies between the real and the simulated data for the parallel configuration. However, in section 11.1.3, it was shown that measurements in the two configurations are consistent. Thus, the discrepancies observed in the measurements with the

parallel configuration could be further investigated in the perpendicular configuration and possibly be associated with some details of the energy loss model.

In Fig. 20 the charge distribution for different steps in the simulation are shown for the lower part of the pulse height spectrum. A description of the various distributions is given below:

Number of ionisation electrons , represented with triangle (▼), is the number of electrons produced after ionisation, at the track level, over the longitudinal size of the pad (1.2 mm). For comparison, it is multiplied by the average gain.

Number of electrons reaching the GEMs , represented with blue squares, is the number of electrons reaching the GEM plane. The only added effect from the previous number is diffusion. For comparison, it is multiplied by the average gain.

Reconstructed charge , in red open circles, is the charge read out on the pads, after all effects (gain variation, noise, digitisation). It is the value to be compared directly to the data (represented with the black circles).

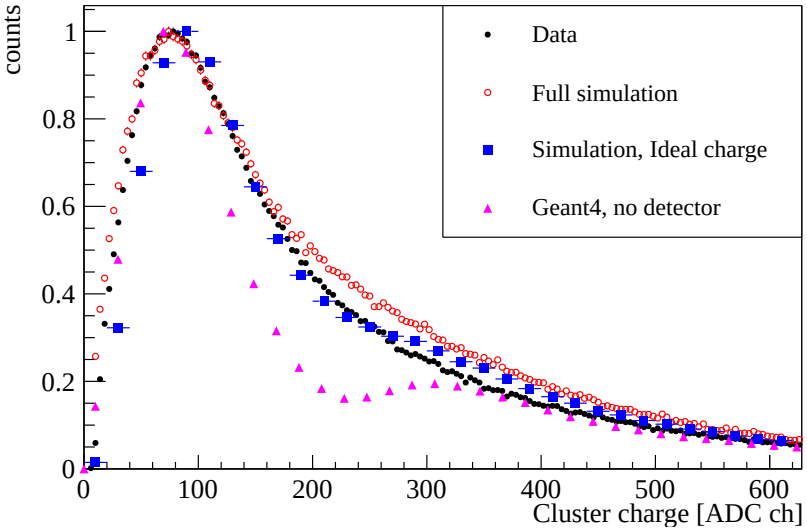

Figure 20: Charge distribution for minimum diffusion, with 1.2 mm wide pads for the lower part of the pulse height spectrum. The triangles (▼) show the number of ionisation electrons produced. The blue squares shows the number of electrons reaching the GEM plane (after diffusion). The red open circles is the full simulation. The real data is represented by black full circles. We can see the bump from the second shell of Argon can be associated with the excess the simulation shows compared to data around 300 ADC.

In Fig. 20, a bump in the number of ionisation electrons (around 300 equivalent ADC channels) is observed, which is related to the L shell in Argon. Following the steps in the simulation shown in the figure, we can associate this bump to an excess in the reconstructed charge compared to data around 300 ADC channels. This suggests that the ionization from inner shells is inadequately modeled.

11.2 Space Resolution

Since no external reference is available, the resolution is calculated with respect to the reconstructed track. The track is obtained from a fit to the cluster coordinates and the residuals (in y) of the individual points are calculated using this fit. The resolution is then obtained as the width σ_y of the residual distribution, obtained from a gaussian fit. Since the investigated point is included in the fit,

this is expected to give an estimation that is better than the actual resolution. A common approach to this is to use the Geometric Mean method. According to this method, another fit is made, this time excluding the investigated point. The geometric mean of the resolutions obtained with the two methods is then calculated $\sigma = \sqrt{\sigma_{in} \cdot \sigma_{ex}}$, where σ_{in} and σ_{ex} is the resolution calculated with the point included and excluded, respectively, in the fitting procedure. This is considered to be a more reliable estimation of the "true" resolution.

Without magnetic field (Fig. 21), the simulation gives a perfect description of the space resolution in the data.

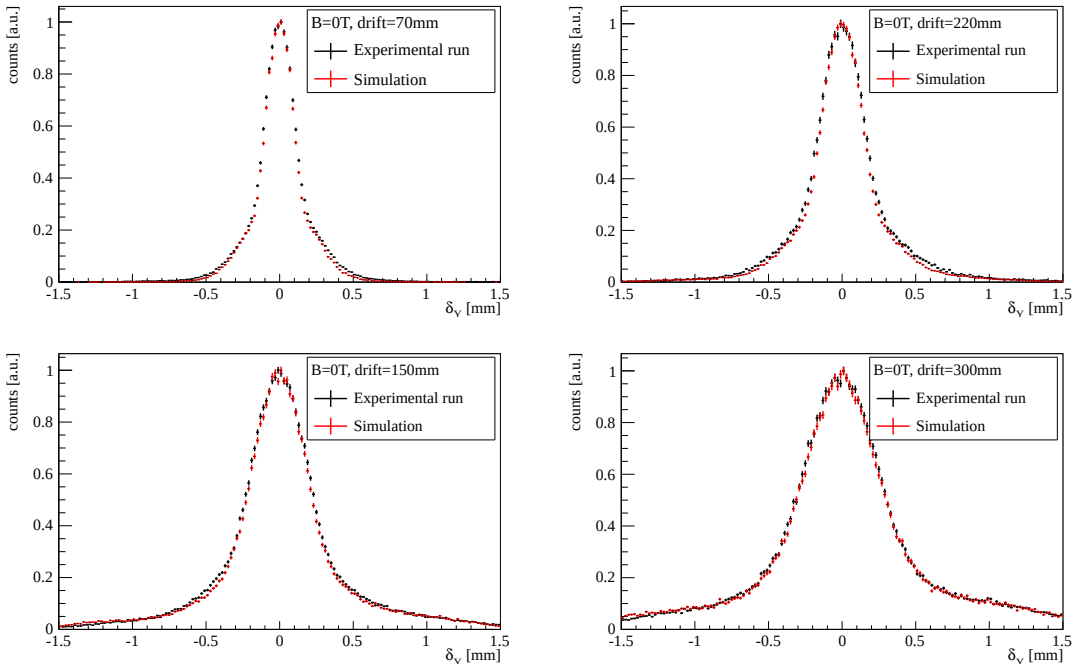

Figure 21: Space residuals for different drift distances, without magnetic field. The simulation (in red) gives a perfect description of the data.

As mentioned in section 4, there was an inhomogeneity of the electric field around the edges of the GEM plane. In the presence of magnetic field, this caused distortions of the tracks, due to the $E \times B$ effect. The tracks appeared as a consequence of this slightly deformed compared to the expected arc. This worsened considerably the resolution measurement relying on a polynomial fit to the track.

An attempt to correct for the distortion was made, using the residual distributions of the individual pad rows. The residuals are calculated assuming a helical track described by a second order polynomial in the transverse projection. Due to the know problem with the distorted electric field at the edges of the GEM the information from outermost 5 pad rows were excluded and a fit was only performed for the middle part of the track, which should be less influence by the field inhomogeneities. Fig. 22 shows the calculated residuals versus the pad rows for many events in a run. A clear S-shape can be observed. Taking the residuals averaged for each row (x-value) a distortion (y-value) can be calculated. This averaged value is used to correct the y-coordinates on a row-by-row basis.

To account for the distortion in the simulation, a fit with a fifth order polynomial to the distortion shape in the data was made as shown on Fig. 22. The fitted distortion was included in the simulation as follows. Since the position of the clusters in the x-direction cannot be measured to a better precision than the length of the pads (5.2 mm), the displacement (in the y direction) applied to each cluster was chosen from the fit at a *random* point (in the x direction) in the corresponding pad row. When the simulated data are corrected in the same way as the real data by the distortion (now *average* over

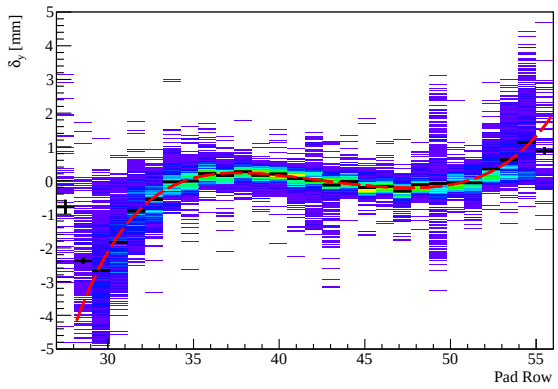

Figure 22: Space residuals δ_y versus pad row. The S-like shape is a consequence of the $E \times B$ effects associated with electric field distortions caused by the support pillars of the GEMs. This profile (black lines) is used to correct the data. The profile is fitted (dashed line) to provide a model of the distortion for the simulation.

the pad length), a spread of the residuals in each row remains due to the unknown cluster position along the pad length. Fig. 23 shows that the simulation gives a good description of the data after inclusion of the track distortion. Ideally the distortions should be done at the electron level in the simulation, but these results anyway suggest that the origin is our lack of knowledge of where along the pad the electrons dominates. Therefore this distortion cannot easily be corrected for, and, to achieve the resolution of 70 μm predicted by the simulation, the electric field close to the GEMs has to be improved.

The space resolution (σ_y) for different drift distances are shown in Fig. 24 from which it is seen that when the drift distance, and therefore the diffusion, is increased, the resolution of the space position of the track becomes worse.

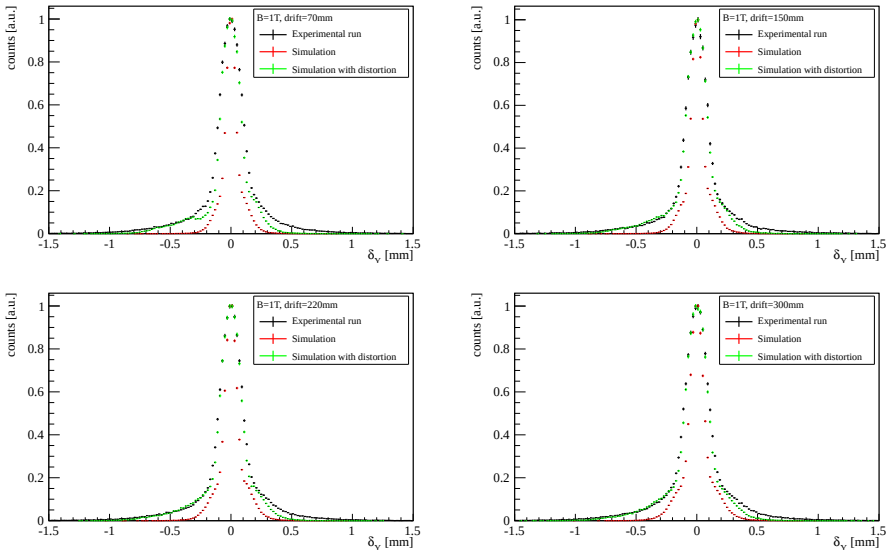

Figure 23: Space residuals (δ_y) for different drift distances, with magnetic field. The $E \times B$ effects, associated to the electric field distortions caused by the support pillars of the GEMs, made the resolution worse for the data (black) than for the simulation (red). After introducing corrections to account for the distorions, the simulation (in green) gives a much better description of the data.

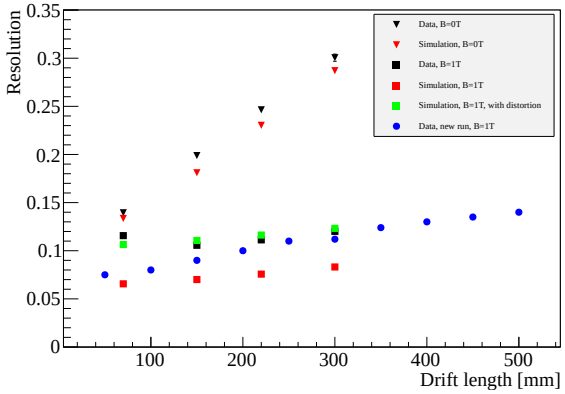

Figure 24: Space resolution for data and simulation. When the drift distance, and therefore the diffusion, is increased, the resolution of the space position of the track becomes worse. With magnetic field, $E \times B$ effects associated with electric field distortions made the resolution worse for the data (black squares) than for the simulation (red squares). After including the distortion, the simulation (green squares) matches the data.
The blue dots show for comparison the resolution measured by the Japanese group on more recent data using the same setup. The method of calculation was different, which explains the slightly different values.

11.3 Influence of ADC resolution

In the current version of the electronics, the analogue signal is digitised with a 10-bit precision (1024 ADC channels). This high resolution is likely to be better than needed, given that the pad width is only 1.2 mm. Reducing the ADC resolution to an optimal value will result in a reduction of power and cost for the electronics.

In order to test this, the digital representation of the raw signal was changed by removing the ADC bits one by one to see at which point a decrease in resolution could be observed. The regular reconstruction is then performed. The size of the ADC signal is reduced from 10 bits down to 8, 6 and 4 bits, and the performance of the LCTPC is compared for the various resolutions.

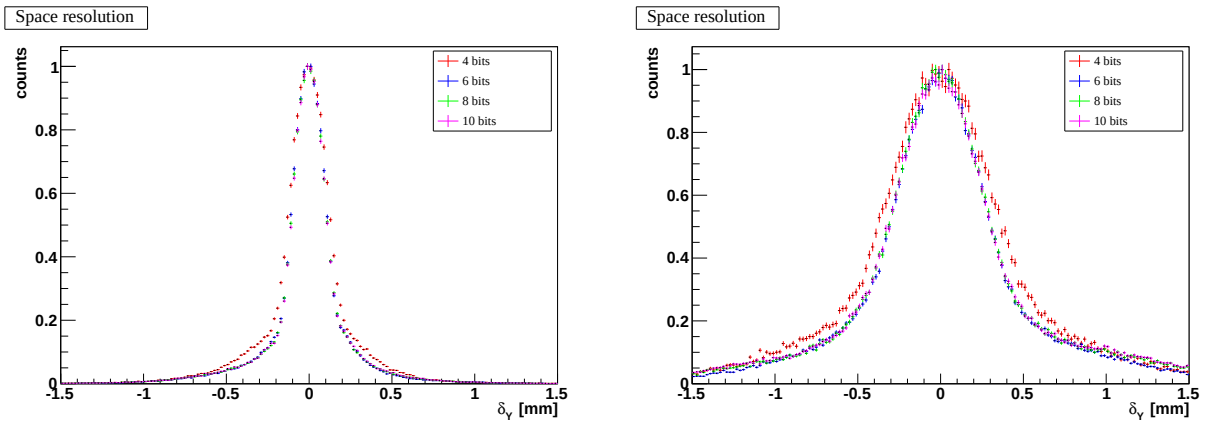

Figure 25: Examples of space residual (δ_y) distributions for different values of the ADC resolution. On the left, with minimum diffusion (70 mm drift and magnetic field on), and on the right with maximum diffusion (300 mm drift and no magnetic field).

From Figs. 25 and 26, it is obvious that no deterioration of the space resolution is observed until

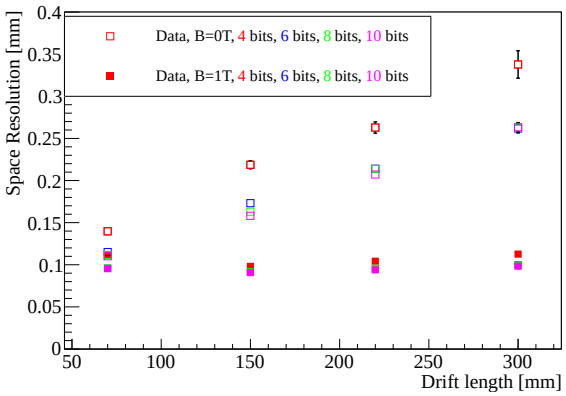

Figure 26: Space resolution as a function of drift distance for different values of the ADC resolution.

the precision has been lowered to 6 ADC bits. Below that a worse space resolution is observed, mostly because of threshold effects.

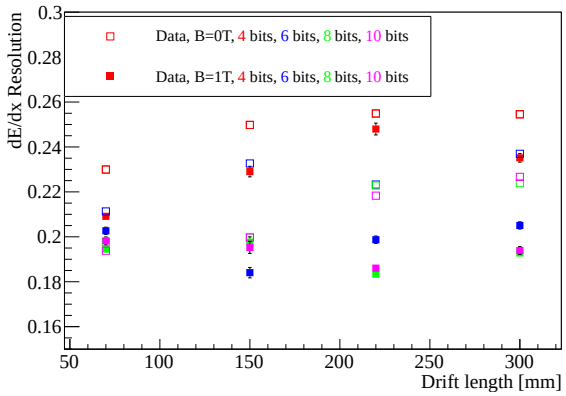

Figure 27: dE/dx resolution as a function of drift distance for different values of the ADC resolution.

In Fig. 27, it is seen that, as expected, the loss in ADC resolution has more influence on the dE/dx resolution. However, down to 6 bits, the loss is not excessive, and begins to be significant at 4 bits.

This shows that the ADC range can be reduced without real damage to the performance. However, this test has been done with electrons on the ultrarelativistic plateau. It should be confirmed for minimum ionising particles, where the effect should be maximal. There is in any case range for adjustment of the digital signal.

12 Conclusion

The large prototype TPC (LCTPC) equipped with Asian GEMs and electronics based on the ALICE ALTRO, has been successfully set up and tested thoroughly in the DESY T24 electron beam with different configurations. The data has been reconstructed, analysed and compared to simulations using software developed in Lund.

Running the LCTPC in a rotated configuration allowed to reach a high level of detail in the study of the charge distribution along tracks. The comparison to simulation allowed to probe the limits of the energy loss models, in particular the PAI model offered by GEANT4.

This unusual orientation also allowed to study cross talk in the readout cables in a real data taking situation.

In spite of imperfection of the energy loss model, the performance of the TPC has been very well described by the simulation. A loss of resolution from distortions from $E \times B$ effect related to inhomogeneities of the electric field close to the GEM was observed. The observed resolution could be described by simulation with a simple correction in reconstructed clusters to include the distortions. While it shows that there is little hope to recover space resolution with the inhomogeneous electric field, it indicates that the resolution of 70 μm shown by the simulation should be achievable if the field is improved.

Acknowledgements

This work is supported by the Commission of the European Communities under the 6th Framework Programme "Structuring the European Research Area", contract number RII3-026126. The project was also supported by the Swedish Natural Science Research Council. We would like to thank K. Dehmelt, T. Matsuda and H. Kuroiwah for help in setting up the equipment needed for the measurement, and H. Bichsel and V. Grichine for help with the energy loss models for the simulation.

References

[1] T. Behnke *et al.*, EUDET-Memo-2007-11.

[2] J. Timmermans, private communication.

[3] T. Behnke *et al.*, EUDET-Memo-2006-042

[4] T. Behnke *et al.*, "A Lightweight Field Cage for a Large TPC Prototype for the ILC", JINST **5** (2010) P10011 [arXiv:1006.3220 [physics.ins-det]].

[5] K. Dehmelt on behalf of the LCTPC Collaboration, EUDET-Memo-2008-46

[6] K. Dehmelt on behalf of the LCTPC Collaboration, EUDET-Memo-2009-9

[7] A. Ishikawa *et al.*, "A GEM TPC End-Panel Pre-Prototype" *In the Proceedings of 2007 International Linear Collider Workshop (LCWS07 and ILC07), Hamburg, Germany, 30 May - 3 Jun 2007, pp TRK27* [arXiv:0710.0205 [physics.ins-det]].

[8] T. Matsuda [LC-TPC Collaboration], "Results of the first beam test of a GEM TPC large prototype", JINST **5** (2010) P01010.

[9] A. Yamamoto and Y. Makida, "Superconducting magnet for long duration flights", Proceedings of the 5th Workshop on 'Balloon-borne experiments with a superconducting magnet spectrometer', KEK Japan, November 30 - December 1, 1994.

[10] L. Musa *et al.*, "The ALICE TPC Front End Electronics", Proc. of the IEEE Nuclear Science Symposium, 20 - 25 Oct 2003, Portland

[11] R. Esteve Bosch, A. Jimenez de Parga, B. Mota and L. Musa, IEEE Trans. Nucl. Sci. **50** (2003) 2460.

[12] L. Musa, "Prototype compact readout system", EUDET-Memo-2009-31, 2009.

[13] C. Gonzales Gutrierrez *et al.*, "The Alice TPC Readout Control Unit", *In the Proceeding of the 2005 IEEE Nuclear Science Symposium and Medical Imaging Conference, Puerto Rico, October 23-29, 2005*

[14] P. Christiansen et al., Nucl. Instr. and Meth. A 609 (2009), p. 149

[15] J. Apostolakis *et al.*, Nucl. Instrum. Meth. A 453 (3): 597-605, 2000

[16] H. Bichsel, Nucl. Instrum. Meth. A **562**, 154 (2006).

[17] H. Bichsel, Nucl. Instrum. Meth. A **566**, 1 (2006).

[18] ICRU Report 31: Average energy required to produce an ion pair. Bethesda, MD: ICRU Publications, 1979.